UNIVERSITÄT DUISBURG ESSEN

Offen im Denken

JÜLICH Forschungszentrum | HELMHOLTZ-INSTITUT MÜNSTER

Polymer electrolytes in lithium metal batteries: From interfacial charge transfer to projections of energy density

Zum Erwerb des akademischen Grades

Doktor der Naturwissenschaften

(Dr. rer. nat.)

der Fakultät für Physik der Universität Duisburg-Essen vorgelegte

Dissertation

von

Peter Lennartz

aus Geldern

1. Gutachter: Prof. Dr. Hermann Nienhaus

2. Gutachter: PD Dr. Gunther Brunklaus

Datum der Disputation: 22.11.2024

“When life gives you lemons, make a lemon battery”

Zusammenfassung

Polymerelektrolyte könnten Batterien mit bisher unerreichten Energiedichten ermöglichen, die Lithium (Li) Metall als Anode enthalten. Während des Ladens und Entladens wird Li-Metall oft inhomogen abgelagert bzw. aufgelöst, was Nebenreaktionen und den Verlust des verfügbaren Li-Inventars fördert und schließlich die Lebensdauer der Batterie verringert. Polymerelektrolyte könnten zu sichereren und langlebigeren Li-Metall-Batterien beitragen, da sie im Vergleich zu den in flüssigen Elektrolyten verwendeten Lösemitteln weniger flüchtig sind und zudem die mechanischen Eigenschaften der Elektrolytmembranen einstellbar sind. Der Ionentransport im Volumenelektrolyten und an Elektroden-Elektrolyt-Grenzflächen bestimmt die Lade-/Entladeleistung der Zellen. Trotz langjähriger Forschung sind die Wechselwirkungen zwischen Änderungen an Elektroden-Grenzflächen und den Eigenschaften des Elektrolyten noch nicht vollständig verstanden. Auch die Anwendbarkeit polymerbasierter Li-Metall-Batterien in der modernen Technik (z. B. in Elektrofahrzeugen) wird oft vermutet, aber selten eingehend untersucht. In der vorliegenden Arbeit wurden daher polymerbasierte Li-Metall-Batterien auf verschiedenen Ebenen analysiert, von der mikroskopischen Ladungsübertragung bis hin zum Anwendungspotenzial solcher Batterien in modernen Elektrofahrzeugen. Ausgewählte Polymerelektrolyte wurden mit elektrochemischer Impedanzspektroskopie und Verteilung der Relaxationszeiten (DRT) charakterisiert. Es konnten charakteristische Zeitkonstanten des Ladungstransfers und der Grenzphasenwiderstände ermittelt werden, die von der Temperatur und der Art des Elektrolyten (trocken/gelartig/flüssig) abhängen. Darüber hinaus konnten durch die Kombination von DRT und Röntgenmikrotomographie dynamische Veränderungen der Li-Mikrostrukturen beobachtet und mit experimentell zugänglichen Messgrößen wie den Interphasenwiderständen und den zugehörigen Zeitkonstanten korreliert werden. Stark abnehmende Widerstände wurden dem Wachstum der mikroskopischen Oberfläche zugeordnet, während ein langfristiger Anstieg des Interphasenwiderstands mit dem Wachstum kugelförmiger Li-Metallablagerungen in Verbindung gebracht wurde, die sich häufig an Elektrolytverunreinigungen bilden. Auch wurde *in situ* ^{7}Li-NMR-Spektroskopie eingesetzt, um die sich auf reinen und modifizierten Li-Metallelektroden entwickelnden Li-Mikrostrukturen zu charakterisieren, was die positive Wirkung Si-basierter Elektroden-Beschichtungen bestätigte. Unter Verwendung eigens entwickelter Mikroelektroden wurde die Ladungstransferkinetik zwischen Li-Metall und Polymerelektrolyten evaluiert, speziell um die Austauschstromdichte zu bestimmen, eine grundlegende Gleichgewichtsstromdichte, die die Reaktionsraten begrenzt. Ähnlich wie bei flüssigen Elektrolyten konnte die Kinetik des Ladungstransfers gegen Li-Metall mit der Marcus-Hush-Theorie des Ladungstransfers modelliert werden, wobei sich jedoch im Vergleich zu flüssigen Elektrolyten wesentlich geringere Austauschstromdichten ergaben. Schließlich wurde das Anwendungspotential polymerbasierter Li-Metall-Batterien mit Hilfe einer selbst entwickelten Software bewertet, die eine Projektion der Energiedichten mehrschichtiger Pouch-artiger Zellen auf der Grundlage von Parametern ermöglicht, die auch für kleinere experimentelle Zellen verfügbar bzw. zugänglich sind. Hohe Kathodenmassenbeladungen (> 1 mAh cm^{-2}), dünnes überschüssiges Li-Metall (< 20 µm) und dünne Elektrolytmembranen (< 30 µm) sind dabei Schlüsselstrategien zur Förderung der Anwendbarkeit. Wenn sie in modernen Batteriepacks für Elektrofahrzeuge eingesetzt werden, könnten diese Energiedichten von bis zu 422 Wh L^{-1} erreichen, was das zukünftige Potential polymerbasierter Li-Metall-Batterien unterstreicht.

Summary

Polymer electrolytes may enable next generation batteries that contain lithium (Li) metal as anode, providing higher energy densities than state-of-the-art Li ion batteries. During charging and discharging, Li metal is often inhomogeneously deposited and dissolved, respectively, thereby promoting side reactions and losses of available Li inventory, eventually reducing the cycling life of the battery. Here, polymer electrolytes may contribute to safer and more durable Li metal batteries due to reduced volatility compared to solvents used in liquid electrolytes and tunable mechanical properties of the electrolyte membrane. Ion transport in the bulk electrolyte and at the electrode|electrolyte interfaces governs charging/discharging performances. Despite decades of research, the interdependencies of interfacial variation and key properties of the electrolytes are not yet fully understood. Also, the applicability of polymer-based Li metal batteries in modern technology (e.g., in electric vehicles) is often presumed, but seldomly considered in depth. Hence, polymer-based Li metal batteries were analyzed in this thesis on different levels, ranging from microscopic charge transfer to the evaluation of the application potential of such batteries in state-of-the-art electric vehicles. Various polymer electrolytes were characterized with electrochemical impedance spectroscopy and distribution of relaxation times (DRT) analysis. Characteristic time constants reflecting both charge transfer and interphase resistances could be identified, depending on the operation temperature and type of electrolyte (dry/gel/liquid). Also, combining DRT and X-ray microtomography, dynamic changes of occurring Li microstructures could be monitored and correlated with experimentally accessible observables, such as the interphase resistances and the associated time constants. Strongly decreasing resistances were assigned to a growth of microscopical surface area, while a long-term increase of interphase resistances was associated with the growth of globular Li metal deposits, that often nucleate at electrolyte impurities. In addition, *in situ* ^{7}Li NMR spectroscopy was employed to resolve Li microstructures evolving on pristine and modified Li metal electrodes, corroborating the beneficial impact of Si-based coatings on cell cycle life and Li reversibility by promoting the formation of inorganic-rich solid electrolyte interphases. Invoking custom-made micro electrodes, the charge transfer kinetics between Li metal anodes and polymer electrolytes was characterized based on cyclovoltammetry, explicitly determining the exchange current densities, a fundamental equilibrium current density that limits reaction rates. Similar to liquid electrolytes, the charge transfer kinetics against Li metal could be modeled based on a Marcus-Hush type theory of charge transfer, though yielding substantially lower exchange current densities compared to liquid electrolytes. Lastly, the corresponding application potential of polymer-based Li metal batteries was evaluated, using a custom-made software, that enables projection of energy densities of multi-layered pouch cells based on parameters available and accessible from common experimental cell setups. Here, high cathode mass loadings (> 1 mAh cm^{-2}), thin excess Li metal anodes (< 20 µm) and thin electrolyte membranes (< 30 µm) constitute key strategies to further promote applicability. When implemented in state-of-the-art battery packs for electric vehicles, energy densities of up to 422 Wh L^{-1} could be projected, clearly highlighting the future potential of polymer-based Li metal batteries.

Preface

The research activities conducted for this doctoral thesis were carried out and funded within the framework of the *U.S.-German Collaboration on Energy Storage*, in particular the project "LISI – Lithium Solid Electrolyte Interphases", sponsored by the German Ministry of Education and Research ("BMBF") and the United States Department of Energy (U.S. DOE). The Helmholtz-Institute Münster coordinated the activities on the German side and collaborated with renowned U.S. institutes such as the Lawrence Berkeley National Laboratory (LBNL), Pennsylvania State University (PSU), Stanford University (SU), Massachusetts Institute of Technology (MIT), Argonne National Laboratory (ANL), and the Oak Ridge National Laboratory (ORNL). The strong focus on joint collaboration is mirrored by the results presented and discussed in this doctoral thesis, including exchange of materials and exploitation of advanced analytical methods made available by the partners. All the contributions originating from collaborative efforts are explicitly stated throughout this thesis, wherever applicable.

Table of Contents

1. Motivation

Electrochemical energy storage today is among the most relevant research topics, not least due to increasing demands of versatile and efficient energy storage solutions for the mobility sector and the overall transition towards renewable energy sources. Here, batteries present a prominent example, owing to their high efficiency and flexible design opportunities. In view of electromobility, key characteristics of batteries, such as energy density, specific energy and rate capability manifest themselves in pronounced driving ranges and fast-charge capabilities of battery electric vehicles. Note that specific energies of 350 to 500 Wh kg^{-1} and driving ranges of >500 km per charge are reasonable goals defined by the United States Advanced Battery Consortium (USABC).[1,2] Meeting these challenging demands requires further advances in materials and cell development, especially comprising major components of current batteries: electrodes and electrolytes. While both the anode and cathode should store as much charge as possible per unit volume and mass, the electrolyte should provide sufficient ionic transport while maintaining a robust and electronically insulating barrier between anode and cathode. Today, state-of-the-art rechargeable batteries often contain graphitic anodes that more or less reversibly absorb (intercalate) and release (de-intercalate) charge carriers such as lithium (Li) ions. Alternative anode materials could potentially increase the available energy densities of the cells, thereby enhancing driving ranges of electric vehicles.[3] For example, the specific capacity (amount of electric charge per unit mass) of Li metal (3860 mAh g^{-1}) is 10-fold larger than that of graphitic anodes (372 mAh g^{-1}), rendering it an attractive anode material for next-generation batteries.[4] In view of electrolytes, polymer-based electrolytes are a promising class of materials compared to liquid electrolytes that often contain highly flammable solvents and thus pose the safety risk of leakage or fire. However, despite the intrinsic advantages of Li metal anodes compared to conventionally used graphitic anodes, and irrespective of the kind of electrolyte, substantial operational challenges remain that prevent cell longevity and faster charge capabilities, including limited reversibility of the Li inventory during charging and discharging. In contrast to intercalation of Li ions into graphite, Li metal is dissolved when the battery is discharged and (re-)deposited on anodes during charging. The deposited Li metal species often have a significantly higher surface area compared to pristine bulk Li metal, fostering continued side-reactions of Li metal with electrolyte constituents that eventually compromise the available amounts of reversible Li inventory of the cells. Ideally, the decomposition layer acts as a solid electrolyte interphase (SEI) and prevents further electrolyte decomposition, while enabling suitable charge transfer from Li metal electrodes to the electrolyte and vice versa.

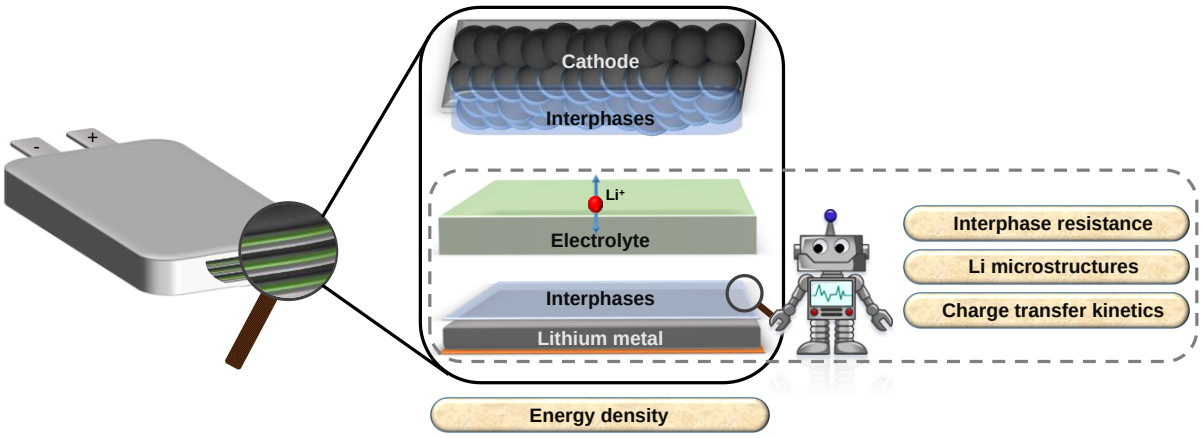

***Figure 1**: Scheme of a pouch cell and its individual layers, comprising electrodes, electrolyte and interphases, as well as key observables to be analyzed at Li|electrolyte interfaces.*

The actual impact of polymer-based solid electrolytes and artificial interphases on the reversibility of Li metal deposition and associated charge transfer reactions is far from being understood to a degree such that one could speak of *optimized* cell chemistry or exerting *control* on the redox processes within batteries. Therefore, a central goal of this thesis is to establish key observables that reliably describe charge transfer processes at the Li|electrolyte interfaces (2-dimensional) and interphases (3-dimensional) and may be utilized to further tailor the electrochemical performance of Li metal batteries (***Figure 1***). In particular, interphase resistances are analyzed with electrochemical impedance spectroscopy, where the distribution of relaxation times is employed to resolve characteristic rates of the underlying charge transfer processes. Also, the benefits of interfacial charge transfer on the occurring Li metal microstructures are evaluated invoking *in situ* ^{7}Li NMR spectroscopy protocols. Lastly, the future potential of polymer-based Li metal batteries is critically discussed based on scaling projections from common laboratory cells to larger, more application-oriented batteries.

2. Fundamentals

Despite their complexity, rechargeable batteries have been developed already in the mid of the 19th century, when Wilhelm Sinsteden and Gaston Planté invented the lead acid battery.[5] 50 years later, Thomas Edison presented an early nickel||iron "storage battery" for exploitation in electric vehicles, including cars and buses.[6] Remarkably, distances of over 200 km could be achieved with a single charge, though at an average velocity of only 16 km h^{-1} and a specific energy of 30 Wh kg^{-1}.[6] The following chapter provides a fundamental framework to explored concepts on how to enhance current cell chemistries. Basic principles of electrochemical energy storage in batteries are briefly summarized, highlighting the origin of cell voltage and capacity, as well as introducing important quantities to describe salient features of batteries. In addition, the formation of solid electrolyte interphases on Li metal is discussed, followed by a brief overview of polymer electrolytes and charge transfer kinetics at electrode|electrolyte interfaces. Finally, relevant characterization techniques and mathematical methods to monitor and access key properties of the considered cell systems are presented.

2.1 Electrochemical fundamentals

In batteries, energy can be ideally reversibly stored and released through electrochemical reactions, which convert electrical energy into chemical energy and vice versa. To understand the fundamentals behind this immensely useful phenomenon, it is worthwhile to simplify the battery and break it down to its major components. For simplicity, one may consider two metal rods, one zinc and one copper rod, plugged into a lemon (***Figure 2a***).

(a) (b)

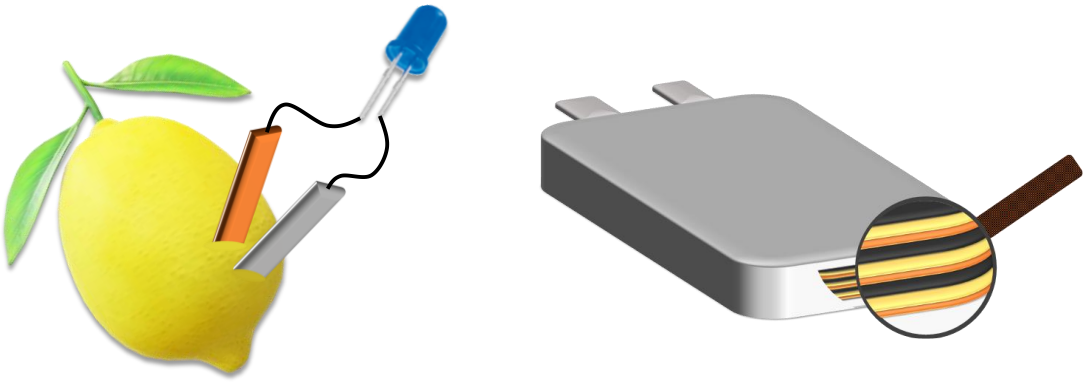

Figure 2*: a) Simplified scheme of a lemon battery consisting of a copper and zinc metal rod (orange and grey, respectively), wires and an electrical load (blue LED), as well as the lemon. Note that in practice, high internal resistances and low cell voltages require multiple lemon batteries connected in series to actually operate the LED (3.2 V, 20 mA). b) Exemplary "pouch-type" battery comprising multiple layers of active materials including cathodes (black), anodes (orange) and electrolyte (yellow).*

Once the metal rods are connected to an external load, current can be drawn from the "battery" and a voltage can be obtained. The metals take the role of electrodes (sites for electrochemical reactions), whereas the citric acid as part of the lemon constitutes an aqueous electrolyte that transports ions (and thereby charges) from one metal electrode to the other. At its core, the lemon battery and a commercial "pouch-type" battery such as depicted in ***Figure 2b*** are much alike, with a main difference of rather reversible charging/discharging capability of the latter ("rechargeable battery") accounting for exploited cell chemistries and electrode materials. This brings up two critical questions that will be answered on the following pages: 1) What is the origin of a cell voltage and 2) What drives (electro-)chemical reactions and resulting currents?

2.1.1 The origin of cell voltage and current

When a metal is immersed into a solution (e.g. the lemon juice), two substances with different electronic states share an interface and a so-called *electrode potential* is established. To understand why this is indeed the case, one may consider the energetic states of the electrons in the metal and in the ions in the solution. In the metal, the electrons are delocalized and fill the electronic conduction bands continuously up to the characteristic maximum, known as Fermi level‡. For the ions in the solution, the electronic energy levels relate to the unfilled molecular orbitals and take discrete values. The lower electronic energy levels of these two phases are favored by the electrons and thus, the energy difference is the driving force of the electron transfer. After some time, the electron transfer reactions reach a point of equilibrium, where both directions of the reaction are equally likely, occurring at similar rates. In spite of the electrochemical equilibrium, charge separation between the metal and the ions in the solution cause differences between the electric potentials, and thus, an electrode potential is established.[9] So far, only one metal dipped in solution was considered. To understand what happens if this metal is electronically connected to another metal with a different electron energy (Fermi energy) that is immersed in the same solution, consideration of thermodynamics helps. The laws of thermodynamics give an indication of the directions of chemical reactions. At constant pressure and temperature, the change in the Gibbs energy ('free energy') indicates the spontaneity of chemical reactions.[10] Under standard conditions (here, at a constant pressure of 1 bar), the change in standard Gibbs energy of a reaction, $\Delta_r G^{\ominus}$, is given in Eq. (1), where T is the temperature, and $\Delta_r H^{\ominus}$ and $\Delta_r S^{\ominus}$ are the change in standard reaction enthalpy and entropy, respectively. The change in reaction enthalpy can be understood as the amount of heat that is generated from or required for a chemical reaction and is equal to the

‡ The Fermi level (or Fermi energy) is defined as the energy of the topmost filled band at 0 K. At temperatures above 0 K, the chemical potential of the electrons is the more precise term, representing the energy level at which the probability of occupation is exactly 0.5 (Fermi-Dirac distribution).[7] For metals, the difference between the chemical potential and the Fermi energy is often negligible even at room temperature.[8]

change in inner energy plus the work associated with volume (or pressure) changes. The change in reaction entropy is a measure of the energy dispersed.

$$\Delta_r G^{\ominus} = \Delta_r H^{\ominus} - T\Delta_r S^{\ominus} \qquad (1)$$

Chemical reactions involve the change of substances, and the potential of a substance to undergo such a change is called *chemical potential* μ. The relation between the Gibbs energy and chemical potential becomes clear when considering the addition or removal of an infinitesimal amount $\mathrm{d}n$ of the substance from a location (spatial or phase) with the chemical potential μ. Then the Gibbs energy changes by $\pm\mu\mathrm{d}n$, where the negative sign corresponds to a removal of the substance and the positive sign to an addition. Thus, the chemical potential is defined as the change in the Gibbs energy with respect to the amount of a substance (Eq. (2)).[9]

$$\mu_j = \left(\frac{\partial G}{\partial n_j}\right)_{T,n_i \neq n_j} \qquad (2)$$

So far, the chemical reactions were of the form $aA + bB + \ldots \rightleftharpoons xX + yY + \ldots$, where $A, B, \ldots$ are the educts and $X, Y, \ldots$ are the products. In electrochemical reactions, electrons are present on either the educt or the product side, and are actively added to or removed from the system. As not only substances, but also charges are involved, the electric potential ϕ of the environment can no longer be neglected and the *electrochemical potential* $\bar{\mu}_j$ of a substance is defined accordingly (Eq. (3)). Here, z_j is the charge (valency) of the involved species and F is the Faraday constant ($F = 96485.3\ \mathrm{C\ mol^{-1}}$).[11]

$$\bar{\mu}_j = \mu_j + z_j F\phi \qquad (3)$$

If two metals with different electrochemical potentials are electronically connected and immersed into the same solution (thereby creating two half-cells with established electrode potentials), the difference of the electrochemical potentials drives an electrochemical reaction and the energy change of the reaction is given by Eq. (4).[12]

$$\Delta G = \left(\sum_i z_i \bar{\mu}_i\right)_{\mathrm{right}} - \left(\sum_i z_i \bar{\mu}_i\right)_{\mathrm{left}} \qquad (4)$$

Here the terms right and left are chosen arbitrarily. In case the right half-cell is the one with the lower electrochemical potential, ΔG is negative and electrons will tend to flow from the left to the right electrode. Upon addition of a potentiostat to the electrical circuit, a voltage can be measured that equilibrates to a characteristic value, the open circuit voltage (OCV). The OCV (denoted as potential difference ΔE) is proportional to the Gibbs energy (Eq. (5)), where z is the number of electrons transferred per single reaction.

$$\Delta G = -zF\Delta E \qquad (5)$$

With the driving forces of the reaction and the origin of the cell voltage at hand, it is now time to clarify how an electric current can be drawn from the reaction. In fact, the rate of consumption or production of species is directly related to the current, as described by Faraday's law (Eq. (6)). Here, m_i is the mass of species i, M_i is its molar mass, I the current, and t the time.[12]

$$m_\mathrm{i} = -\frac{s_i M_i I t}{z\,F} \qquad (6)$$

In practice, Faraday's law is immensely useful when calculating the expected current from the active mass of electrodes. However, one should keep in mind that Eq. (6) exclusively holds for faradaic currents, i.e. those related to (reversible) electrochemical (charge transfer) reactions. In batteries, capacitive and parasitic currents are not negligible, especially when considering interfacial changes and irreversible side reactions.

2.1.2 Charge transfer kinetics (Faradaic currents)

When applying an external current or voltage to a battery, it is forced out of equilibrium and the voltage changes. In this chapter, the relation between current and voltage is explored, considering deviations from thermodynamic equilibrium conditions. The voltage deviation from open circuit voltage is called overvoltage (or overpotential, if measured against a reference), and in the following pages particularly refers to the overpotential due to electrode surface reactions. Other overpotentials may occur due to capacitive currents or concentration gradients that are only indirectly linked to the kinetics of the reactions. In contrast to a simple ohmic resistor, the relation between current and surface overpotential is nonlinear in batteries, owing to the underlying chemical reactions. This is the case, since the rates of the electrochemical reactions at an electrode strongly depend on its potential.[11] The fundamental relation between current and overpotential is often derived from the Butler-Volmer model of charge transfer kinetics. One assumption is that the rate constant k describing the underlying (one-step and one-electron) reactions is thermally activated and hence depends exponentially on the temperature T and Gibbs energy (barrier for oxidation or reduction, $\Delta G^{\ddagger}$), thus following an Arrhenius-type behavior (Eq. (7)).[11]

$$k = A' e^{-\Delta G^{\ddagger}/\bar{R}T} \qquad (7)$$

Here, A' is a pre-factor and $\bar{R}$ is the universal gas constant ($8.314\ \mathrm{J\,mol^{-1}K^{-1}}$). Introducing a standard rate constant k^0 and distinguishing between forward and backward reactions with rate constants k_f and k_b, respectively, one can express the two rate constants as shown in Eq. (8) and Eq. (9).

$$k_\mathrm{f} = k^0 e^{-\alpha f (E - E^{0\prime})} \tag{8}$$

$$k_\mathrm{b} = k^0 e^{(1-\alpha) f (E - E^{0\prime})} \tag{9}$$

The parameter α is the *transfer coefficient* (dimensionless number between 0 and 1), f is a constant ($f = F/\bar{R}T$) and E is the measured potential. As a point of reference, $E^{0\prime}$ is chosen and describes the formal potential (where the concentrations of oxidized and reduced species are equal). As discovered by Nernst, the equilibrium potential E_eq (or open circuit potential) deviates from the formal potential and depends on the bulk concentration of the oxidized (C_O^*) and reduced species (C_R^*), as shown in Eq. (10) for a one-electron reaction ($z = 1$).

$$E_\mathrm{eq} = E^{0\prime} + \frac{\bar{R}T}{F} \ln \frac{C_\mathrm{O}^*}{C_\mathrm{R}^*} \tag{10}$$

Considering kinetic rate constants from Eq. (7) for oxidation and reduction and the equilibrium potential from Eq. (10), one can derive the *current-overpotential equation* (Eq. (11)). A detailed derivation can be found in Bard & Faulkner's book *Electrochemical Methods*.[11] The surface overpotential $\eta = E - E_\mathrm{eq}$ is defined to describe the deviation of the actual potential and the equilibrium potential. Note that the currents are normalized to the macroscopic electrode area, thus are to be understood as current densities with the unit mA cm^{-2}.

$$i = i_0 \left[\frac{C_\mathrm{O}(0,t)}{C_\mathrm{O}^*} e^{-\alpha f \eta} - \frac{C_\mathrm{R}(0,t)}{C_\mathrm{R}^*} e^{(1-\alpha) f \eta} \right] \tag{11}$$

An important quantity is introduced, the *exchange current density* i_0, which describes the current density at equilibrium, i.e. the faradaic activity when the net current is zero. Also, the concentrations at the electrode surface ($C_\mathrm{O/R}(0,t)$) are assumed to change over time due to mass transfer from and to the electrodes. When no considerable mass transfer is apparent (e.g., at low enough current densities), the surface concentrations and bulk concentrations are approximately equal, so that the historically known *Butler-Volmer equation* is achieved (Eq. (12)).

$$i = i_0 \left[e^{-\alpha f \eta} - e^{(1-\alpha) f \eta} \right] \tag{12}$$

For small deviations from the equilibrium potential, the exponential functions can be linearized, such that the current (density) is proportional to the overpotential (Eq. (13)) and a charge transfer resistance can be defined (Eq. (14)). The negative sign results from the arbitrary definition of the difference of anodic and cathodic current and is disregarded for the expression of R_ct.

$$i = -i_0 f \eta \tag{13}$$

$$R_{\mathrm{ct}} = \frac{\bar{R}T}{Fi_0} \tag{14}$$

The Butler-Volmer theory of charge transfer relies on the phenomenological parameters k^0 and α and does not consider molecular effects of the charge carrier environment, such as the solvent surrounding the reaction species. Here, the Marcus-Hush theory of charge transfer comes into play.[11] Consider the reaction of $\mathrm{Li}^+ + e^- \rightleftharpoons \mathrm{Li}^0$, where a solvated Li ion reduces to elemental Li at an electrode (***Figure 3***). In the oxidized state (O), the Li ion is surrounded by solvent molecules and the free energy of this configuration is given by $\Delta G_{\mathrm{O}}^0(q_{\mathrm{O}})$.

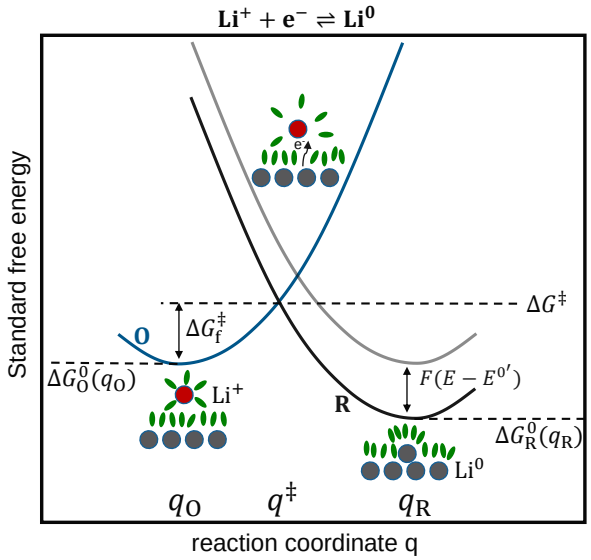

Figure 3: *Standard free energies ΔG of activation for the reaction of $Li^+ + e^- \rightleftharpoons Li$ at different Marcus reaction coordinates q_R, q_O and the transition state $q^{\ddagger}$. R is the reduced state, O is the oxidized state.*

In equilibrium, the free energy of the reduced state (R) is equal to that of the oxidized state. To force an actual reaction, the electrode potential is lowered, such that the free energy of the reduced configuration, $\Delta G_{\mathrm{R}}^0(q_{\mathrm{R}})$, is lower than that of the oxidized state. The reaction occurs via a transition state, denoted with the reaction coordinate $q^{\ddagger}$. Marcus showed that along the reaction path, the free energies of the two configurations depend quadratically on the reaction coordinate.[11] Thus, they can be expressed by Eq. (15) and Eq. (16), where the constant $\bar{k}$ can be understood as a force constant.

$$\Delta G_{\mathrm{O}}^0(q) = \frac{\bar{k}}{2}(q - q_{\mathrm{O}})^2 \tag{15}$$

$$\Delta G_{\mathrm{R}}^0(q) = \frac{\bar{k}}{2}(q - q_{\mathrm{R}})^2 + F(E - E^{0\prime}) \tag{16}$$

To derive the free energy of the reduction, $\Delta G_{\mathrm{f}}^{\ddagger}$, the cross-over point of both parabolas can be straightforwardly determined by setting $\Delta G_{\mathrm{O}}^0(q^{\ddagger}) = \Delta G_{\mathrm{R}}^0(q^{\ddagger})$, solving for $q^{\ddagger}$ and inserting in

Eq. (15) or Eq. (16). The resulting Eq. (17) can further be simplified by defining a structural reorganization factor $\lambda_\mathrm{r} = (\bar{k}/2)(q_\mathrm{R} - q_\mathrm{O})^2$, yielding Eq. (18).

$$\Delta G_\mathrm{f}^\ddagger = \frac{\bar{k}(q_\mathrm{R} - q_\mathrm{O})^2}{8}\left[1 + \frac{2F(E - E^{0\prime})}{\bar{k}(q_\mathrm{R} - q_\mathrm{O})^2}\right] \tag{17}$$

$$\Delta G_\mathrm{f}^\ddagger = \frac{\lambda_\mathrm{r}}{4}\left[1 + \frac{F(E - E^{0\prime})}{\lambda_\mathrm{r}}\right] \tag{18}$$

The implications of this result for the Butler-Volmer model become clear when deriving an expression for the transfer coefficient α. From rearranging Eq. (8) and Eq. (7), one can derive that the transfer coefficient can be expressed in general as shown in Eq. (19).

$$\alpha = \frac{1}{F}\frac{\partial \Delta G_\mathrm{f}^\ddagger}{\partial E} \tag{19}$$

Since, according to the Marcus-Hush derivations, $\Delta G_\mathrm{f}^\ddagger$ depends on the potential E, the transfer coefficient α is no longer constant, but depends on the applied potential, as demonstrated in Eq. (20).

$$\alpha = \frac{1}{2} + \frac{F(E - E^{0\prime})}{2\lambda_\mathrm{r}} \tag{20}$$

The reorganization energy λ_r is a scaling factor that describes the energy required for the reorganization of the solvent molecules upon the reaction. Typical values for liquid electrolytes are $\lambda_\mathrm{r} \approx 0.3\ \mathrm{eV}$.[13]

2.1.3 Capacitive (non-faradaic) currents

When the potential of an electrode is changed due to an external bias, the resulting current does not exclusively occur due to electrochemical reactions. A part of the current (or change in voltage) is caused by the charging/discharging of the electrochemical double layer that acts as a capacitor. ***Figure 4*** visualizes the double layer, which is caused by the separation of positive and negative charges in the vicinity of the electrically charged electrode. Close to the electrode, a layer of adsorbed solvent molecules forms the inner Helmholtz plane (IHP), followed by the solvated cations (in case of a negatively charged electrode) which create the outer Helmholtz plane (OHP). The anions remain farther away from the electrode due to electrostatic repulsion, but still remain relatively close due to diffusion and form the outer part of the double layer (diffusive layer). In the bulk electrolyte, charge neutrality is given and ideally, no concentration gradient occurs. In case of an ideally polarizable electrode that does not allow electrochemical reactions, the current can be compared to that required to charge a capacitor.

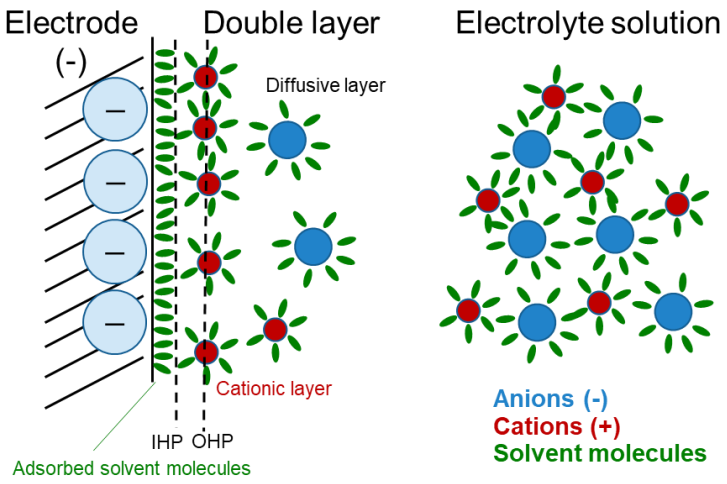

Figure 4: *Formation of an electrochemical double layer at an electrode that is negatively charged. The inner Helmholtz plane (IHP) and the outer Helmholtz plane (OHP) denote the first part of the double layer. Figure adapted from ref.*[11]

Consider the application of a constant potential E_0 to a cell with ideally polarizable electrodes and an electrolyte solution with bulk resistance R_b. In this case, the (differential) Eq. (21) holds, as a result of $q(t) = C_\mathrm{dl}U(t)$, $U(t) = i(t)R_\mathrm{b}$ and $dq/dt = -i(t)$, where $q(t)$ is the amount of charges stored in the double layer, C_dl is the double layer capacitance, $U(t)$ is the time dependent voltage.[11]

$$i(t) + R_\mathrm{b}C_\mathrm{dl}\frac{\mathrm{d}i(t)}{\mathrm{d}t} = 0 \qquad (21)$$

Through separation of variables and defining the boundary condition $i(0) = E_0/R_\mathrm{b}$, a solution for this equation is of exponential form (Eq. (22)), where the characteristic time constant $\tau = R_\mathrm{b}C_\mathrm{dl}$ defines the time when the magnitude of current reached ca. 37 % of the original current.

$$i(t) = \frac{E_0}{R_\mathrm{b}}e^{-t/R_\mathrm{b}C_\mathrm{dl}} = \frac{E_0}{R_\mathrm{b}}e^{-t/\tau} \qquad (22)$$

In case of non-blocking electrodes, currents from charge transfer reactions (i_f) contribute to the overall current, such that a more generalized expression is given in Eq. (23).[12]

$$i = i_\mathrm{f} + C_\mathrm{dl}\frac{\mathrm{d}\eta}{\mathrm{d}t} \qquad (23)$$

2.2 The lithium metal anode

Metal electrodes were already key active parts of early stage primary (non-rechargeable) and secondary (rechargeable) batteries attributed to their high specific capacity (charges per unit mass) and often low reduction potentials (tendency to gain or lose electrons).[6,14] Since metals typically exhibit negative reduction potentials vs. standard hydrogen electrode (SHE), they are often employed as anodes rather than cathodes.[3] In this chapter, the exploitable properties of Li metal as electrode material are summarized, showcasing why Li metal is among the most

prospective metals for next-generation batteries that afford higher energy densities than contemporary Li ion batteries.

2.2.1 Lithium as metal electrode

Among all technically considered metal anodes, Li metal constitutes a most promising solution due to its exceptionally low standard reduction potential (-3.04 V vs SHE) and high specific capacity (3861 mAh g^{-1}). While other alkali and earth alkaline metals such as sodium (Na), potassium (K), calcium (Ca), or even magnesium (Mg) offer reasonably low reduction potentials below -2.0 V vs. SHE, none of them is capable of storing nearly as much charge per unit mass as Li (***Figure 5a***). Aluminum (Al) is closest with 2205 mAh g^{-1}, yielding only 57 % of the capacity of Li. The combination of both reduction potential and capacity eventually governs how much energy can be stored within the cells. Besides the storable charges per unit mass (specific capacity), the storable charges per unit volume are of interest for battery applications. Instead of presenting the charge density in units of mAh cm^{-3}, for better comparison, the values are converted into a theoretical layer thickness in ***Figure 5b***. The thickness can be understood as a measure of the volume expansion per unit area and charge and is derived from Eq. (24), where q_{spec} is the specific capacity in mAh g^{-1} and ρ is the density in g cm^{-3}.

$$d\ (\text{in } \mu\text{m}) = \frac{1\ \text{mAh cm}^{-2}}{q_{\mathrm{spec}}\,\rho} \cdot 10^4 \qquad (24)$$

For example, the (minimal) thickness of Li metal that provides an areal charge capacity of 1 mAh cm^{-2}, at a density of 0.534 g cm^{-3}, and specific capacity of 3861 mAh g^{-1} amounts to only $d = 4.8\,\mu\text{m}$. In practice, batteries may exhibit areal charge capacities of up to 4 mAh cm^{-2}, thus a total Li thickness of almost 20 µm (under ideal conditions) is deposited upon charging, in this way contributing to the overall volume expansion during cell operation.[15] Note that the actual thicknesses may be even larger, as electrochemical metal deposits are often less densely packed than pristine metals.[16] Alternative alkali metals such as Na and K exhibit lower charge densities, hence resulting in metal deposit thicknesses of 8.8 µm and 16.9 µm, respectively. Al offers the highest charge density due to its trivalent nature and comparably high density of 2.7 g cm^{-3} and thus yields a thickness of as low as 1.2 µm. However, a formation of ionically non-conductive passive layers on the metal electrode currently presents a major challenge for Al-based batteries.[17]

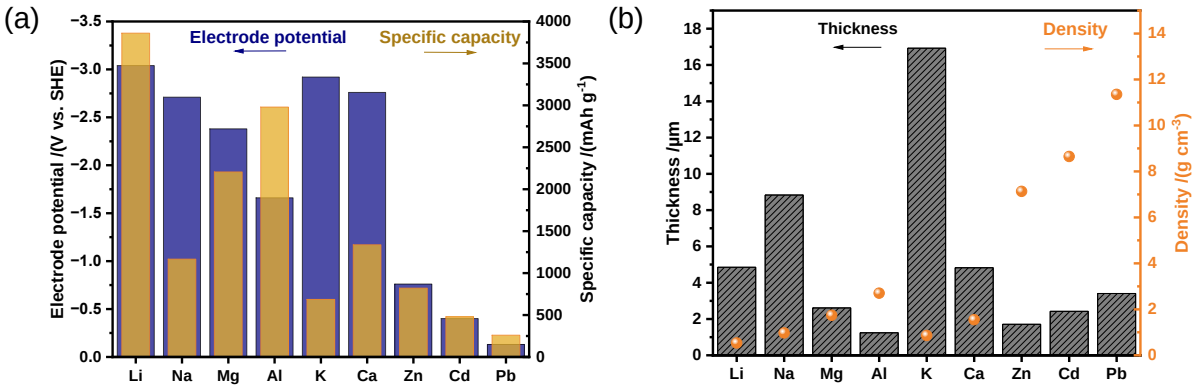

Figure 5: *(a) Standard reduction potentials in V vs. standard hydrogen electrode (SHE) and specific capacities of various metals. (b) Theoretically expected layer thickness per areal charge capacity of 1 mAh cm^{-2} and density of the corresponding metals.*

Compared to conventional Li ion batteries, a Li metal battery is substantially thinner, as demonstrated by exemplary single-layer cell stacks in ***Figure 6***. The Li anode provides, in most cases, an excess reservoir, as all active charges (Li ions) are initially stored within the cathode and deposited upon charging on the anode. Thus, in principle, the initial metal anode could be fully omitted and a current collector could serve as nucleation site. This so called “anode-free” or “zero-access” cell set-up would enable the highest available energy densities, but in practice is plagued by fast capacity fading due to interfacial reactions and formation of electrochemically isolated “dead Li” fractions.[18,19] Therefore, the excess Li reservoir yields an additional source of Li ions to maintain reversible charging/discharging until electrode interphases are stabilized.

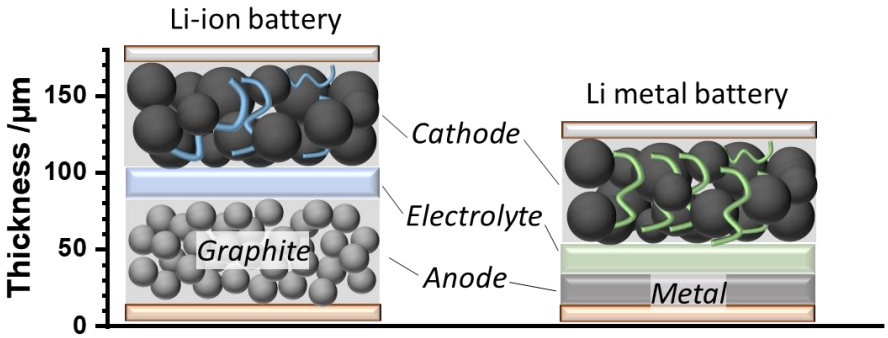

Figure 6: *Comparison of single-layers of typical Li ion and Li metal batteries. Redrawn from Duffner et al.[20] Parts of the electrolyte are contained in the cathode (thus acting as catholyte).*

Niu et al. reported that a ratio of excess anode capacity to cathode capacity of 1:1 is beneficial to achieve a compromise between the conflicting demands of cycling efficiency and energy density.[21] In case of Li metal electrodes and a cathode capacity of 4 mAh cm^{-2}, the excess Li foil should then have an estimated thickness of 20 µm to fully compensate for any capacity losses due to side reactions upon cycling.

2.2.2 The solid electrolyte interphase

Both spontaneous and electrochemically induced side reactions inevitably cause the formation of solid layers of reaction products at the electrode surfaces in electrochemical cells. What seems undesired at first sight, is in fact quite essential for robust battery operation.[22] The layers are often ionically conductive and electronically insulating, thus they act as solid electrolyte layers that ideally prevent further electrolyte degradation. The term solid electrolyte interphase (SEI) refers to the layers that form at the anode side (***Figure 7***), while those at the cathode side are termed as cathode electrolyte interphases (CEI).[23] The SEI on metal anodes (and especially Li metal) is often composed of inorganic components that typically build up close to the electrode surface, while organic (often softer) products are accumulated closer to the electrolyte. With thicknesses of 10 nm to 100 nm, the SEI layers on Li metal are thin compared to bulk electrolyte thicknesses of tens of µm.[24] Contrary to SEIs on graphite electrodes, the SEI layers on Li metal have to compensate for the substantial volume changes during charging and discharging. Sufficient charge transport (high ionic conductivity) and mechanical robustness of the SEIs are required to prevent a filamental growth of Li through towards the counter electrode, which eventually shorts the cell.

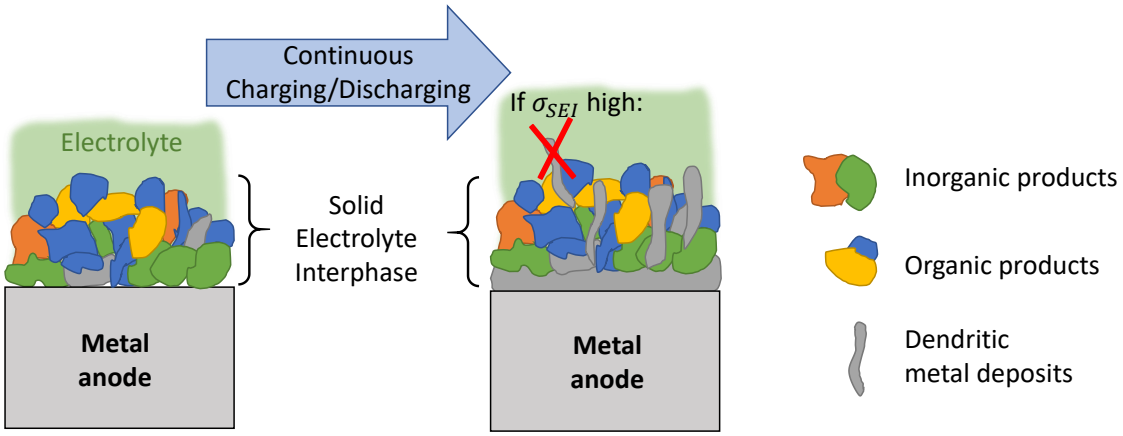

Figure 7: *Schematic representation of the solid electrolyte interphase (SEI) on a metal anode. Upon continous charging and discharging of the battery, metal is deposited below the SEI, which prevents filamental growth of metal deposits, if the ionic conductivity σ_{SEI} is large enough.*

2.2.3 Strategies for homogeneous Li deposition

Achieving homogeneous Li deposition can perhaps be considered as the holy grail when developing Li metal batteries. Various strategies have been developed in the last decades, including coatings, modification of electrolyte constituents (additives), as well as completely novel electrolytes. The motivation for coatings is that the native SEI on Li metal is too brittle to enable reversible deposition and dissolution and that the artificial SEI enables a more homogeneous deposition/dissolution. Here, the challenges lie in the compromise between

adding resistive layers to the system and achieving more homogeneous depositions. Ideally, the coating does not increase the internal resistance (or even decreases it), while increasing the flexibility of the interphase. The volume change due to Li metal is inevitable and needs to be tamed as much as possible (5 µm per mAh cm^{-2}). Polymers may serve as artificial layers to improve interfacial contacts, Li compatibility and reversibility of the Li inventory.[25] Various design strategies have been suggested, including polyurethane-based flexible polymers, which could be tuned based on their two major components (one structural and one ionically conductive component).[26] Another coating layer comprised Li polyacrylate with an impressive elasticity that could stretch up to 580 % to withstand the large Li volume expansion.[27]

2.3 Polymer electrolytes

The role of the electrolyte is fundamental to the overall electrochemical performance of cells, as it ultimately limits the actual reaction rates by transporting charges between the electrodes. Typically, electrolytes are classified based on their material characteristics, e.g. liquids, inorganic solids and organic solids (polymer electrolytes). In many applications, the electrolyte is a hybrid version of these, for example a combination of liquid components with a polymer matrix (gel electrolytes). While all three classes have particular benefits and challenges, the focus is set on polymer electrolytes in this thesis. Four important topics can be identified that characterize the electrolyte (***Figure 8***). First, the electrolyte serves as ionic conductor, thus the ion transport is a main concern when developing new electrolytes. Quantities describing the ionic transport comprise the ionic conductivity, transference number, diffusion coefficient, as well as the thermodynamic factor, which is related to the salt activity coefficient.[28] While the charge transport through the bulk electrolyte is important, the charge transfer at the electrode/electrolyte interface is also crucial. Here, interface compatibility is important. In case of Li metal, the surface is subject to permanent volume changes and highly reactive, thus prone to undesired side reactions. Low interfacial resistances are desired. Furthermore, electrolytes need to be both sufficiently stable (electrochemically and mechanically), as well flexible to accompany for external forces. The solvent uptake of gel polymer electrolytes, as well as the operating temperature are important parameters that eventually govern the mechanical stability (e.g. the elastic modulus). Lastly, electrochemical performance is governed by reversible processes, thus losses of active material should be kept to a minimum.

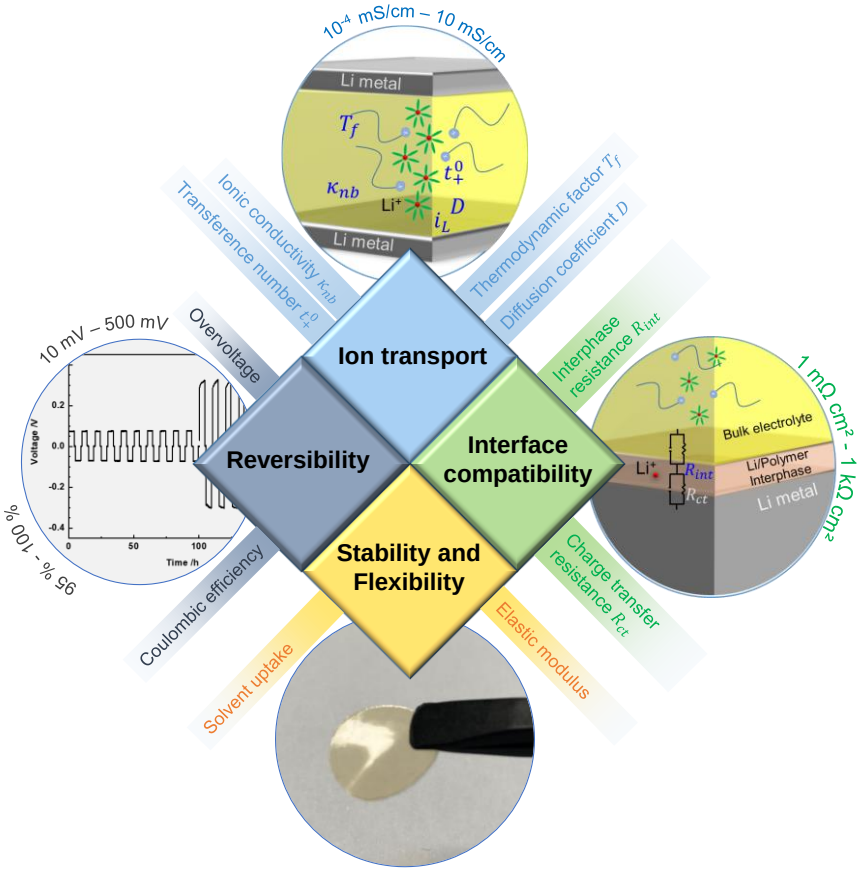

Figure 8: *Important properties and associated quantities of polymer electrolytes used in rechargeable Li metal batteries.*

2.3.1 Charge transport in the electrolyte

The electrolyte primarily transports charge carriers among the electrodes to sustain ongoing electrochemical reactions. In conventional liquid electrolyte systems, a porous separator (e.g. poly propylene foil[29]) is required to prevent electronic contacts between the electrodes. Solid electrolytes, such as polymers or inorganic ceramics often substitute the porous separator, as they exhibit sufficient mechanical rigidity to separate the anode from cathode. Note that the ionic transport is typically described by the ionic conductivity ($[\sigma] = 1\,\mathrm{S\,cm^{-1}}$), which is a measure of the conductivity of electric (here ionic) particles in an electric field. From the equations of electrodynamics, in particular Ohm's law, it is apparent that the ionic conductivity in the one-dimensional case is a constant of proportionality between the electric current density i and the electric field ***E***. In simple terms, a high conductivity in an electric field results in a high current density (charge flow per time and area, $[i] = 1\,\mathrm{mA\,cm^{-2}}$). Since electrochemical reactions rely on mass transport from and to the electrodes, another driving force of ionic transport is the concentration gradient and resulting diffusion of mobile species. A combination of the four *transport properties*, including ionic conductivity, cation transference number,

mutual salt diffusion coefficient, and the thermodynamic factor, gives a complete overview of the ionic transport in electrolytes.[28]

Ionic charge transport of polymer electrolytes is different from charge transport within liquid or ceramic electrolytes. Charge transport in liquid electrolytes (***Figure 9***) is often assisted by the solvent molecules that cause a vehicular transport of the ion surrounded by solvation shell, or by hopping from one solvation environment to the other.[30,31] Typical coordination numbers for the solvation are between 4 and 6 solvent molecules per Li^+ ions.[32] Solvents are often mixtures, examples of solvents are ethylene carbonate (EC) offering high dielectric permittivity (good solubility of Li), dimethyl carbonate, diethyl carbonate, and ethylmethyl carbonate, all of which are low viscosity solvents to facilitate ion transport.[33] Notably, compared to most solid and polymer electrolytes, liquid electrolytes require a porous separator to physically divide the electrode compartments and prevent a short circuit. Typical materials of separators include polyethylene, polypropylene, and polyamide.[29] The impact of the non-conductive separator on the ionic conductivity is generally not negligible and is typically expressed in terms of the MacMullin-Number, which is the ratio of the pure electrolyte conductivity and the effective conductivity (electrolyte and separator).[34,35] MacMullin numbers of separators should be below 8 for operation in batteries[36], though the reported values of the common separator membrane Celgard2500 are between 6 and 23. The large range of values likely reflects the use of different electrolytes and characterization techniques.[37,38]

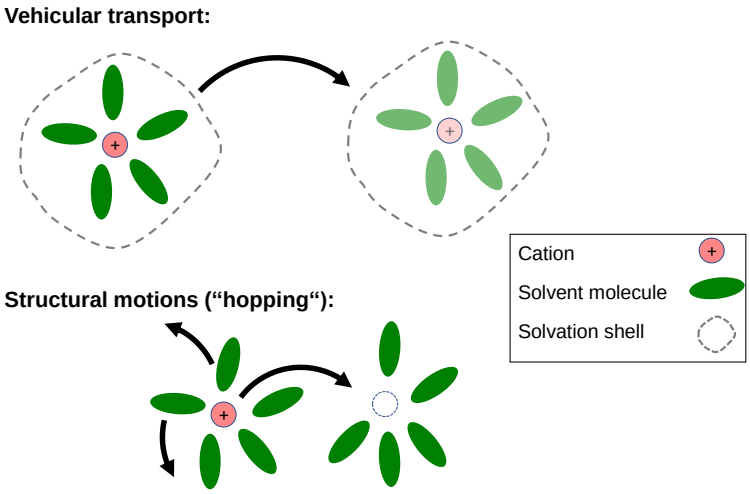

Figure 9*: Common types of ionic charge carrier transport in liquid electrolytes, including solvation shell-supported vehicular transport and "hopping" of ions through structural motions.[31] Salt anions are not shown for simplicity, but may also contribute to overall charge transport.*

In polymer electrolytes, segmental motion but also intra chain dynamics of the polymer chains are often the dominating mode of charge transport, as visualized in ***Figure 10***.[39] Elucidating the mode of charge transport is key to enhance it, as for example the amount of segmental

motion strongly depends on the mechanical properties of the polymer electrolyte, which in turn depend on temperature. Therefore, many fully dry polymer electrolytes are operated above or close to their melting point at elevated temperatures (e.g., 60 °C).[40]

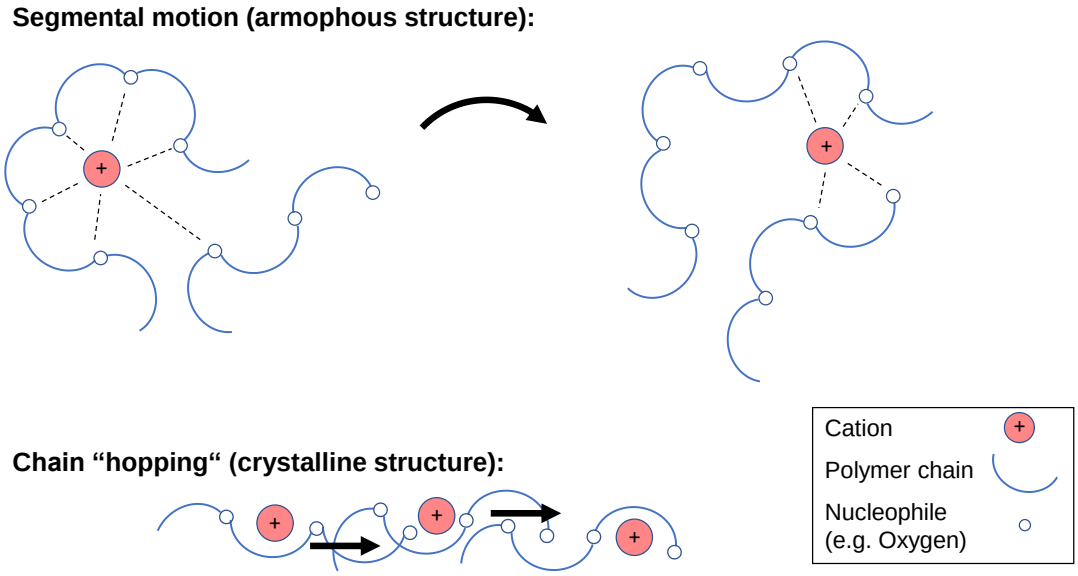

***Figure 10**: Charge transport in amorphous and crystalline (ether-type) polymer electrolytes, where cations move either through segmental motion of polymer chains or "hopping" through crystalline polymer tunnels.[41] Salt anions are not shown for simplicity.*

Compared to dry polymers, gel polymer electrolytes contain flowable components such as solvents that facilitate charge transport and operation at lower temperatures (e.g. 20 °C). Bocharova et al. proposed that besides gel polymer electrolytes, composite polymer electrolytes (e.g., ceramic-polymer composites or combinations with ionic liquids) may also enable higher conductivities by decoupling the ion dynamics from segmental relaxation.[42]

2.3.2 Single-ion conducting polymer electrolytes

Since mobile ions in the electrolyte migrate in the apparent electric field upon battery operation, concentration gradients occur. For example, the anions migrate away from the negatively charged electrode under the influence of the electric field (***Figure 11***). When the applied current density is high and the anions are mobile enough, the resulting concentration gradient may eventually cause a depletion of anions at the negatively charged electrode. Chazalviel developed a model that related the anion drift velocity (a quantity that is also related to the mobility of the anions) to the growth rate of Li metal deposits.[16] Faster anion drift velocities (i.e. at higher currents or lower transference numbers) thus promote inhomogeneous Li deposition. Single-ion conducting polymer electrolytes present a promising class of polymer electrolytes, as the anions are usually immobilized to the large polymer backbone, thereby preventing cell polarization.[43]

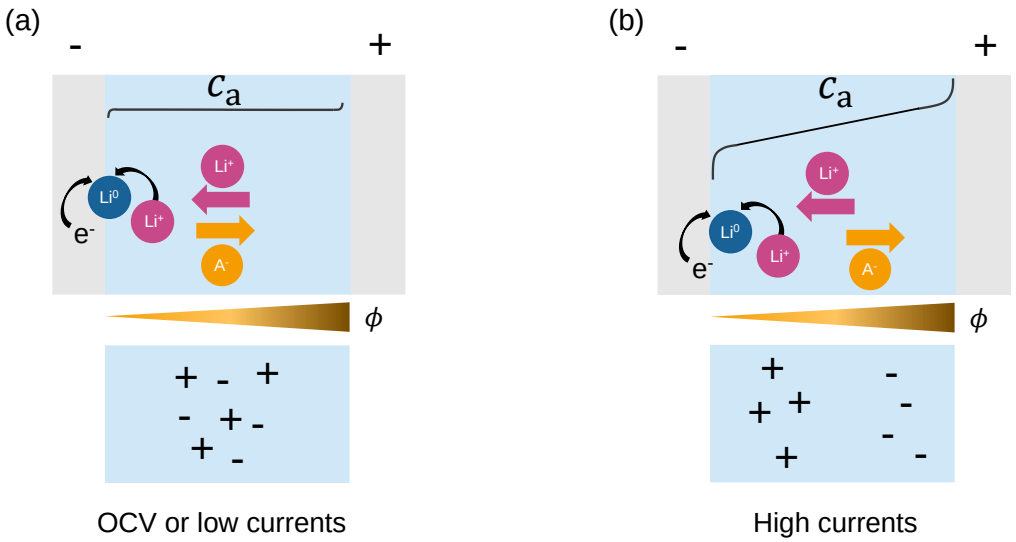

Figure 11: *Anion concentration profile under the influence of an electric field with (a) no polarization and (b) polarization occuring due to charge separation in the bulk electrolyte.*

2.4 Characterization methods

The main characterization methods used in this thesis comprise electrochemical impedance spectroscopy, nuclear magnetic resonance spectroscopy and cyclovoltammetry, which will be briefly introduced in this chapter.

2.4.1 Electrochemical impedance spectroscopy

Electrochemical impedance spectroscopy (EIS) is perhaps one of the most important methods for characterizing electrochemical cells and cell components. In suitable cell and measurement configurations, EIS may provide information about ionic conductivities, internal and interfacial resistances, while only slightly perturbating the considered systems. EIS is based on the principle that the electrical resistance of an electrochemical cell is often frequency-dependent, which becomes apparent when applying an AC voltage or current at different frequencies. Depending on the invoked frequency ranges, the complex resistances (impedances) allow for distinguishing different processes within components of a cell, so that, for example, bulk ionic conductivities of electrolytes can be distinguished from electrode interfacial processes. Typical frequency spectra cover ranges from 1 mHz to 5 MHz at excitation amplitudes of 5 mV to 50 mV in case of potentiostatic EIS. A small amplitude relative to the operating voltage is important to obtain linear current responses, which might not be the case if the systems are perturbed much stronger than a few tens of millivolts. Since the impedance is a complex quantity, each data point at a given frequency includes two values (real and imaginary parts of the impedance, or magnitude and phase angle). Therefore, the impedance of a system is not to be understood as a point value, but as vector with a length ("magnitude") and a direction

("phase angle"). Depending on the frequency, the length and direction of the vector changes, and so does the impedance. Impedance spectra are usually plotted in the complex plane, with the real part on the abscissa and the negative imaginary part on the ordinate. In this parametric form (Nyquist plot), the frequency is only implicitly present as a variable, which should be compensated for by explicitly specifying characteristic, individual frequencies (e.g. maxima). The imaginary part is presented as negative value, as capacitive contributions are more common in batteries than inductive contributions.

A common strategy to evaluate EIS data is the use of equivalent circuit elements. The three basic electrical components are a resistor (resistance $R \propto \omega^0$), a capacitor (capacitance $C \propto \omega^{-1}$) and an inductor (inductance $L \propto \omega^1$). Combinations thereof in series and in parallel may mimic the actual behavior of an electrochemical cell to a certain degree. More advanced circuit elements, which in general are functions in the form of $Z(\omega)$, may be derived from considerations of mass transfer and concentration gradients. Here, the Warburg element is a commonly used element that scales with $\omega^{0.5}$. A constant phase element (CPE) is an element with a variable exponent (ω^{φ}), and is often interpreted as “non-ideal capacitance”.[44]

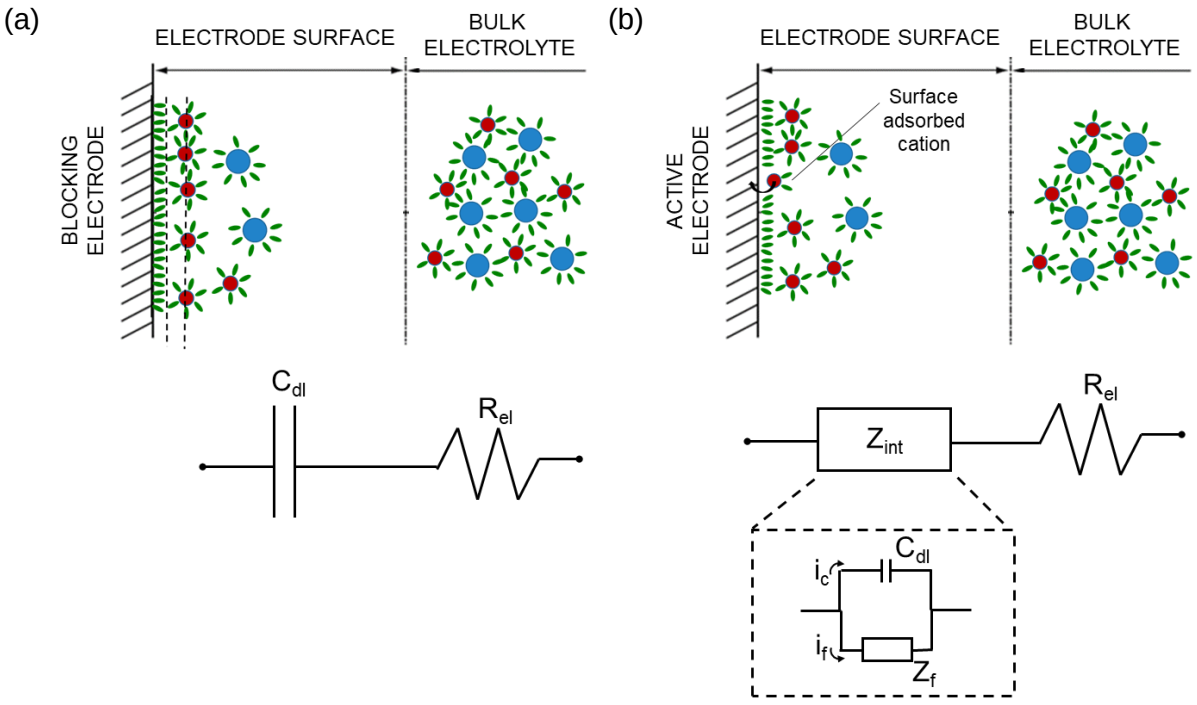

Figure 12: *Schematic visualization of the response of electrolyte constituents to external current or voltage when squeezed between two electrodes that are (a) blocking or (b) non-blocking for electrochemical reactions. The equivalent circuit models are provided below, with the double-layer capacitance C_{dl}, electrolyte resistance R_{el}, interfacial impedance Z_{int}, capacitive (non-faradaic) and faradaic current densities i_c and i_f, respectively, and faradaic impedance Z_f (e.g., charge transfer resistance). Bottom part adapted from Orazem et al.*[44]

In ***Figure 12***, two scenarios of commonly used electrochemical cells are visualized close to the surface of the electrode. In case of blocking electrodes (***Figure 12a***), i.e. when no charge

transfer occurs, the system can be modeled with a simple combination of a resistor and a capacitor, reflecting the bulk electrolyte resistance and the capacitance of the electrochemical double layer, respectively. This double layer inevitably forms when establishing a potential at the electrode and can be interpreted as a capacitive layer that charges and discharges upon passage of currents. The bulk electrolyte resistance represents an inverse ionic conductance, thus it is a characteristic of the charge transport capability of the electrolyte (expressed as the conductivity). In case of non-blocking electrodes (***Figure 12b)***, the interfacial impedance is divided into two contributions: 1) the capacitive currents that cause charging of an electrochemical double layer and 2) the faradaic currents which are associated with electron transfer (e.g. resulting in electrochemical reactions).[11,44] Real electrochemical systems often show non-ideal impedance behavior, in that their response cannot be accurately modeled by simple circuit elements and combinations thereof. Instead, a distribution of time constants (or relaxation times) has to be assumed. The time constants are inverse frequencies ($\tau = 1/(2\pi f)$) and thus reflect characteristic rates of processes (e.g. charge transfer or ionic conduction). For example, the analytical expression of a CPE element in time domain is given in Equation (25), as shown by Macdonald at al.[45]

$$G_{CPE}(\tau) = \frac{1}{2\pi\tau} \frac{\sin((1-\alpha)\pi)}{\cosh \alpha \log\left(\frac{\tau}{\tau_0}\right) - \cos((1-\alpha)\pi)} \qquad (25)$$

Here, $G_{CPE}(\tau)$ is a normalizable distribution function with the dimension s^{-1}, as depicted in Eq. (26) for a general distribution function $G(t)$.

$$\int_0^\infty G(\tau)\, d\tau = 1 \qquad (26)$$

Another distribution function is, for example, a delta function $\delta(\tau - \tau_0)$ that describes a single relaxation time (comparable to that of an RC-circuit). If a thermal distribution of activation energies can be assumed, one may derive that another distribution of relaxation times is lognormal to τ, thus in the form of $\exp(-b^2 \ln\left(\frac{\tau}{\tau_0}\right)^2)$, with b being a temperature dependent parameter.[45] The unit of a distribution of relaxation times often varies in literature due to slightly different definitions. Throughout this thesis, the amplitude of the DRT spectra corresponds to a resistance with the unit $\Omega\mathrm{cm}^2$, such that the integrated absolute area of the spectrum on logarithmic time scales corresponds to the overall resistance.

2.4.2 NMR spectroscopy of batteries

Nuclear magnetic resonance (NMR) spectroscopy works due the phenomenon that nuclei with a nuclear spin different from zero interact with external magnetic fields (Zeeman effect). For simplicity, one may compare the nuclear spin to spinning tops that have an angular momentum. When exposed to a strong external magnetic field, the spins align parallel and antiparallel to

the magnetic field, thereby building up a net magnetization, exhibiting Zeeman splitting of their energetic states. The process of alignment to the magnetic field is called spin-lattice relaxation (T_1 relaxation) and is comparably fast for paramagnetic materials.[46] The spins precess around the z-axis (along the applied magnetic field) with a characteristic frequency, the Larmor frequency, that depends on both the nucleus and magnetic field. For example, at a magnetic flux density of 4.7 T, the Larmor frequency of ^{7}Li is 77.8 MHz. The magnetized spin system is now manipulated by radio-frequency (RF) pulses through an RF coil, that is used for both RF pulsing and signal detection. The RF pulse causes a transfer of the magnetization into the xy-plane, where it rotates around the z-axis and thereby induces a measurable voltage. This voltage decays (= free induction decay, FID) due to internal NMR interactions, that comprise, for example, interactions between the nuclear spin and the electron spin (shift interactions) or between nuclear spins (dipolar coupling) and quadrupolar interactions in cases of spins >1/2. The spin-spin relaxation processes that cause the voltage decay are also called T_2 relaxation. The voltage curve (FID) is Fourier-transformed to an intensity-frequency signal and usually referenced against a standard (e.g., tetramethylsilane (^{1}H, ^{29}Si), deuterochloroform (^{1}H, ^{13}C), or Lithium chloride in water (^{6,7}Li)). The difference of signal and reference frequency is further normalized to the spectrometer frequency and given in parts per million (ppm). The utility of NMR spectroscopy in battery science ranges from liquid NMR spectroscopy of electrolyte constituents over solid-state magic angle spinning to *in situ* NMR spectroscopy. As part of this thesis, *in situ* ^{7}Li NMR spectroscopy was performed on Li||Li cells. The shift of Li metal is different from that of ionic Li species due to the Knight shift, that is an interaction of the nuclear spin and that of the conduction electrons. Due to its paramagnetic properties and the orientational dependence of the susceptibility with respect to the external magnetic, bulk magnetic susceptibility (BMS) effects give rise to shifts, so that the orientation of the sample in the magnetic field is highly relevant.[46] In case of Li metal, it was shown that this BMS effect causes a shift of the corresponding Li metal peak, depending on its actual microstructure or "morphology". ^{7}Li NMR shifts towards 270 ppm could be assigned to more dendritic Li metal structures, whereas signal contributions close to 250 ppm reflect more dense or mossy Li deposit species.[47] Notably, the rf field penetrates the Li metal only to a finite thickness, depending on the strength of the static B-field. At a flux density of 4.7 T, the skin depth for Li metal is 17.4 µm, thus larger than the dimensions of most Li metal deposits.[47] A detailed review of NMR spectroscopy in the field of battery research can be found in ref.[46]

2.4.3 Cyclovoltammetry

In voltammetry experiments, the potential of a working electrode is deliberately altered and the resulting change in current is observed. Typically, constant sweep rates (e.g. 1 mV s^{-1}) are applied in a three-electrode set-up (against a reference electrode). Cyclovoltammetry is a

method where the potential of the working electrode is swept forward and backward to investigate occurring oxidative and reductive reactions. ***Figure 13*** visualizes a simplified cyclic voltammogram for a reversible one-step, one-electron redox reaction. Here, the redox reaction of Li ions and Li metal is considered.

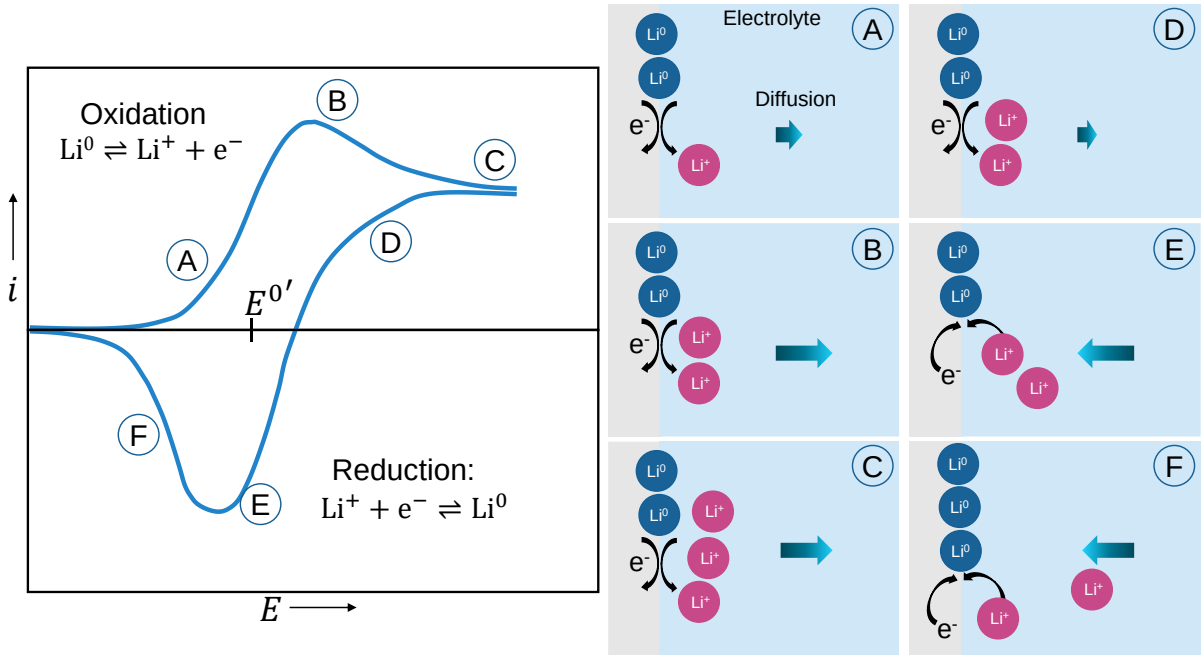

Figure 13: *Simplified cyclovoltammogram of a one-step one-electron reaction, exemplary for the reduction and oxidation of Li^+ and Li, respectively.*

Note that in practice, this reaction is not fully reversible and may vary due to phase transitions and passivating reactions. Initially, the electrode potential is swept forward towards the equilibrium (or more precisely, the formal) potential $E^{0\prime}$. As a result, first capacitive and then faradaic reactions are initiated that cause a measurable current, which increases further, as more and more Li is oxidized to Li^+ ions (point A). Due to the concentration gradient of Li ions at the surface compared to regions farther away from the electrode, the Li ions diffuse away from the electrode. However, diffusion is limited by the electrolyte-specific diffusion coefficient, such that the current reaches a peak maximum. At this point (B), the diffusion of Li ions away from the electrode and the rate of reactions are equal. A further increase of the potential causes an accumulation of Li ions at the electrode surface, such that the reaction is slowed down and the current decreases again (point C). When reversing the sweep rate, an oxidation reaction continues, but the current decreases, as the potential is reversed. Only when the measurable current is negative, the reductive reactions dominate the redox reaction, such that Li ions are reduced to Li metal. This time, Li ions diffuse towards the electrode due to the concentration difference at bulk and electrode surface. The diffusion to the electrode limits the reductive reactions, resulting in a peak current (point E). Further decreasing of the potential causes a depletion of Li ions at the electrode, such that the current decreases (point F). Further

information about voltammetry can be gathered from Compton and Banks' comprehensive book *Understanding Voltammetry*.[9]

2.5 Mathematical methods

The path from experimental raw data to generated fits, such as the DRT fits presented in this thesis, involves mathematical tools that are briefly introduced in this chapter.

2.5.1 Non-negative least squares minimization

Fitting the parameters of a model to experimentally derived data can be considered as a minimization problem of the residual of the model and experimental values. For simplicity, an exemplary data set and the corresponding fit is depicted in ***Figure 14***. The dotted red lines represent the residual $r_i = y_i - f(x_i)$, which varies for each data point y_i and corresponding model function values $f(x_i)$.

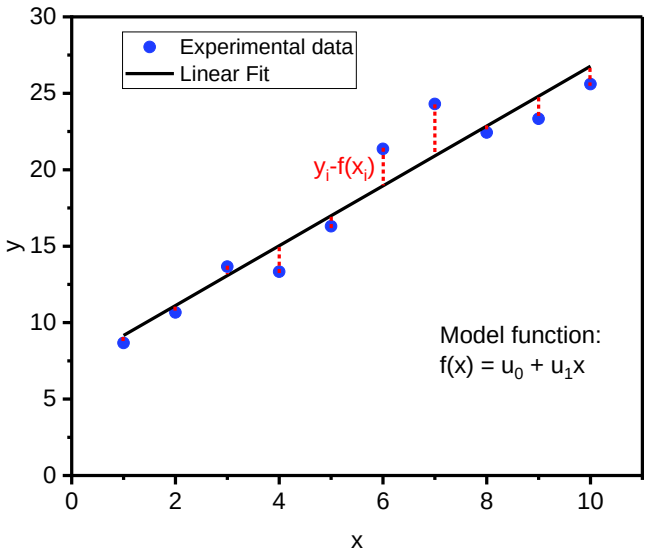

Figure 14: *Exemplary fit of a data set with a linear model function. The dotted red lines indicate the residual of the model values to the measured values. The parameters u_0 and u_1 are fit parameters to be determined.*

Typically, the residuals are squared to achieve positive values and summed up to obtain an estimate of the overall goodness of the fit. Therefore, the sum of squared residuals S_r for n datapoints can be expressed as

$$S_r = \sum_{i=1}^{n} r_i^2 = \sum_{i=1}^{n} \big(y_i - f(x_i)\big)^2. \qquad (27)$$

Utilizing linear algebra, Eq. (27) can be rewritten in terms of matrices and vectors, which may be more practical when handling large data sets. Let $\vec{u} = (u_0, u_1, \dots, u_m)$ be a vector that contains all fit parameters to be determined (for example, the slope and y-axis intercept of the linear fit in ***Figure 14***) and let $\vec{b} = (y_1, y_2, \dots, y_n)$ be a vector that contains all experimental data points. Then, Eq. (27) can be written as

$$S_r = \left|\left|\boldsymbol{A}\,\vec{u} - \vec{b}\right|\right|^2, \tag{28}$$

where $\boldsymbol{A}$ is a matrix that contains all information about the model function $f(x)$ and $\left|\left|\ \right|\right|$ denotes the Euclidean norm. For the simple case of a linear model function $f(x) = u_0 + u_1 x$, the matrix $\boldsymbol{A}$ is given in Equation (29):

$$\boldsymbol{A} = \begin{pmatrix} 1 & x_1 \\ 1 & x_2 \\ \vdots & \vdots \\ 1 & x_n \end{pmatrix} \tag{29}$$

To show that this is indeed a correct expression for the matrix $\boldsymbol{A}$, Eq. (28) is explicitly rewritten in the following Eq. (30):

$$\begin{aligned} \boldsymbol{S_r} &= \left\| \begin{pmatrix} 1 & x_1 \\ 1 & x_2 \\ \vdots & \vdots \\ 1 & x_n \end{pmatrix} \begin{pmatrix} u_0 \\ u_1 \end{pmatrix} - \begin{pmatrix} y_1 \\ y_2 \\ \vdots \\ y_n \end{pmatrix} \right\|^2 = \left\| \begin{pmatrix} u_0 + u_1 x_1 - y_1 \\ u_0 + u_1 x_1 - y_2 \\ \vdots \\ u_0 + u_1 x_n - y_n \end{pmatrix} \right\|^2 \\ &= \left(\sqrt{\sum_{i=1}^{n} (f(x_i) - y_i)^2} \right)^2 = \sum_{i=1}^{n} (f(x_i) - y_i)^2 \end{aligned} \tag{30}$$

Considering that the best fit is the one with the lowest sum of squared residuals, S_r must be minimized to achieve the optimal fit parameters. In some cases, the minimization yields unstable results, such that regularization is required.

2.5.2 Tikhonov regularization

In case of DRT, the impedance of an infinite series of RC elements is expressed in Eq. (31).

$$Z(\omega) = \int_0^\infty \frac{h(\tau)}{1 + i\omega\tau} \mathrm{d}\tau \tag{31}$$

The integral in Eq. (31) is a Fredholm integral of first kind and can be classified as mathematically ill-posed.[48] A mathematical problem is considered ill-posed, if at least one of the following criteria are not fulfilled: 1) There exists a solution to the problem, 2) the solution is unique, 3) the solution changes continuously with the initial conditions.[49] In the case of Eq. (31), the solution is not necessarily continuous but may vary strongly even at small variations of the initial conditions, and is therefore ill-posed. The required regularization can be achieved by Tikhonov regularization, one of the most common regularization methods.[50] This is realized by adding a regularization term to the cost function of the minimization problem, which scales with the factor λ. This factor can be interpreted as smoothness factor that penalizes solutions for neighboring time constants that largely deviate from each other. The cost function in Eq. (28) is thus expanded, as demonstrated in Eq. (32).[51]

$$S_r = \left|\left|\boldsymbol{A}\,\vec{u} - \vec{b}\right|\right|^2 + \left|\left|\lambda \boldsymbol{I}\vec{u}\right|\right|^2 \qquad (32)$$

3. Experimental details

The details of experiments and analysis techniques that were conducted during the doctoral period are laid out in this chapter, divided into four subtopics. In subtopic 1, the algorithm for the distribution of relaxation times is presented, alongside relevant experimental parameters for the impedance measurements. In subtopic 2, the collaborative works on *in situ* observation of Li deposits are highlighted, providing details on cycling protocols and NMR spectroscopic experiments. In subtopic 3, the details of the cyclovoltammetry experiments are laid out and in subtopic 4, the basics for the calculation of energy density and specific energy are presented.

3.1 Distribution of relaxation times analysis

The distribution of relaxation times analysis was performed with a custom-made program after acquiring impedance data for various electrochemical systems. Therefore, details of the DRT algorithm and the preceding EIS measurements are given below.

3.1.1 DRT algorithm

The minimization algorithm was developed in Wolfram Mathematica at first and finalized in Python language due to enhanced calculation time and simpler distribution of the program among the institute. At its core, the algorithm is based on a non-negative least square minimization that fits a series of RC-elements to the experimental data (real part and imaginary part). An overview of the working principle is presented in ***Figure 15***. As input parameters, the measured real and imaginary parts at a given frequency are required, as well as a regularization parameter λ. The latter is required to regulate the impact of noise on the fit result. In principle, λ is a measure of the similarity between two neighboring fitting points (see also Chapter 2.5.2). Furthermore, the number of predefined time constants (multiples of the number of experimental frequencies) can be chosen to increase the resolution of the DRT spectra (at the cost of calculation time). As a first step, the range of time constants is created. Then, the modeling matrix ***A*** and the data vector ***b*** are created, that incorporate the underlying model (series of RC elements and serial elements R, C, and L) and the measured real and imaginary parts of the impedance, respectively. In the next step, the normalized cost function ***J*** is minimized and a solution vector ***x*** is obtained. The output comprises not only the range of time constants and the solution vector, but also the residuals, as well as the residual norm and the solution norm for quality control.

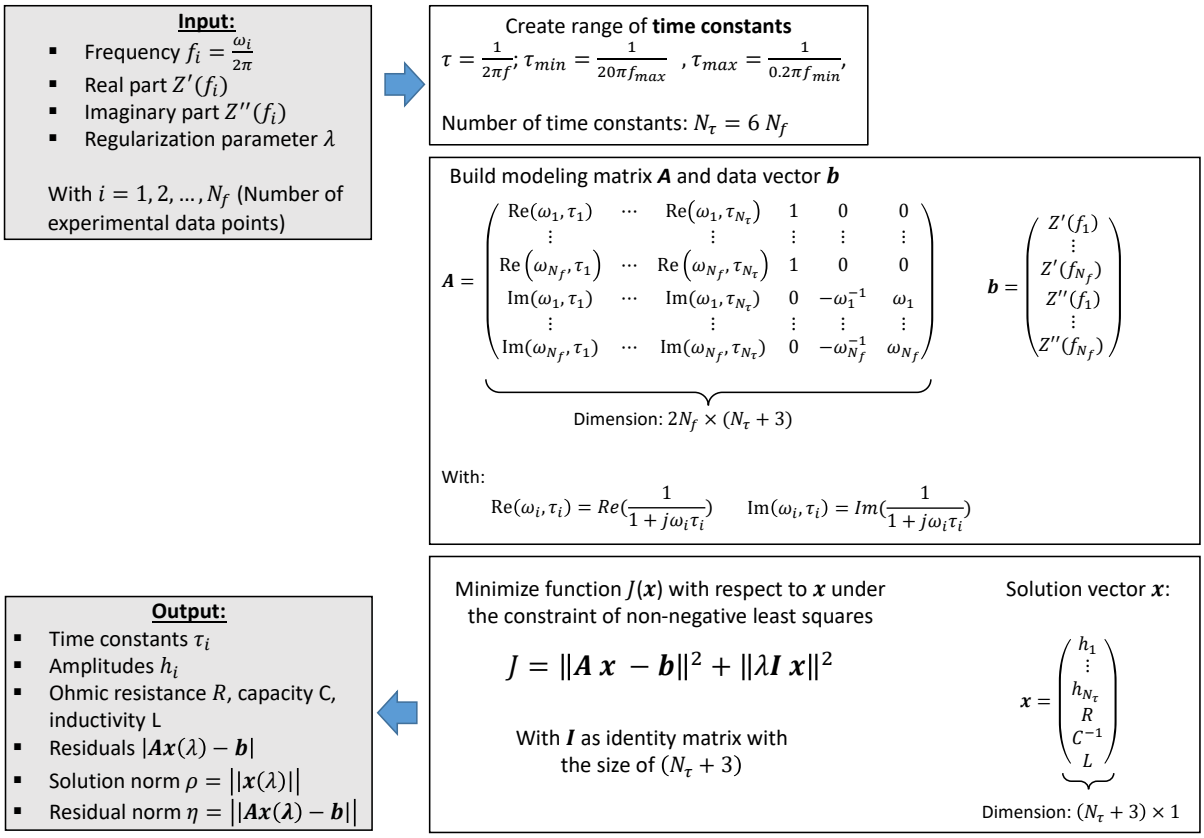

***Figure 15**: Outline of the DRT algorithm for calculating the resistive-capacitive contribution of each RC-element, as well as the Ohmic resistance R, capacity C and inductivity L.*

A code excerpt is shown in ***Figure 16*** that demonstrates the core of the minimization algorithm. After initializing the input data (frequency, real part and imaginary part of the resistance), the set of time constants is created with the function `rtimesfct()` and takes into account an integer factor (e.g., 2x or 3x the number of frequencies), as well as the boundaries (e.g., 1 or 2 more decades than the frequency window). The function `buildmat()` creates the modeling matrix ***A*** and merges it with the regularization matrix (identity matrix with λ on the diagonal entries). Furthermore, the function considers that the user can decide to include serial elements (R, C, L) within the model. Following the scheme in ***Figure 15***, the function `buildbvec()` generates the vector of the acquired data (real and imaginary part of the impedance). Finally, the function `nnlsfunc()` yields the non-negative least squares following a Python implementation of the minimization algorithm published by Lawson and Hanson.[52]

```
class DRTsolver:
    def __init__(self, data):
        self.data = data # initialize original freq, reals, negims
        self.freqi = [col[freqcol] for col in self.data]
        # initialize adjusted freq, negim and reals
        self.freq = self.freqi[self.hboundary:self.lboundary]
        self.negim = self.negimi[self.hboundary:self.lboundary]
        self.reals = self.realsi[self.hboundary:self.lboundary]
    ...

    def rtimesfct(self): # define time constants
        self.get_boundaryfactor()
        lowerboundary = (1/self.boundaryfactor)*1 / (2 * math.pi * self.freq[0])
        upperboundary = self.boundaryfactor*1 / (2 * math.pi * self.freq[-1])
        self.get_rfact()
        rtimes = np.geomspace(lowerboundary, upperboundary, num=self.rfact * len(self.freq)).tolist()
        return rtimes

    def buildmat(self):
        rtimes = self.rtimesfct()
        realpartlist = [[(1 / (1 + 2j * math.pi * i * j)).real for j in rtimes] for i in self.freq]
        imagpartlist = [[(1 / (1 + 2j * math.pi * i * j)).imag for j in rtimes] for i in self.freq]
        matA = np.vstack([realpartlist, imagpartlist]).tolist()
        vartp = [var_r.get(), var_c.get(), var_l.get()]
        regmat1 = [[x * self.lambada for x in y] for y in np.identity(len(list(rtimes))).tolist()]
        if vartp == [1, 1, 1]:
            r_array = [[1, 0, 0] for i in self.freq]
            c_array = [[0, -1 / (2 * math.pi * i), 2 * math.pi * i] for i in self.freq]
            rc_array = np.vstack([r_array, c_array]).tolist()
            matC = np.hstack([matA, rc_array]).tolist()
            regmat2 = [[0, 0, 0] for i in rtimes]
        elif vartp == [1, 0, 0]:
            r_array = [[1] for i in self.freq]
            c_array = [[0] for i in self.freq]
            rc_array = np.vstack([r_array, c_array]).tolist()
            matC = np.hstack([matA, rc_array]).tolist()
            regmat2 = [[0] for i in rtimes]
        elif vartp == [1, 1, 0]:
            ...
        elif vartp == [0, 1, 0]:
            ...
        elif vartp == [0, 0, 1]:
            ...
        elif vartp == [1, 0, 1]:
            ...
        elif vartp == [0, 1, 1]:
            ...
        else:
            ...
        regmat3 = np.hstack([regmat1, regmat2]).tolist()
        matCreg = np.vstack([matC, regmat3])
        return matCreg

    def buildbvec(self):
        rtimes = self.rtimesfct()
        bvec = np.hstack([self.reals, self.negim]).tolist()
        regvec0 = [0 for i in rtimes]
        bvecreg = np.hstack([bvec, regvec0])
        return bvecreg

    def nnlsfunc(self):
        mat = self.buildmat()
        vec = self.buildbvec()
        result = nnls(mat, vec)[0].tolist()
        return result
```

Figure 16: *Code excerpt of the* `DRTsolver` *class used to calculate the non-negative least squares of the input data compared to the model.*

The graphical user interface was constructed with the *tkinter* module. The complete code and the standalone executable program can be downloaded free of charge from github.com (https://github.com/pelenn22/DRTtool).

3.1.2 Experimental details of the impedance measurements

Electrochemical impedance spectroscopy was performed in potentiostatic mode within a frequency window of 5 MHz to 0.1 Hz at an amplitude of 10 mV (if not stated otherwise). The acquired raw data of the EIS measurements was adjusted to the region of interest (e.g., 1 MHz to 1 Hz) and DRT was performed with the custom-made DRT software using 6 times the number of frequencies as length for the time constant array, as well as an extrapolation of ± 1 decade to avoid boundary effects. If not stated otherwise, a regularization parameter of $\lambda = 0.2$ was used as a compromise between oversmoothening and occurrence of unphysical peaks. All experiments were performed in a controlled climate chamber (the temperature is indicated for the individual experiments).

3.2 Non-destructive monitoring of Li microstructures

In this section, the experimental details of two collaborative works are presented. In the first collaboration, cell failure modes in Li||Li cells with a single-ion conducting polymer electrolyte were explored by X-ray microtomography, impedance spectroscopy and distribution of relaxation times analysis. In the second collaboration, Li metal electrodes were modified with Si-based polymer coatings and the deposition/dissolution was monitored with ^{7}Li NMR spectroscopy.

3.2.1 Li microstructures and cell failure

All electrochemical and X-ray tomographic experiments were performed at the Lawrence Berkeley National Laboratory (LBNL), in particular by Louise Frenck and Dilworth Y. Parkinson of the group of Prof. Nitash Balsara. Since the first experiments were already performed at the end of 2020, Covid-19-related travel restrictions did not allow for personal exchange. Materials preparation and data evaluation (incl. DRT analysis) was performed in Münster. The experimental details described in this chapter were also published in ref.[53]

Materials preparation and cell assembly

The single-ion conducting polymer electrolyte was prepared in Münster based on established protocols.[43] The polymer electrolyte is composed of lithiated polysulfonamide (PSA, ***Figure 17a***) that is blended with poly(vinylidene fluoride-co-hexafluoropropylene) (PVDF-HFP) in a weight ratio of 1:3 (PVDF-HFP : PSA). The two polymers were blended by dissolving 100 mg of PVDF-HFP in 4 mL of anhydrous n-methyl-2-pyrrolidone (NMP) and subsequently adding 300 mg of PSA and stirring overnight at 60 °C. To obtain a solid membrane, the solution was poured in an evaporation dish and vacuum dried at 80 °C for 24 h. The resulting membranes were fragile and therefore swollen in a mixture of ethylene carbonate (EC) and propylene carbonate (PC) (volume ratio 1:1). Swelling with these solvents did not only make the

membrane mechanically flexible (***Figure 17b***), but also greatly enhanced its ionic conductivity to a comparably high value of 0.5 mS cm^{-1} at 20 °C, as disclosed in previous work.[43,54] The solvent uptake of the polymer membrane amounts to approximately 130 wt%, which reflects a natural limit of this blend membrane.[43] Membrane preparation was performed in a dry room environment (with < 20 ppm H_2O), whereas cell manufacturing and characterization was done at Berkeley in an argon-filled glove box. After re-soaking the membranes with EC/PC solution to account for potential losses during sample shipment, they were cut into round discs (11.4 mm in diameter) for cell assembly. For the electrodes, three Li metal foils (Honjo Metal, 250 µm) were stacked and pressed onto Ni current collectors at 130 MPa to obtain a smooth and shiny Li surface. Discs with a diameter of 9.5 mm were punched out and an electrolyte membrane was placed between two of these electrodes. The cell stack was sandwiched between two stainless steel shims (250 µm thick) for better horizontal alignment and stability and sealed in an air-tight pouch foil (***Figure 17c***).

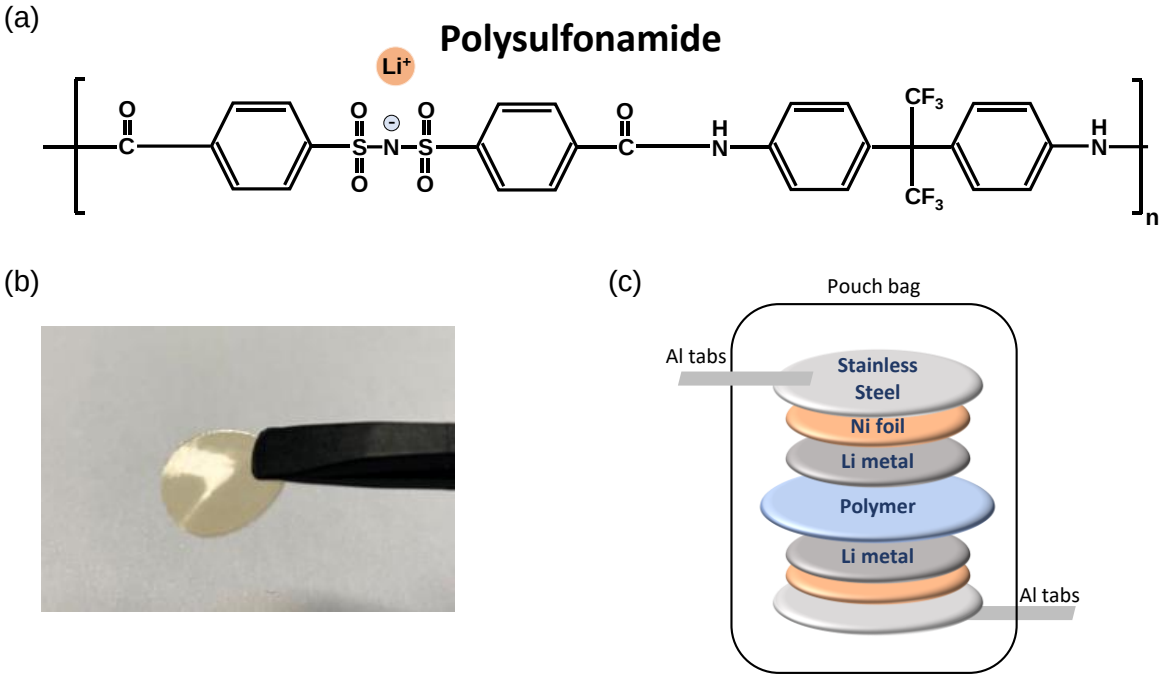

Figure 17: *(a) Schematic structure of the synthesized polysulfonamide (PSA) anion and the associated Li cation. (b) Picture of the obtained flexible membrane. (c) Cell stack with individual layers of the investigated cells. Adapted with permission from ref.[53] Copyright 2024 © American Chemical Society.*

Electrochemical experiments

The electrochemical experiments were conducted at the Lawrence Berkeley National Laboratory by Louse Frenck. The cells were cycled at 25 °C inside an environmental chamber using a BioLogic VMP3 potentiostat. After resting for 6 h, the cells were conditioned at a low current density of 0.02 mA cm^{-2} for 10 cycles before applying current densities of 0.1 mA cm^{-2} and 0.3 mA cm^{-2}. Each half-cycle consists of 4 h of polarization in one direction (either positive

or negative current), followed by 45 min of rest to reach a steady state for impedance spectroscopy measurements. The estimated mass of Li transported back and forth is ca. 0.1 mg cm^{-2} or 2 µm per half-cycle at a current density of 0.1 mA cm^{-2} and 0.3 mg cm^{-2} or 6 µm at a current density of 0.3 mA cm^{-2}, respectively. Impedance spectra were acquired at the same device (BioLogic VMP3) with a frequency range from 1 MHz to 0.1 Hz at an amplitude of 40 mV. The comparably high amplitude (an amplitude of 10 mV is common for EIS) was applied to enhance the signal-to-noise ratio. Kramers-Kronig conformity was checked to ensure that the acquired data was valid and data points below 1 Hz and above 14 kHz were excluded from further analysis. The data for the interphase resistance was multiplied with the electrode area and divided by two, to account for the two symmetric electrodes.

X-ray microtomography

All X-ray microtomographic experiments and data processing were conducted by researchers at the Lawrence Berkeley National Laboratory (LBNL), in particular by Louise Frenck and Dilworth Y. Parkinson. Monochromatic hard X-rays (22 keV) were used at beamline 8.3.2 at the Advanced Light Source to illuminate the cells. The X-ray shadow casted by the sample was converted into visible light using a scintillator and, after magnification with an optical microscope, the image was converted into a digital image file (***Figure 18***). The cell was rotated slightly and repeatedly imaged until 1313 images were collected (total rotation angle of 180°). 3D reconstruction images were produced by the software Xi-Cam[55], cross-sections of the cells were stacked and rendered using the software ImageJ. The cells were imaged in their original pouch format at a magnification of 2:1 and 4:1, corresponding to pixel sizes of 3.4 µm and 1.7 µm, respectively.

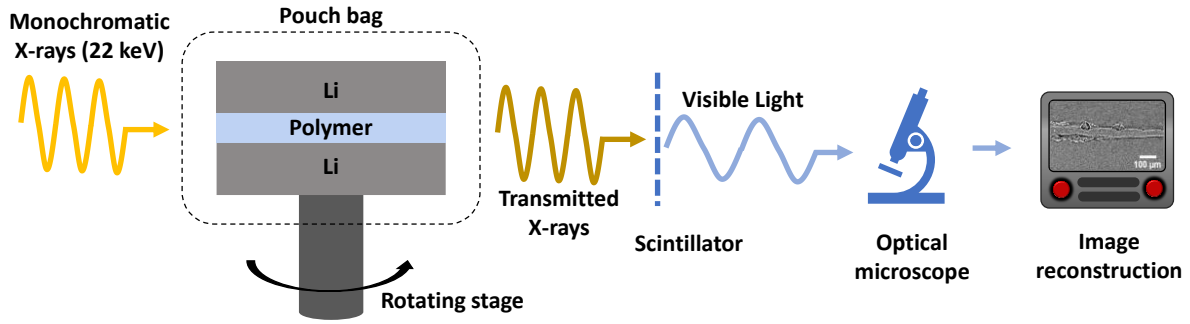

***Figure 18**: Scheme of the experimental set-up to acquire X-ray microtomographic images of an electrochemical cell. Adapted with permission from ref.[53] Copyright 2024 © American Chemical Society.*

3.2.2 Selective desolvation coatings on Li metal

The functionalized silica polymer coatings were synthesized at the Pennsylvania State University (PSU) in the group of Prof. Donghai Wang, following a previously published

synthesis route.[56] The coating dispersions were prepared by Guoxing Li (PSU) based on the following recipes. For the polyethylene oxide-based silica polymers (PEOS), 40 mg of polyethylene oxide ($M_v = 10^6\ \mathrm{g\,mol^{-1}}$) were dissolved in 4 mL of N-methylpyrrolidone (NMP) and 100 mg of (3-isocyanatopropyl) functionalized silica, as well as 2 mg of dibutyltindilaurate (DBTDL) were added. The reaction system was stirred at room temperature for 8 hours to achieve a viscous dispersion. For the crown-ether-based silica polymers (CES), 38 mg of 2-hydroxymethyl-12-crown-4 were dissolved in 2 mL of NMP and 100 mg of (3-isocyanatopropyl) functionalized silica, as well as 2 mg of DBTDL were added. The reaction system was stirred at room temperature for 8 hours, then 10 mg of polyethylene oxide ($M_v = 10^6\ \mathrm{g\,mol^{-1}}$) were added and the mixture was again stirred for 10 min to achieve a homogenous dispersion.

Coating procedure

The coating dispersions were shipped to Münster and transferred to an argon-filled glovebox ($\mathrm{O_2} < 0.1\ \mathrm{ppm}, \mathrm{H_2O} < 0.1\ \mathrm{ppm}$). Prior to coating, the dispersions were stirred at 40 °C for 2 h to achieve a homogeneous solution. Li metal foil (Honjo, 300 µm) was placed onto a glass plate in the glovebox and flattened with a mylar foil. The Li metal was wetted with diethyl carbonate (DEC) to prevent sticking to the mylar foil or the glass plate. After fixing the Li metal foil to the glass plate with adhesive tape, a doctor blade (50 µm gap height between Li and blade) was used to coat the Li metal. Coating was done manually with an approximate velocity of 2 cm s^{-1} due to the lack of space in the glovebox for an automatic film applicator.

^{7}Li NMR spectroscopy

Li||Li pouch-type cells (***Figure 19***) were analyzed in a broadband probe (^{1}H,^{19}F// (X = ^{6}Li–^{7}Li) using a Bruker Avance III 200 MHz spectrometer (4.7 T). The Li electrodes had a thickness of 300 µm and an area of 1.25 cm² (0.5 x 2.5 cm²). The cells were polarized with a current density of 1 mA cm^{-2} for 4 h at a temperature of 20 °C. The resonance frequency of the spectrometer was set to 77.8 MHz at a pulse length of 16 µs (=15625 Hz) and a power of 80 W, following a series of previous saturation pulses. Calibration was carried out with a 1 M LiCl + 0.1 g L^{-1} $CuSO_4$ standard aqueous solution. A recycle delay of 1 s was optimized for the peak assigned to bulk Li metal at 246 ppm. The ^{7}Li NMR peaks of the electrolyte and SEI compounds were in the range of -20 ppm to 20 ppm and therefore not considered in the optimization range. Bruker Topspin software and a custom-made MATLAB script (developed by Lennart Wichmann[57,58]) were used for data processing and peak analysis, respectively. The experimental procedures were carried out based on previously established protocols.[59,60]

(a)

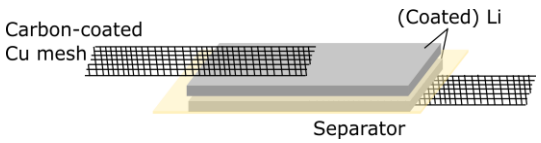

(b)

Figure 19: *(a) Schematic drawing of the NMR pouch-type cell and (b) picture of the NMR cell holder with implemented NMR coil and brass contacts for battery operation.*

3.3 Li|polymer interface kinetics

The interface kinetics of Li metal in contact with polymer electrolyte were studied with fast cyclovoltammetry using custom-made microelectrodes. Therefore, the experimental details of the fabrication of the microelectrodes and the cyclovoltammetry experiments are given in the following two subchapters.

3.3.1 Fabrication of microelectrodes

The microelectrodes were designed to fit into a standard metal housing for three-electrode Swagelok-type cells. Polyether ether ketone (PEEK) was chosen as base material for the cylinder due to its excellent chemical inertness and temperature stability. A first version of the hollow cylinders was 3D-printed with an Appium P220 device, before switching to more precise fabricates created through milling and drilling by the workshop for fine mechanics of the University of Münster (***Figure 20a***). The tungsten wire (Alfa Aesar, 25 µm in diameter) was not straight enough to directly thread it through the hollow cylinder. Therefore, it was first wound onto copper wire with a diameter of 0.5 mm and then threaded through a glass capillary with an inner diameter of 0.8 mm and an outer diameter of 1.0 mm and a length of 2 cm. Electrical contact between the Cu wire and the tungsten wire was maintained by silver conductive paste. The glass capillary with the incorporated copper/tungsten wires was then threaded through the hollow PEEK cylinder (***Figure 20b***). The cylinder was fixed on a rack so that the tungsten wire was straightened, before a mixture of epoxy resin and epoxy hardener was filled into the hole to cover the tungsten wire (***Figure A1*** in the Appendix). After a curing time of 24 h, the electrode surface was flattened with abrasive paper and finally polished with Al_2O_3 polishing paste (particle size 0.3 µm) to achieve a smooth and flat electrode surface. A photo of the finished microelectrode is shown in ***Figure 20c***.

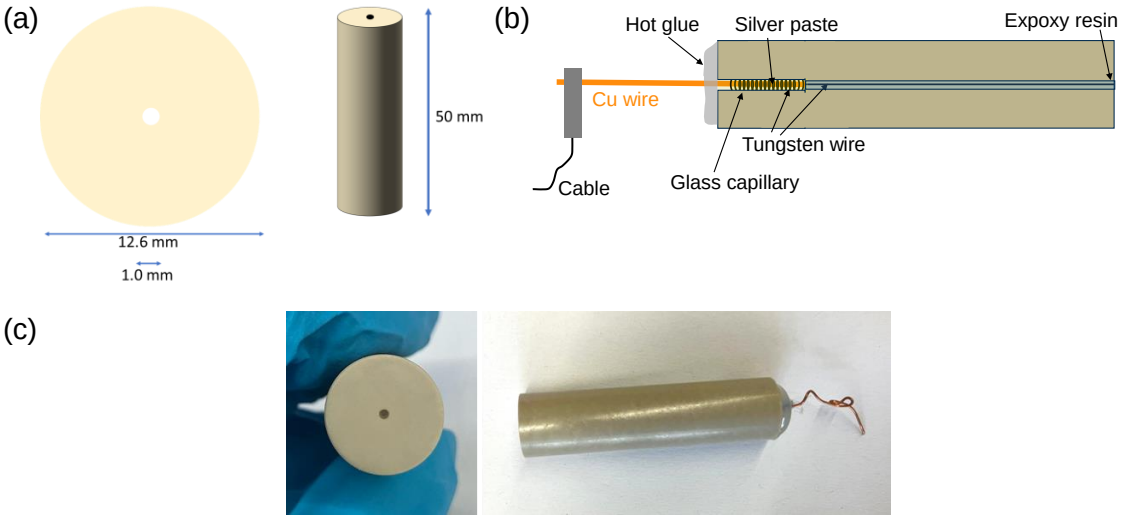

Figure 20: *(a)Top and side view of the PEEK cyclinder with a feed-through for the thin wire electrode. (b) Cross-section and (c) photographs of an exemplary microelectrode.*

The microelectrode was implemented as working electrode in a Swagelok-type cell, as shown in ***Figure 21***. Li metal foil (Honjo, 50 µm) was used as counter electrode. The reference electrode was not used for cells with polymer electrolytes.

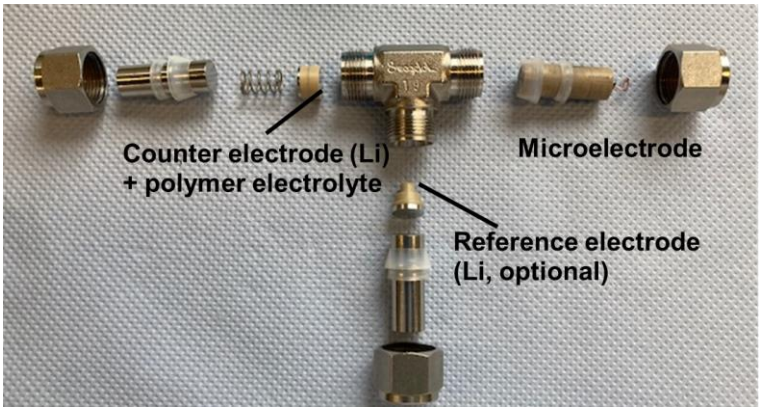

Figure 21: *Photograph of the Swagelok-type cell incorporating the PEEK cylinder with the implemented copper wire that is surounded by the 25 µm thick tungsten wire.*

3.3.2 Cyclovoltammetry

Cyclovoltammetry was performed on a Zahner ZenniumPro potentiostat with various settings, including scan rates from 100 µV s^{-1} to 100 V s^{-1} and voltage windows from -1.5 V to 2.5 V. Since the reference electrode was not used in this set-up, the acquired data is not to be understood as “true” potential, but rather as voltage (i.e., potential difference).

3.4 Projection of energy density

Specific energy and energy density of projected multi-layered cells are calculated based on simple geometric and electrochemical calculations. A straightforward graphical user interface

was created with Python to allow for custom cell modifications. In the following chapters, the calculation details and an excerpt of the Python program are presented.

3.4.1 Calculation of energy density and specific energy

The projection of specific energy (Wh kg^{-1}) and energy density (Wh L^{-1}) is based on geometric and electrochemical considerations. Both mass and volume of single layers can be straightforwardly acquired experimentally and projected to multi-layered batteries by adding up individual cell layer thicknesses and masses. A calculation of the storable energy (in Wh) is less straightforward and requires further considerations. Since the energy density should be a measure of how much energy can be stored reversibly, the average discharge capacity is considered rather than the average charge capacity. Instead of the absolute capacity, the specific capacity Q_S is often presented in literature and is hence used as an input parameter for the calculation. Also, the average operating voltage is approximated as the plateau value of the observed voltage curve (nominal voltage $V_{nominal}$). To derive the actual amount of the available energy, the active mass m_{act} (used to calculate the specific discharge capacity) is another factor in the calculation, since the available energy is the product of active mass, nominal voltage and specific discharge capacity (***Figure 22***).

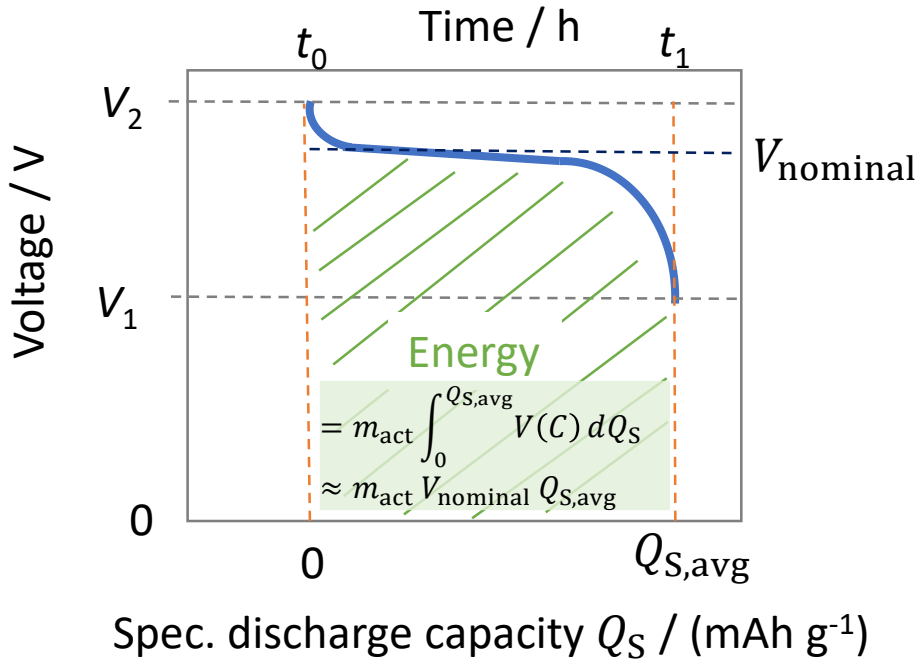

Figure 22: *Voltage profile of a battery during discharge at a constant current density. The available energy (in Wh) depends on the active mass m_{act} (in g), the nominal voltage $V_{nominal}$ (in V), and the specific discharge capacity Q_S (in $mAh\ g^{-1}$).*

In multi-layered pouch cells, each cathode|electrolyte|anode layer (denoted as n) contributes a portion E_{n} to the overall energy $E_{\mathrm{tot.}}$ (Eq. (33)) The total mass of the cell, $m_{\mathrm{tot.}}$, is the product of the number of layers and of the mass of an individual layer, m_l, plus the mass of the casing (m_{casing})(Eq. (34)). The total volume is calculated analogously to the total mass (Eq. (35)). The energy density and the specific energy are then calculated by dividing the total energy by the total volume and total mass, respectively (Eq. (36) and (37)).

$$E_{\mathrm{tot.}} = n\,E_l \tag{33}$$

$$m_{\mathrm{tot.}} = n\,m_l + m_{\mathrm{casing}} \tag{34}$$

$$V_{\mathrm{tot.}} = n\,V_l + V_{\mathrm{casing}} \tag{35}$$

$$e_m = \frac{E_{\mathrm{tot.}}}{m_{\mathrm{tot.}}} = \frac{n\,E_l}{n\,m_l + m_{\mathrm{casing}}} \approx \frac{E_l}{m_l}\ (\text{for } n\,m_l \gg m_{\mathrm{casing}}) \tag{36}$$

$$e_V = \frac{E_{\mathrm{tot.}}}{V_{\mathrm{tot.}}} = \frac{n\,E_l}{n\,V_l + V_{\mathrm{casing}}} \approx \frac{E_l}{V_l}\ (\text{for } n\,V_l \gg V_{\mathrm{casing}}) \tag{37}$$

For large n, the terms associated with the cumulative active layer mass and volume are much larger than the terms for the casing ($n\,m_l \gg m_{\mathrm{casing}}$ and $n\,V_l \gg V_{\mathrm{casing}}$, respectively), and the expressions for $m_{\mathrm{tot.}}$ and $V_{\mathrm{tot.}}$ become proportional to n. As the absolute energy $E_{\mathrm{tot.}}$ represents the sum of the energy of an individual layer E_l (and thus proportional to n), the energy density e_V and specific energy e_m are independent of n in these limits. Note that the simple addition of individual layers becomes more complicated if active materials are used that were coated onto the same current collector foil (coated from both sides). Then, only half of each current collector foil contributes to each layer. The adjusted equations were used in the program and are given in Eq. (38) and Eq. (39). For simplicity, the thickness $d_{\mathrm{tot.}}$ is shown rather than the volume. The symbols $d_{\mathrm{c|e|a}}$ and $m_{\mathrm{c|e|a}}$ refer to the thickness of and mass of an individual cathode|electrolyte|anode layer without current collector, respectively. The symbols $d_{\mathrm{cc,a}}$, $d_{\mathrm{cc,c}}$, $m_{\mathrm{cc,a}}$, and $m_{\mathrm{cc,c}}$ refer to the thickness and mass of the anodic and cathodic current collectors, respectively. The thickness and mass of the casing refers to that of a single layer (either top or bottom), thus it is multiplied by 2.

$$d_{\mathrm{tot.}} = n\,d_{\mathrm{c|e|a}} + \frac{n+1}{2}\left(d_{\mathrm{cc,a}} + d_{\mathrm{cc,c}}\right) + 2\,d_{\mathrm{casing}} \tag{38}$$

$$m_{\mathrm{tot.}} = n\,m_{\mathrm{c|e|a}} + \frac{n+1}{2}\left(m_{\mathrm{cc,a}} + m_{\mathrm{cc,c}}\right) + 2\,m_{\mathrm{casing}} \tag{39}$$

Note that these calculations are only exact for odd values of n. For an even number of layers, there is one cathode current collector more than anode current collector, or vice versa. The term $\frac{n+1}{2}\left(d_{\mathrm{cc,a}} + d_{\mathrm{cc,c}}\right)$, however, does not differentiate between cathode current collector and

anode current collector in this regard, and therefore can be understood as an average of the two. The impact of this inaccuracy on the results reduces drastically for $n \gg 1$.

3.4.2 Code implementation

The calculation was performed within a Python script and the graphical user interface was generated using the *customtkinter* package. The code for the core function `calculation()` is visualized in a shortened form in ***Figure 23***. At first, the input values (slider values) from the user are gathered to define local variables that fully describe the system of interest. Then, key properties of the projected cell, such as thickness, mass, and energy content are straightforwardly calculated, along with the specific energy and energy density.

```
def calculation():
    voltage = round(slider_a.get(),slider_a.rounder)
    specific_capacity = round(slider_b.get(),slider_b.rounder)
    ...

    # Total thickness, unit: mm
    totalthickness = 0.001*(layers*(electrolyte_thickness + anode_thickness + cathode_thickness) + ((layers+1)/2)*
(anode_cc_thickness + cathode_cc_thickness) + 2*casing_thickness)

    # Total volume, unit: cm³
    totalvolume = 0.1*totalthickness*active_area*casing_oversizing

    # Total weight, unit: g
    totalweight = 0.0001*(layers*(10*active_area*active_massloading/(0.01*active_material_ctd) +
anode_density*anode_thickness*active_area*anode_oversizing +
electrolyte_density*electrolyte_thickness*active_area*separator_oversizing)
                  + ((layers+1)/2)*(anode_cc_density*anode_cc_thickness*active_area*anode_oversizing +
cathode_cc_density*cathode_cc_thickness*active_area)
                  + 2*casing_density*casing_thickness*casing_oversizing*active_area)

    # Total energy, unit: Wh
    totalenergy = 0.000001*specific_capacity*active_massloading*voltage*active_area*layers

    # Absolute capacity, unit: Ah
    absolute_capacity = 0.000001*specific_capacity*active_massloading*active_area*layers
    if absolute_capacity < 0.1:
        roundcap = round(absolute_capacity,3)
    else: roundcap = round(absolute_capacity,1)

    # Specific energy, unit: Wh/kg
    specificenergy = 1000*totalenergy/totalweight

    # Energy density, unit: Wh/L
    energydensity = totalenergy/(0.001*totalvolume)

    return int(round(specificenergy,0)), int(round(energydensity,0)), roundcap, round(totalthickness,1),
round(totalvolume,1), round(totalweight,1)
```

Figure 23: *Code excerpt of the function that calculates the specific energy and energy density based on user inputs.*

The complete code and executable file can be downloaded free of charge from github.com (https://github.com/pelenn22/EnergyDensityCalculation).

4. Results and discussion

The following four sections summarize major achievements and experimental results gathered during the doctoral research period from January 2020 to December 2023. In section 4.1, the distribution of relaxation times analysis is introduced and applied to various systems, ranging from simple electric circuits to actual batteries. In section 4.2, special focus is put on the advanced characterization of Li microstructures via electrochemical impedance spectroscopy, X-ray microtomography, and NMR spectroscopy. In section 4.3, the charge transfer kinetics (Li nucleation and dissolution) are characterized by fast cyclovoltammetry employing a custom-made microelectrode. Finally, in the last section (4.4), energy densities and specific energies of academic model cells are projected towards multi-layered pouch cells with capacities > 1 Ah to identify key bottlenecks of current cell systems.

4.1 Impedance analysis of polymer electrolyte systems

A core goal of this thesis was to establish DRT analysis for the investigation of electrochemical impedance data, thereby identifying key observables of interfaces and interphases in batteries. The alternating current or voltage signals applied during EIS elucidate features that are not detectable by dc methods, such as capacitances of charge separation layers and charge transfer rates. Here, DRT may ease quantification of these parameters and assist in the development of more sophisticated electrochemical models. Since DRT was not considered a standard method in the electrochemical community at the beginning of the doctoral thesis, only a few commercial software solutions were available, that did not allow sufficient customization or access to the source code (e.g., *RelaxIS* by *rhd instruments*). Therefore, a custom-made graphical user interface and DRT algorithm was programmed with Python. In this chapter, this DRT Tool is first tested with simulated spectra, before applying the software to data derived from real electrochemical cells and extracting key observables thereof. Parts of the results presented here were published in the following research articles:[61,62]

- Y.-H. Chen, P. Lennartz, K. L. Liu, Y.-C. Hsieh, F. Scharf, R. Guerdelli, A. Buchheit, M. Grünebaum, F. Kempe, M. Winter, G. Brunklaus: Towards all-solid-state polymer batteries: going beyond PEO with hybrid concepts, *Advanced Functional Materials*, 2300501, 2023, [https://doi.org/10.1002/adfm.202300501].
- P. Lennartz, K. Borzutzki, M. Winter, G. Brunklaus: Viscoelastic polyborosiloxanes as artificial solid electrolyte interphase on lithium metal anodes, *Electrochimica Acta*, 388, 138526, 2021, [https://doi.org/10.1016/j.electacta.2021.138526].

4.1.1 Artificial impedance spectra

Prior to applying the DRT algorithm to data acquired from electrochemical cells, its functionality is tested using artificial data generated by a simulation software (*Circuit Simulator*, *rhd-instruments*). In the simplest case, a single, uniform electrochemical interface with an ideal capacitive layer (capacitance *C*) and a defined charge transfer resistance *R* yields a semi-circle in the complex plane, as shown in ***Figure 24a***. The characteristic time constant of this simulated interface ($\tau = RC$) yields 10^{-5} s, which is also well resolved in the respective DRT plots (***Figure 24b***). As anticipated, the width of a DRT peak depends on the regularization parameter λ, since stronger regularization penalizes solutions that are less smooth (that is, their norm is large).[51] Regardless of λ, the integrated spectrum corresponds to the real part of the impedance and, in this case, amounts to $R = 50\ \Omega\,\mathrm{cm}^2$. The error margins are largest for $\lambda = 1$, resulting in a value of $50.17\ \Omega\,\mathrm{cm}^2$, i.e. 0.3 % deviation from the input value. The results suggest that in the case of noise-free impedance spectra that originate from ideal resistive-capacitive interfaces, λ should be set as small as possible without exceeding the spectral resolution (which depends on the number of pre-defined time constants). A value of $\lambda = 0.1$ seems reasonable in this case.

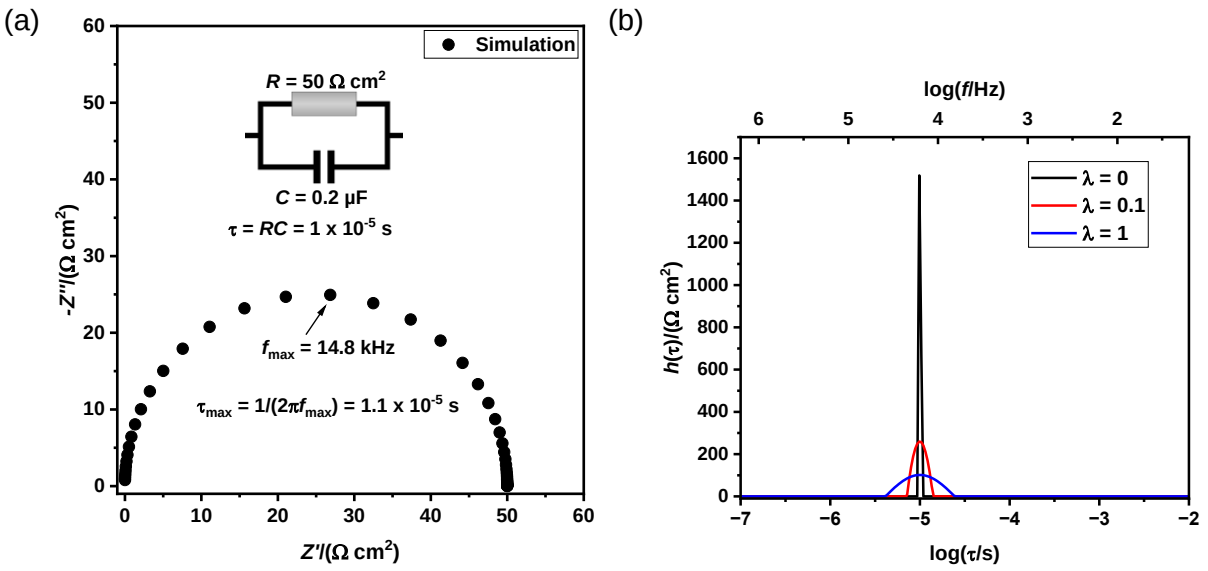

Figure 24*: (a) Nyquist plot of the simulated impedance response of a resistor in parallel with a capacitor. (b) Corresponding DRT spectra using a different regularization parameter λ.*

A CPE element is often employed to account for any inhomogeneities of real interfaces and its impedance response in parallel with a resistor is depicted in ***Figure 25a***. Here, an exponential factor of $\alpha = 0.9$ is proposed, modeling a slightly non-ideal interface. The DRT spectrum of this R-CPE circuit (***Figure 25b***) demonstrates that regularization is required to achieve meaningful spectra. At a value of $\lambda = 0$, the spectrum intensity strongly fluctuates around the center of 10^{-5} s, while the spectrum with $\lambda = 0.1$ is much smoother, though showing two satellite peaks

at roughly $\log\left(\frac{\tau_c}{\mathrm{s}}\right) \pm 0.9$. The reason for the fluctuation and satellite peaks is unclear, but likely originates from the lacking transferability of R-CPE and R-C elements (which comprises the core of the invoked DRT algorithm). Based on these results, DRT analysis may help to identify CPE-type behavior in real electrochemical systems, that would be characterized by symmetric satellite peaks at low lambda values (e.g. $\lambda = 0.1$).

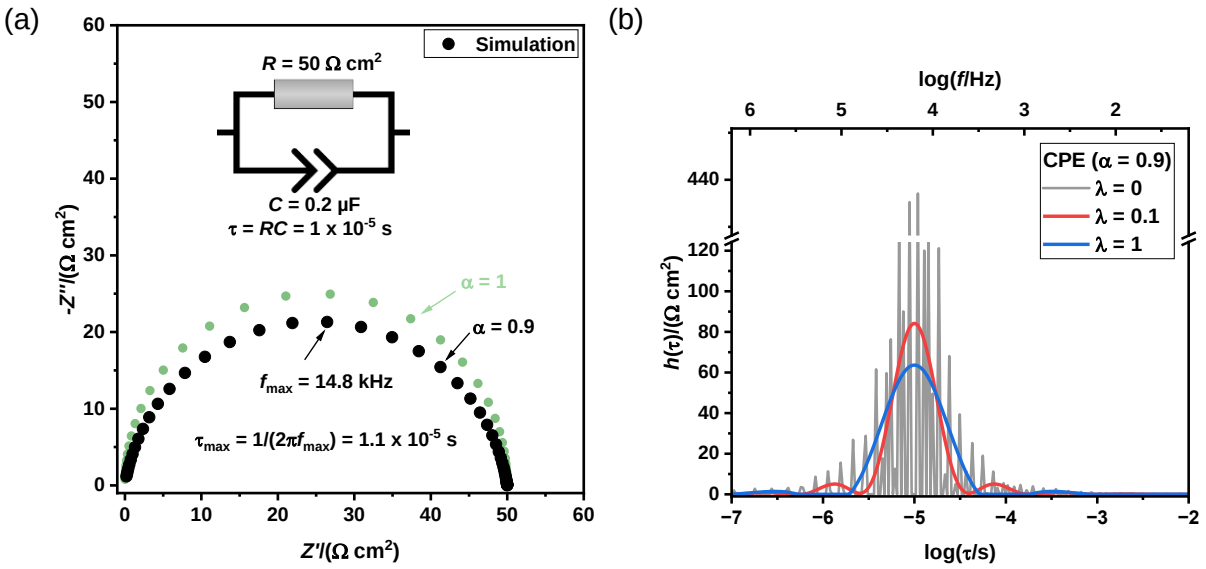

Figure 25: *(a) Nyquist plot of the simulated impedance response of a resistor in parallel with a constant phase element ($\alpha = 0.9$). The impedance spectrum of an RC element ($\alpha = 1$) is shown for comparison. (b) DRT spectra corresponding to the R-CPE circuit with varying regularization parameter λ.*

Next, instead of a CPE-type distribution, the impedance response of a series of RC-elements is considered, with slightly varying time constants centering around a single τ_c equal to the peak time constant from the previous circuits (10^{-5} s). The resistances of RC-elements follow a gaussian normal distribution on a logarithmic scale and the integrated area is defined as $R = 50\,\Omega\,\mathrm{cm}^2$, similar to the previous simulations. The impedance response of this distribution function is reconstructed using Eq. (40).[63,64]

$$Z(\omega) = \sum_i \frac{h(\tau_i)}{1 + j\omega\tau_i} \tag{40}$$

with

$$h(\tau_i) = h_0 \frac{1}{2\pi\sigma} \exp\left(-\frac{\left(\log\left(\frac{\tau_i}{\tau_c}\right)\right)^2}{2\sigma^2}\right) \tag{41}$$

The parameter h_0 is the total resistance ($50\,\Omega\,\mathrm{cm}^2$) and σ is the standard deviation ($\sigma = 0.2$). The resulting impedance response of the distribution function and the derived DRT spectra are

visualized in ***Figure 26***. The DRT algorithm fits the model function best when using a small regularization parameter of $\lambda = 0.001$. In contrast to the DRT spectra of the R-CPE elements, no satellite peaks or fluctuations are visible. Similar to previous results, the integrated area corresponds to the total resistance and is reliably quantifiable regardless of the chosen lambda value.

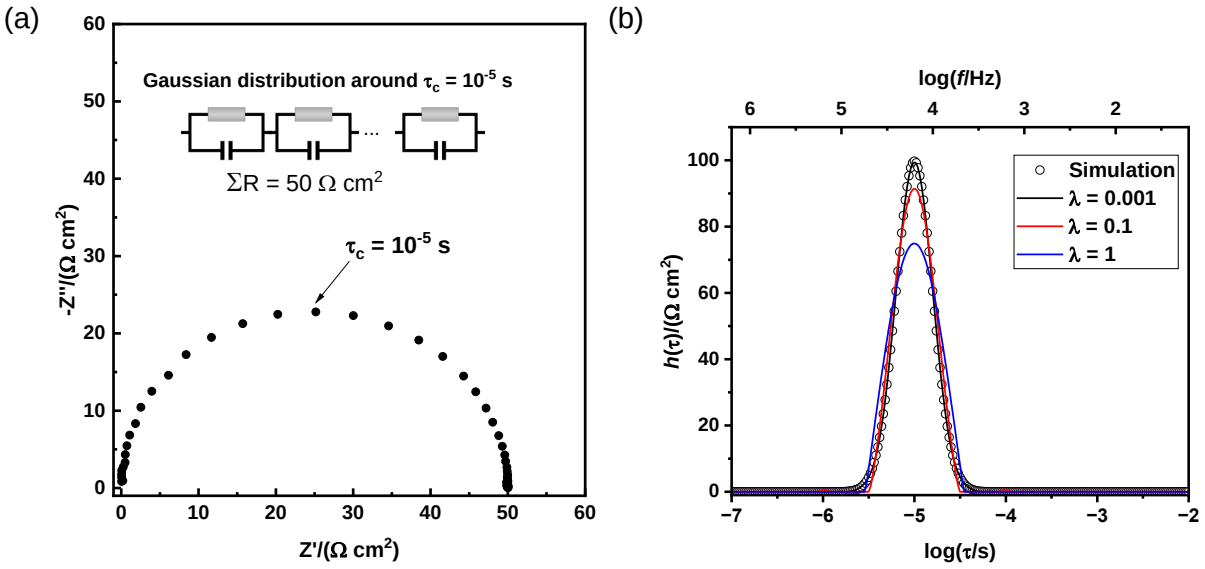

Figure 26: *(a) Nyquist plot of the simulated impedance response of a series of resistors in parallel with capacitors. (b) Corresponding DRT spectra with varying regularization parameter* λ.

Until this stage, all of the simulated data is noise-free. However, naturally occurring noise (e.g. from the presence of external electromagnetic fields) impacts the EIS data and thereby also DRT analysis.[51] By adding random noise to the real and imaginary parts of the impedance, the impact of λ is further elucidated. The distributed noise was added in Mathematica to the recreated artificial EIS spectra that were generated by a gaussian DRT distribution, where a factor (noise amplitude) was introduced to scale the noise and analyze its impact on the DRT spectra. At low regularization ($\lambda = 0.01$), artificial noise causes additional peaks and prevents identification of a main peak (***Figure 27a***). A larger noise amplitude yields larger satellite peaks that cover a wider range of time constants. Increasing the regularization substantially improves the applicability of DRT to recreate the initial spectrum, as demonstrated in ***Figure 27b***. At a value of $\lambda = 0.1$, the satellite peaks are only slightly visible for larger noise amplitudes of 0.2. Further increasing regularization to $\lambda = 0.2$ also generates fewer and less pronounced satellite peaks (***Figure 27c***). The peak amplitudes, however, deviate from the original spectrum as a consequence of regularization. The integrated area of the main peak of 49.67 $\Omega\mathrm{cm}^2$ at a noise amplitude of 0.2 and regularization of $\lambda = 0.2$ is still in an acceptable range, reflecting a deviation of 0.66 % from the expected value of 50.00 $\Omega\mathrm{cm}^2$. The peak time constant is similar to the original time constant (1.0 x 10^{-5} s). At $\lambda = 1$, regularization successfully prevents

additional satellite peaks caused by noise, but the generated curves do not fit the original spectrum well (***Figure 27d***).

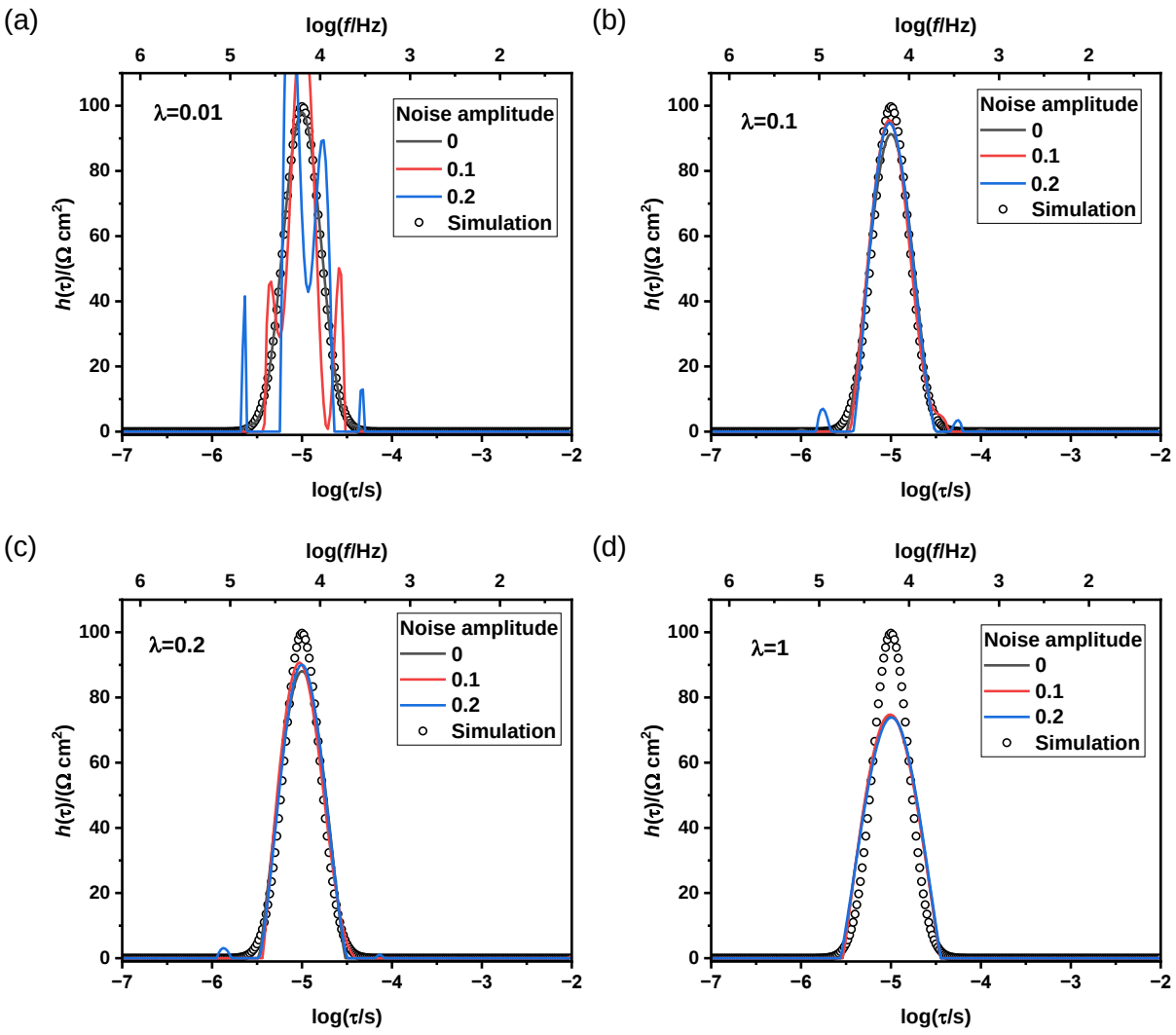

Figure 27: *DRT spectra of artificial impedance data recreated from gaussian peaks with and without noise. The noise amplitude is given as dimensionless factor and was scaled so that the resulting EIS spectra showed reasonable variations from the ideal case.*

In practice, the apparent noise level of impedance data cannot be quantified straightforwardly, but requires a detailed analysis of the error structure, as demonstrated by M. Orazem.[65] A regularization parameter between 0.1 and 0.5 was chosen for the experimental data acquired for this thesis.

4.1.2 Real electrochemical cells

After a proof-of-concept with well-defined data sets, key properties of actual electrolytes that eventually govern the electrochemical performance of a battery were obtained. This includes, for example, the ionic conductivity of the electrolyte, and the charge transfer or interphase resistances at Li|electrolyte interfaces and interphases. The ionic conductivity is a fundamental property of electrolytes that limits the achievable current passed through the bulk electrolyte in

the presence of electric fields (see Chapter 1: Fundamentals). It is typically determined at varying temperatures, as it often follows an exponential trend with temperature (e.g., Arrhenius-type conductivity). The cell set-up is highly relevant when performing EIS, as the impedance response depends, for example, on the electrode geometry and the distance between the electrodes. A straightforward cell set-up for determining the ionic conductivity comprises a symmetric cell with blocking electrodes (e.g., stainless steel), where ideally no charge transfer or electrode reactions. When increasing the complexity of the system by introducing non-blocking electrodes, in this case Li metal foil, the total impedance of the cell is then composed of the contributions from bulk electrolytes and that of the reactive interphase(s). Note that each reaction is coupled with a resistance, the charge transfer resistance, and each interphase is coupled with an additional resistance, for example the resistance of passing charges across an SEI layer. By using two identical Li electrodes (symmetric cell set-up), the interphase resistance of a single electrode is approximately half of the total interphase resistance of the cell. In the following sections, various polymer electrolytes are characterized with both EIS and DRT to demonstrate the applicability of DRT analysis to electrochemical systems and to determine key properties of these materials.

Dry polymer electrolyte xGCD-PCL

The dry polymer electrolyte xGCD-PCL was developed by Liu and coworkers at the Helmholtz-Institute Münster[61] and can be operated at elevated temperatures (40 °C to 60 °C). The polymer structure is composed of cyclodextrine macrocycles grafted with polycaprolactone sidechains. The conductive salt is LiTFSI, added in a ratio of 5:1 of the concentration of carbonyl groups from the polymer relative to that of Li from the salt ([C=O]:[Li]). The impedance spectrum of the dry polymer electrolyte xGCD-PCL between two stainless steel electrodes, as shown in ***Figure 28a***, is analyzed to obtain the overall ionic conductivity of the electrolyte. A characteristic semi-circle forms at higher frequencies (>100 kHz) as a result of geometric capacitance in parallel with bulk electrolyte resistance. At lower frequencies (< 100 Hz), an almost vertical line and thus an increase in mostly the imaginary part of the resistance occurs that is caused by charge separation and subsequent double layer formation at the electrodes (capacitive layer).

(a) (b)

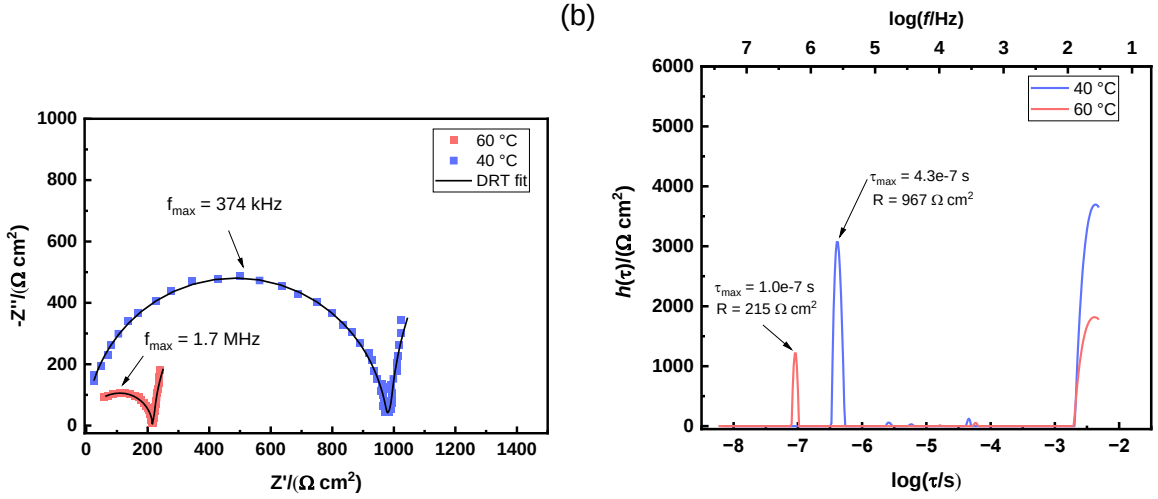

Figure 28: *(a) Nyquist plot of the impedance of polymer electrolyte xGCD-PCL, sandwiched between two stainless-steel electrodes, measured at temperatures of 40 °C and 60 °C. (b) Corresponding DRT plot using a regularization parameter of* $\lambda = 0.05$.

The characteristic frequency or time constant of the semi-circle ($\tau_{max} = RC$) depends on the ionic conductivity and permittivity of the electrolyte, as derived in Eq. (42). Here, $C = \frac{\varepsilon_0 \varepsilon_R A}{d}$ is the capacitance of a parallel plate capacitor with area A and distance d, and $R = \frac{d}{A\,\sigma}$ is the inverse conductance (i.e., resistance) of the electrolyte membrane between the parallel electrodes. In contrast to the resistance, τ_{max} does not depend on the cell's geometry.

$$\tau_{max} = \frac{1}{2\pi f_{max}} = RC = R\frac{\varepsilon_0 \varepsilon_R A}{d} = \frac{d}{A\,\sigma}\frac{\varepsilon_0 \varepsilon_R A}{d} = \frac{\varepsilon_0 \varepsilon_R}{\sigma} \qquad (42)$$

Since the ionic conductivity of electrolytes increases with higher temperature, the characteristic time constant and the resistance decrease accordingly. The semi-circles are well resolved in the DRT plot (***Figure 28b***), and integration of the peaks yields the corresponding resistances, which are already normalized to the electrode area (***Table 1***). The narrow peak width indicates homogeneously distributed charge transport properties within the electrolyte with a single characteristic process rate. An ionic conductivity can be conveniently calculated from the obtained areal resistance for a given electrolyte membrane thickness (here, $d = 100\ \mu m$). Also, the characteristic time constants obtained from DRT can be multiplied with the ionic conductivity to yield the permittivity (and with that, the relative permittivity ε_R) of the electrolyte. The values for the ionic conductivity of xGCD-PCL are in good agreement with those published previously[61] and suggest that this polymer electrolyte can be employed in Li metal batteries that operate at temperatures of 40 °C and 60 °C. The relative permittivity of $\varepsilon_R \approx 50$ is slightly lower than that of common cyclic carbonate-based solvents (e.g. propylene carbonate, $\varepsilon_{R,PC} \approx 66$).[66]

Table 1: *Results obtained from the DRT analysis of the impedance spectroscopy of the dry polymer electrolyte xGCD-PCL between two stainless steel spacers.*

Temperature ***T***/°C	Resistance ***R***/(Ω cm^2)	Time constant $\boldsymbol{\tau}$/s	Conductivity $\boldsymbol{\sigma}$/(S cm^{-1})	Relative permittivity $\boldsymbol{\varepsilon_R}$
40	967	4.3 × 10^{-7}	1.0 × 10^{-5}	49
60	215	1.0 × 10^{-7}	4.7 × 10^{-5}	53

Liquid electrolytes are typically composed of multiple solvents, where those with high relative permittivity facilitate salt de-solvation, whereas those with low relative permittivity (and low viscosity) afford ion transport.[32] Note that the relative permittivity is a complex quantity and thus depends on the applied frequency. For the limit of high frequencies, the real part of the relative permittivity may reach a constant value that is also referred to as dielectric constant (***Figure A2*** in the Appendix). The impedance of xGCD-PCL squeezed between two Li electrodes at a temperature of 60 °C is shown in ***Figure 29***. Both EIS and DRT spectra can be divided into three regions based on the applied frequencies.[67] At high frequencies above 10^5 Hz (below 10^{-6} s), ionic conductivity of the electrolyte is dominating. At moderate frequencies (10^5 Hz > f > 10^1 Hz, or 10^{-6} s < τ < 10^{-2} s), interfacial charge transfer results in a semi-circle in the Nyquist plot. At low frequencies below 10 Hz (above 10^{-2} s), a series of peaks with increasing intensity in the DRT plots is characteristic for diffusive processes, that are also indicated by a straight line in the Nyquist plot. The characteristic frequency of the semi-circle ($f_{\max} = 1.3$ kHz $\widehat{=}$ 1.2×10^{-4} s) fits to the main peak in the DRT plot at 10^{-4} s.

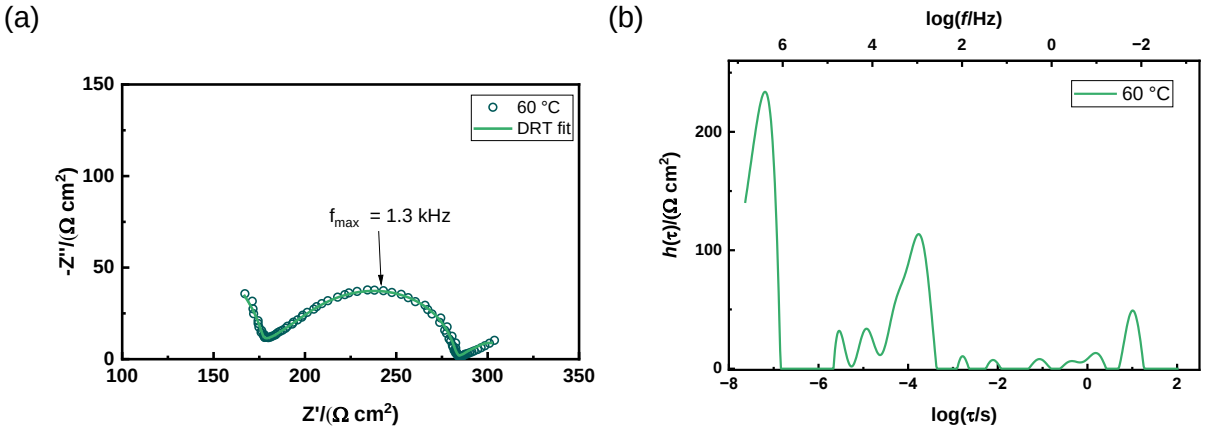

Figure 29: *Impedance of Li||Li cells operated with the solid polymer electrolyte xGCD-PCL at 60 °C in the complex plane (a) and time domain (b). The regularization parameter was* $\lambda = 0.2$.

At a temperature of 40 °C, the impedance is larger than at 60 °C, as visualized in ***Figure 30***. The high frequency resistance associated with the ionic conductivity is more pronounced at this temperature, as expected from previous measurements with blocking electrodes. The characteristic frequency of 800 kHz again fits to the DRT spectrum that shows a large peak at

1.8 x 10^{-7} s. The interphase resistance is also affected by temperature, as the integrated DRT peak area (radius of the second semi-circle) amounts to 210 $\Omega\,\mathrm{cm}^2$ compared to 107 $\Omega\,\mathrm{cm}^2$ at 60 °C. Furthermore, the interphase resistance is not homogenous, but divided into multiple peaks. The more dominant peak is at 1.6 x 10^{-4} s, and the smaller one at lower time constants (1.3 x 10^{-5} s). This indicates that two processes or layers contribute to the overall interphase resistance, for example a more conductive inorganic SEI layer (at lower time constants) and a thicker SEI layer at higher time constants. Similar observations could be made for liquid electrolytes in contact with Li metal.[68,69]

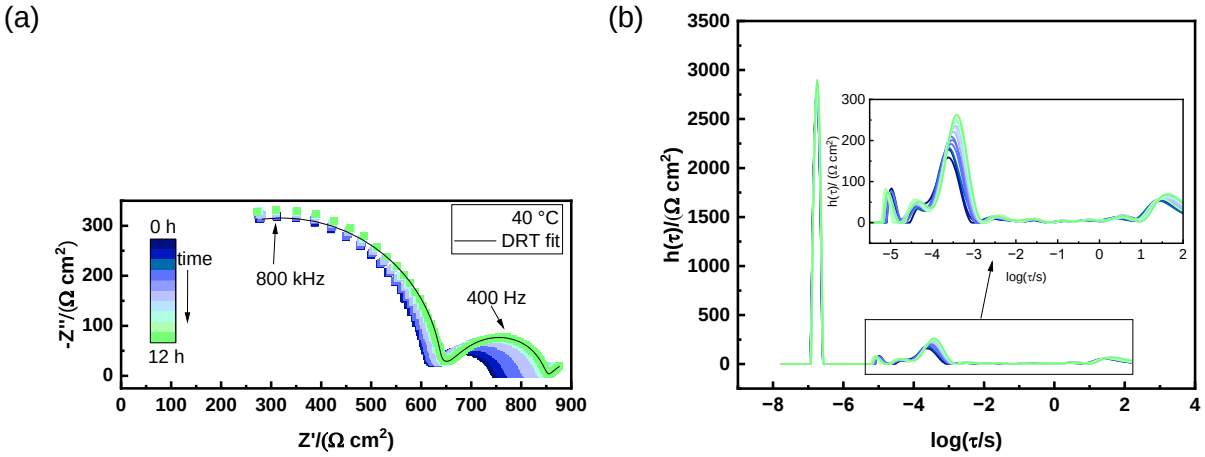

Figure 30: *Impedance of Li||Li cells with the solid polymer electrolyte xGCD-PCL at 40 °C in the complex plane (a) and the time domain (b). The regularization parameter was* $\lambda = 0.2$.

The change of the impedance over time at OCV also indicates that the interphase resistance grows overtime (from initially 128 $\Omega\,\mathrm{cm}^2$, thus ca. 64 %), along with an increase in the resistance associated with ionic conductivity. Interfacial reactions are likely responsible for this increase, as this would result in higher interphase resistances and reduced salt concentration in the electrolyte due to decomposition reactions. An overview of the obtained resistances and associated time constants is shown in ***Table 2***.

Table 2: *Results obtained from the DRT analysis of the impedance spectroscopy of the dry polymer electrolyte xGCD-PCL between two Li metal electrodes at 60 °C and 40 °C.*

Temperature ***T***/°C	Resistance ***R***/($\Omega\,\mathrm{cm}^2$)	Time constant range τ/s	Peak time constant τ_0/s
60	144	< 10^{-6}	6.2 x 10^{-8}
	107	10^{-6} – 10^{-2}	1.3 x 10^{-5} and 1.6 x 10^{-4}
	27	>10^{-2}	-
40	640	< 10^{-6}	1.8 x 10^{-7}
	210	10^{-6} – 10^{-2}	4.3 x 10^{-5} and 3.9 x 10^{-4}
	75	>10^{-2}	-

Notably, the ionic conductivity obtained from the Li||Li cells is slightly higher than that from the blocking electrodes set-up (6.9 x 10^{-5} S cm^{-1} and 1.6 x 10^{-5} S cm^{-1} for 60 °C and 40 °C, respectively). A likely explanation is that the membranes were slightly reduced in thickness by the increased pressure in the coin cell caused by the presence of additional Li electrodes. Thinner membranes have a lower resistance, so that the ionic conductivity is artificially increased by the overestimated thickness. At a thickness of 70 µm instead of 100 µm, the corresponding ionic conductivities obtained from Li||Li cells are similar to those obtained from cells with a blocking electrode set-up. Since even lower electrolyte thicknesses < 30 µm should be favored in terms of energy density of actual cells, further modification of this electrolyte system is required to enable mechanical robustness while maintaining sufficient ionic transport.

Hybrid electrolyte xBtH

Reducing the electrolyte thickness is a convenient approach to increase the energy density of cells, since the electrolyte usually does not store electrochemical energy itself but only transports charge carriers from one electrode compartment to the other. However, thin polymer electrolyte membranes (<30 µm) often do not provide sufficient mechanical stability and thus require a supporting matrix consisting of robust polymer materials such as polyacrylonitrile or polyethylene.[61,70] The hybrid electrolyte membrane xBtH, developed by Chen et al., comprises a thin polyethylene matrix (5 µm) sandwiched between the polycaprolactone-based polymer electrolyte Bt-PCL layers,[57] resulting in an overall electrolyte membrane thickness of 30 µm. The sandwich-type hybrid electrolyte is cross-linked under UV-light for further enhancement of the mechanical stability, thus it is referred to as xBtH. Even though the overall ionic conductivity of the hybrid membrane is expected to be lower compared to a pristine electrolyte membrane (due to reinforcement by a non-conductive matrix), the ionic conductance (inverse resistance) may be higher due to thinner electrolyte membranes. Indeed, the impedance response in ***Figure 31a*** supports this hypothesis, as indicated by the higher real part of the resistance for xBt-PCL and the higher characteristic frequency (proportional to the conductivity). The corresponding DRT spectra (***Figure 31b***) provide even more insights into apparent conduction rates, and the overall conductivity of xBt-PCL membranes is comprised of two characteristic processes at the time constants of $\tau_1 = 4.7 \times 10^{-8}$ s and $\tau_2 = 4.0 \times 10^{-7}$ s, respectively.

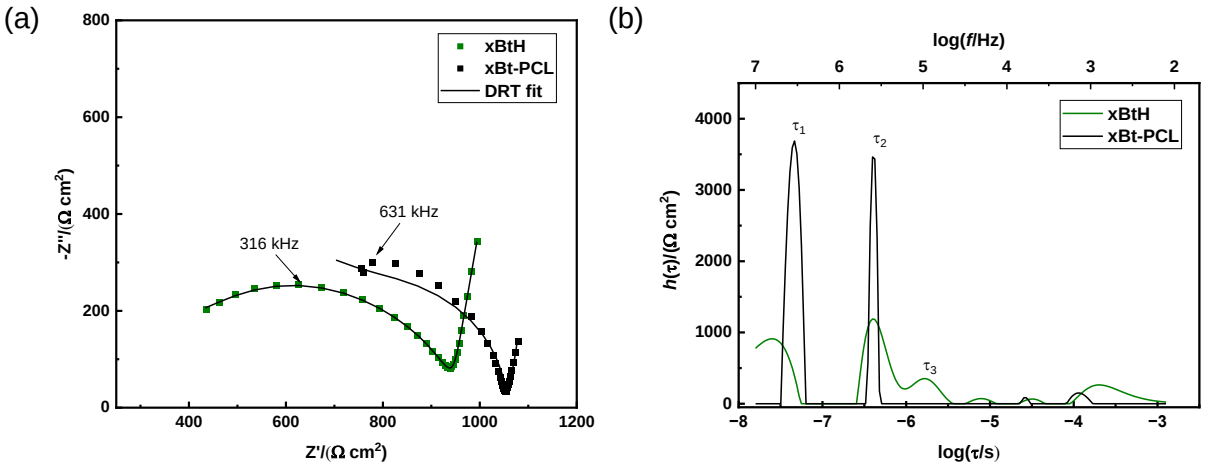

***Figure 31**: (a) Nyquist plot of the impedance of the layered hybrid polymer electrolyte xBtH (30 µm thickness) compared to polymer electrolyte xBt-PCL (100 µm thickness), sandwiched between two stainless-steel electrodes, and measured at 40 °C. (b) Corresponding DRT plot using a regularization parameter of* $\lambda = 0.05$.

It should be noted that the peak of τ_1 corresponds to a frequency of > 3 MHz, thus it is an extrapolated value that lies out of the measurement range (in this case the highest measured frequency was 630 kHz). The authenticity of peak 1 is therefore questionable, also considering the large deviation of the fit in the Nyquist plot at high frequencies. The DRT spectrum for the xBtH membrane reveals a third time constant, $\tau_3 = 1.7 \times 10^{-6}$ s, which likely results from the matrix structure. The results for the xBtH and xBt-PCL membranes against blocking electrodes are summarized in ***Table 3***.

***Table 3:** Results obtained from DRT analysis of the impedance spectroscopy of the xBtH (30 µm) and xBt-PCL (100 µm) polymer electrolytes in a stainless-steel cell set-up at 40 °C.*

	xBt-PCL	xBtH
$\boldsymbol{\tau_1}$/s	4.7×10^{-8}	2.5×10^{-8}
$\boldsymbol{\tau_2}$/s	4.0×10^{-7}	4.0×10^{-7}
$\boldsymbol{\tau_3}$/s	-	1.7×10^{-6}
$\boldsymbol{R_1}/(\Omega\ \mathrm{cm}^2)$	712	386
$\boldsymbol{R_2}/(\Omega\ \mathrm{cm}^2)$	341	398
$\boldsymbol{R_3}/(\Omega\ \mathrm{cm}^2)$	-	127
$\Sigma\ \boldsymbol{R}/(\Omega\ \mathrm{cm}^2)$	1053	911
$\boldsymbol{d}$/µm	100	30
$\boldsymbol{\sigma}$/(S cm^{-1})	9.5×10^{-6}	3.3×10^{-6}

The contact of xBtH with Li metal was analyzed in Li||Li cells with the polymer membrane as free-standing separator and electrolyte. The impedance and corresponding DRT is shown in ***Figure 32***.

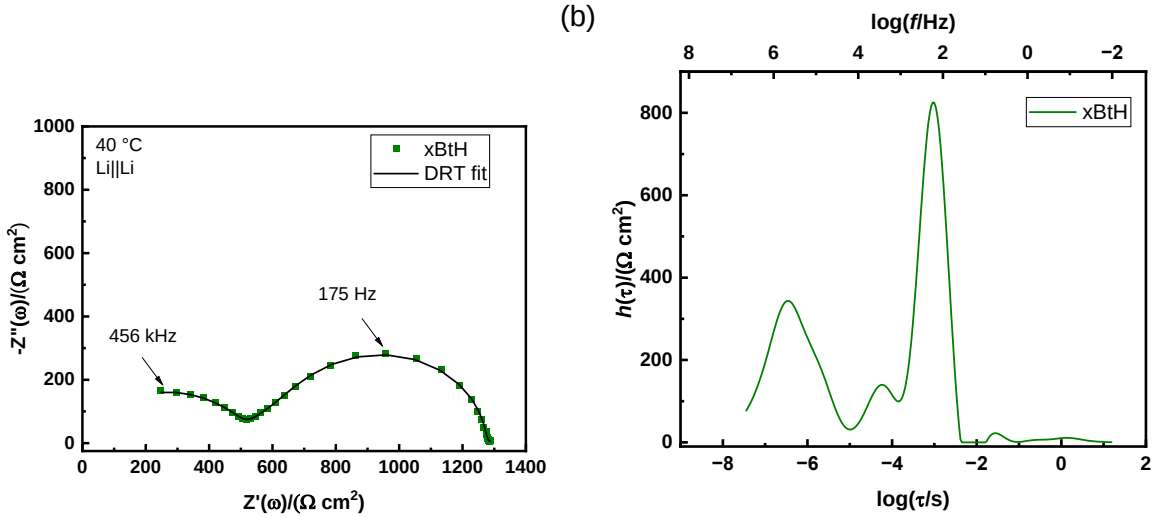

***Figure 32**: (a) Nyquist plot of the impedance of the layered hybrid polymer electrolyte xBtH (30 µm thickness) between two Li electrodes, measured at 40 °C. (b) Corresponding DRT plot using a regularization parameter of $\lambda = 0.5$.*

A clear separation between the resistance due to ionic conduction and due to interphases is also visible here. Below 10^{-5} s, the DRT plot indicates a broad peak for ionic conduction, that is in the similar time constant range than in the blocking set-up. The interphase resistance (between 10^{-5} s and 10^{-2} s) comprises two contributions, which could also be observed for the dry polymer electrolyte xGCD-PCL shown earlier. The quantitative results are listed in ***Table 4***.

***Table 4:** Results obtained from DRT analysis of the impedance spectroscopy of the xBtH (30 µm) polymer electrolyte in a Li||Li cells at 40 °C.*

Temperature ***T***/°C	Resistance ***R***/(Ω cm²)	Time constant range τ/s	Peak time constant τ_0/s
40	484	$< 10^{-5}$	3.3×10^{-7}
	757	$10^{-5} – 10^{-2}$	5.9×10^{-5} and 1×10^{-3}
	21	$>10^{-2}$	-

Gel electrolyte GCD-PTMC

The gel polymer electrolyte GCD-PTMC constitutes another polymer electrolyte that was developed at the Helmholtz-Institute Münster by Chiou et al.[71] and consists of a grafted cyclodextrine core modified with PTMC groups. Additional solvent (propylene carbonate) enhances conductivity at ambient temperatures. An addition of 90 wt% of solvent to GCD-PTMC is denoted as PTMC90. The impedance corresponding to the ionic conductivity at various temperatures is visualized in ***Figure 33***.

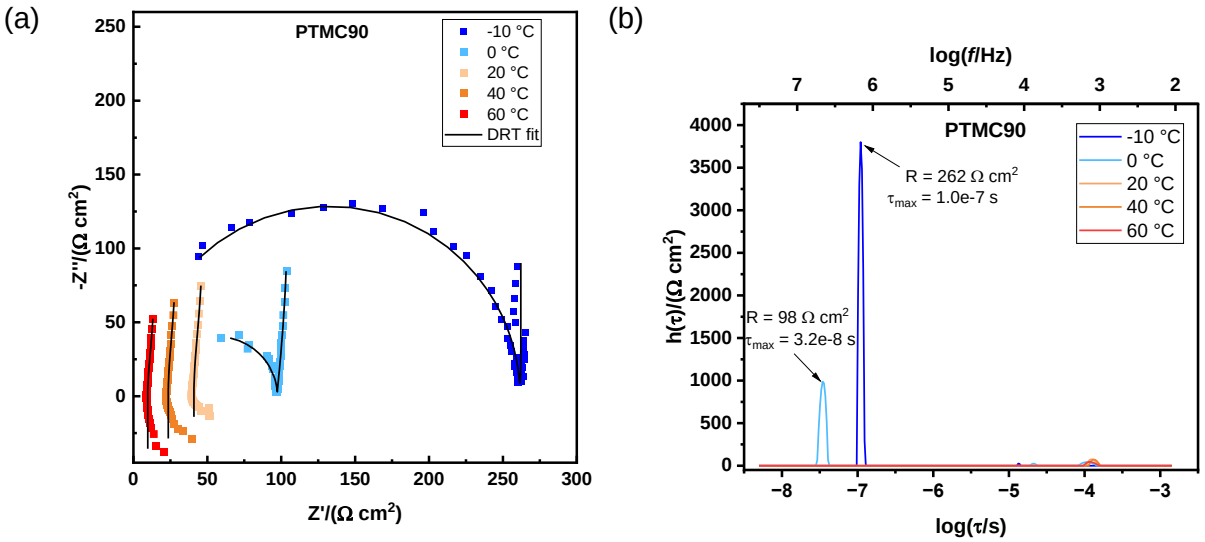

Figure 33: *(a) Nyquist plot of the impedance of gel polymer electrolyte PTMC90, sandwiched between two stainless steel electrodes, measured at various temperatures. (b) Corresponding DRT plot using a regularization parameter of* $\lambda = 0.05$.

Due to the larger amount of solvent, the impedance response at temperatures > 0 °C is comparable to that of liquid electrolytes, in that the semi-circle reflecting geometric capacitance is absent. Only at low temperatures of 0 °C and -10 °C, the ionic conductivity is low enough so that the corresponding time constant is high enough to be within the measured frequency window. Accordingly, the DRT peaks are only visible at -10 °C and 0 °C. Compared to the dry polymer electrolytes shown previously, the ionic conductivity of PTMC90 is more than an order of magnitude higher with 4.6 x 10^{-4} S cm^{-1} at 40 °C.

Table 5: *Results obtained from DRT analysis of the impedance spectroscopy of the gel polymer electrolyte PTMC90.*

Temperature ***T***/°C	Resistance ***R***/(Ω cm^2)	Time constant τ/s	Conductivity σ/(S cm^{-1})	Relative permittivity ε_R
-10	262	1.0×10^{-7}	4.2×10^{-5}	47
0	98	3.2×10^{-8}	1.1×10^{-4}	40
20	41 (from R_{serial})	-	2.7×10^{-4}	-
40	24 (from R_{serial})	-	4.6×10^{-4}	-
60	10 (from R_{serial})	-	1.1×10^{-3}	-

As propylene carbonate is a volatile solvent compared to other components of a polymer electrolyte-based cell, the amount of solvent should be kept to a minimum. The optimal solvent content was determined as 70 wt% in this case.[71] In ***Figure 34***, the impedance of PTMC70 (70 wt% PC in GCD-PTMC) in Li||Li cells is compared to that of 1 M LiTFSI in PC (liquid electrolyte). PTMC70 yielded a substantially larger interphase resistance compared to a liquid

electrolyte, with 700 $\Omega\,cm^2$ compared to 234 $\Omega\,cm^2$, respectively. The DRT peaks indicate that at least parts of the interphase resistance are related to similar processes at similar time constants of ca. 3 x 10^{-4} s for both systems.

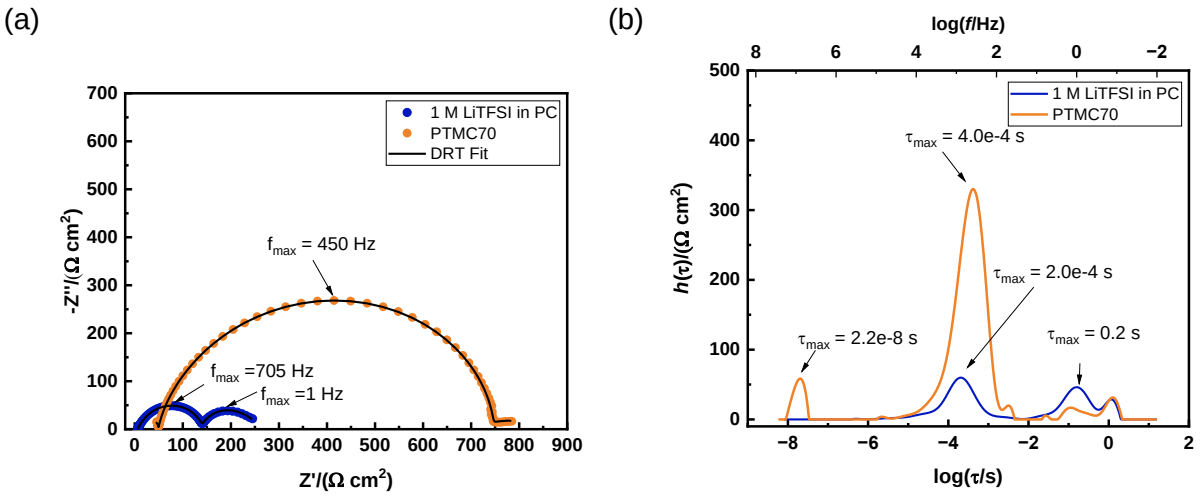

Figure 34: *(a) Nyquist plot of the impedance of gel polymer electrolyte PTMC70 compared to the liquid electrolyte 1 M LiTFSI in PC, in Li||Li cells measured at 20 °C. (b) Corresponding DRT plot using a regularization parameter of* $\lambda = 0.2$.

The results emphasize that an addition of solvent can substantially enhance ionic conductivity and enable operation at ambient temperatures. Here, DRT analysis works as a tool to extract additional information about characteristic rates associated with interphase and bulk charge transport (and corresponding resistances).

Liquid electrolyte with polymer-coated Li electrodes

With the goal of improving the homogeneity of Li metal deposits in liquid electrolyte-based cells, viscoelastic polyborosiloxanes (PBS) were synthesized and coated onto Li metal as part of the preceding master thesis in 2019.[72] One major insight included that the strongly cross-linked siloxane coatings are mechanically robust and yield more homogeneous Li deposits compared to uncoated Li metal electrodes. However, the high degree of cross-linking reduces the liquid electrolyte uptake of intrinsically non-conductive polymer coatings, thus resulting in substantially larger interfacial resistances compared to the reference system. As part of this doctoral thesis, the acquired impedance spectra of Li||Li cells with coated and uncoated Li electrodes were analyzed with DRT to achieve further insights into the evolution and nature of the interfacial resistances. Also, the cycling performance of coated electrodes in LFP||Li cells was evaluated. The interphase impedance of Li||Li cells and corresponding DRT spectra are shown in ***Figure 35a*** and ***b***, respectively. Note that the semi-circles and associated DRT peaks do not reflect ionic conductivity, but purely result from interphase phenomena. This is due to the comparably high ionic conductivity of the liquid electrolyte (> 1 mS cm^{-1}), which corresponds to time constants below the measured range (< 10^{-7} s) and is thus part of the

series resistance (i.e., the anticipated high-frequency intercept with the abscissa). Both systems exhibit two separate semi-circles that correspond to processes that are well separated in the time domain. This could, for example, be based on a heterogeneous SEI structure that locally affords faster or slower charge transport properties. The coated electrodes reveal substantially larger interphase resistance at both relevant regions of relaxation times (10^{-6} s to 10^{-2} s and 10^{-2} s to 10^{2} s). Noteworthy, the relative contribution at higher time constants is larger for the coated system, indicating that outer SEI layers are especially altered by the artificial coating.

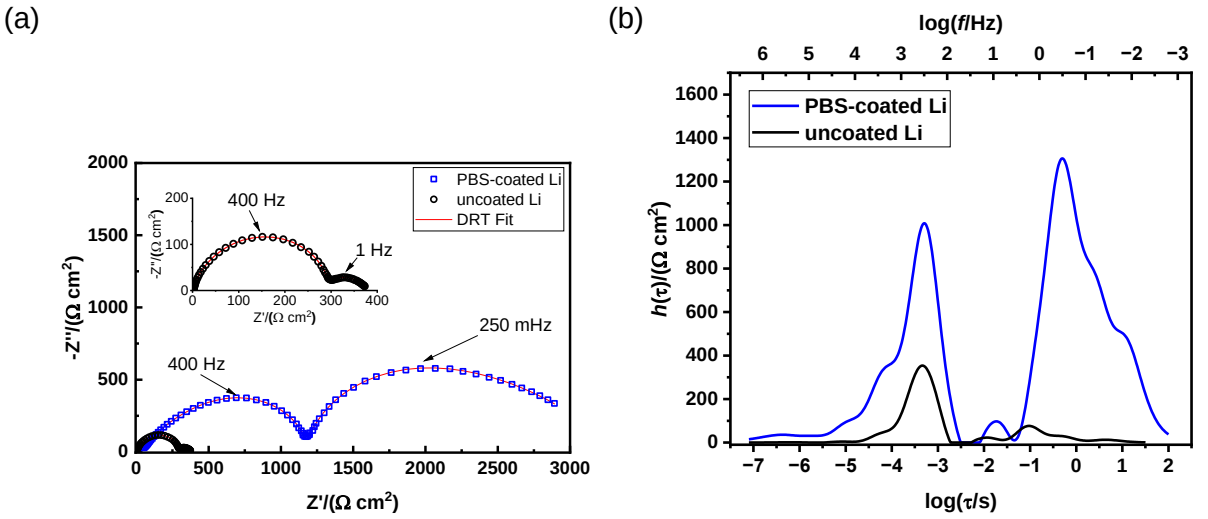

Figure 35: *(a) Impedance plots of Li||Li cells with and without polyborosiloxane(PBS)-coatings after resting for 12 h at 20 °C. (b) Corresponding DRT plots with a regularization parameter of* $\lambda = 0.1$.

The PBS-modified electrodes were further examined in LFP||Li cells at charge/discharge rates of 0.1 C and 1 C with a cathode capacity 0.66 mAh cm^{-2} at a temperature of 20 °C. The cells with coated electrodes perform comparable to those with uncoated electrodes at 0.1 C, though their Coulombic efficiency is less robust throughout cell formation and cycling. Nevertheless, both coated and uncoated Li systems maintain a discharge capacity of 150 mAh g^{-1}, with average Coulombic efficiencies of 99.2 % and 99.1 %, respectively. The cycling stability of the systems is attributed to the high-performing liquid electrolyte (1 M LiTFSI in DOL/DME + 1 wt% $LiNO_3$) and mechanically roll-pressed Li electrodes, creating well-defined and flattened Li metal anode surfaces and native SEI layers.[73] At charge/discharge rates of up to 1 C, the cells with coated electrodes afford, compared to those with uncoated electrodes, 14 % less specific capacity (90 mAh g^{-1} compared to 105 mAh g^{-1}) after formation and 8 % less after 100 cycles (111 mAh g^{-1} compared to 121 mAh g^{-1}). Coulombic efficiencies of > 100 % result from the Li excess on the anode side that is exploited during discharge.

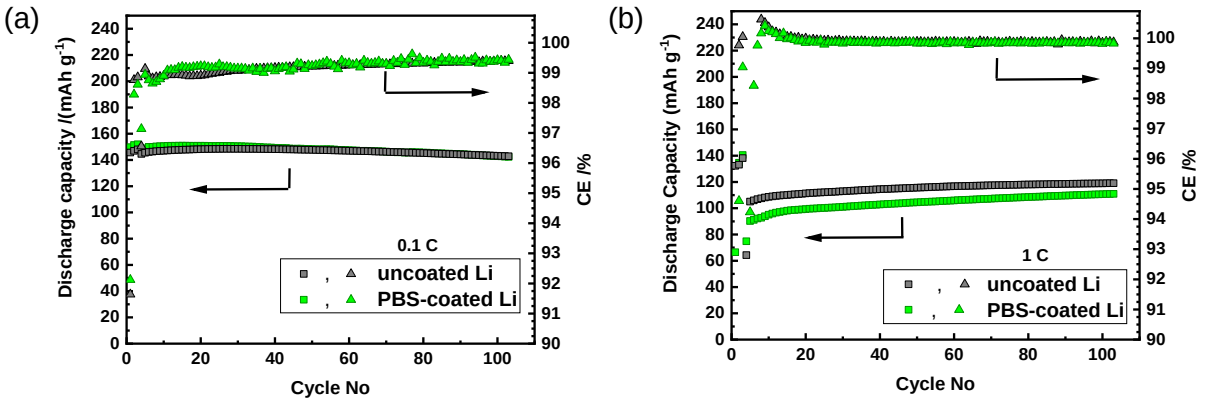

Figure 36: *Specific discharge capacity vs cycle number of LFP||Li cells at a temperature of 20 °C at (a) 0.1 C and (b) 1 C. The formation cyles were 3x0.05 C, the voltage window was 3.0 V – 3.5 V. Reprinted with permission from ref.[62] Copyright © 2024 Elsevier.*

4.1.3 Key achievements of this chapter

The following results of this chapter can be summarized:

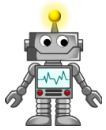

Artificial impedance spectra

- Regularization parameters between $\lambda = 0.1$ and $\lambda = 0.5$ are acceptable for most of the investigated systems, as determined with artificial data. The impact of noise on the DRT spectra is dominant at low regularization ($\lambda = 0.01$) and can be mitigated by surpassing a threshold regularization parameter of $\lambda = 0.1$. At values of $\lambda > 1$, the regularization is too strong, yielding large deviations from experimental data.

Real electrochemical systems [61,62]

- In blocking electrode set-ups, DRT enables quantification of bulk resistances and associated ionic conductivities of polymer electrolytes. Under appropriate conditions, characteristic time constants of the bulk charge transport and permittivity could be identified. In case of blocking electrodes, a regularization parameter of 0.05 was often suitable due to low noise level and well-defined electrode surfaces.
- In Li||Li cells, the bulk electrolyte and interfacial resistances could be quantified. The characteristic time constants of interfacial reactions could be resolved, yielding insights into fast and slow processes at electrode interphases.
- Most time constants of interphase resistances are between 10^{-6} s and 10^{-2} s, where temperature and addition of solvents (forming gel electrolytes) could enhance time constants and reduce both bulk and interphase resistances.
- An addition of a non-conductive matrix to the dry polymer electrolyte xBt-PCL enables thin electrolytes (30 µm), but causes additional resistive contributions to the bulk resistance. Relevant contributions could be resolved in the DRT spectra for the blocking electrode set-up.

4.2 Monitoring of Li microstructures

While electrochemical observables extracted by EIS and DRT, such as interphase resistances and time constants, are important for improving batteries, they provide only limited (or indirect) insights into the dynamic changes of the microstructures of the electrodes. Yet, monitoring the evolution of Li metal deposit microstructures upon cell operation is a critical step towards better understanding of the reversibility of Li inventory in rechargeable Li metal batteries. It comprises all available Li species that contribute to the electrochemical reactions within electrochemical cells, including dense metallic Li, “surface roughened” Li deposits, and coordinated Li ions trapped within electrodes. In view of achieving excellent cell longevity, reversible Li inventory is highly important since irreversible Li losses (e.g. due to side-reactions) limit both the storable energy and capacity at each cycle. Here, smart coupling of electrochemical and analytical methods yields valuable strategies to provide relevant insights into prominent cell failure mechanisms and options for enabling more reversible cell chemistry. In this chapter, data from electrochemical impedance spectroscopy and *in situ* X-ray microtomography are combined to correlate observable electrochemical features with microstructural changes of Li metal deposits upon cell cycling. Also, *in situ* solid-state ^{7}Li NMR spectroscopy is utilized to evaluate the Li microstructures upon charging of a Li metal electrode modified with polymer coatings.

4.2.1 Li microstructures and cell failure

In joint work with Prof. Nitash Balsara (Lawrence Berkeley National Laboratory, LBNL), non-destructive *in situ* X-ray microtomography and electrochemical impedance spectroscopy were exploited to unravel details of failure mechanisms in Li||Li cells at various operating conditions (***Figure 37***). Parts of this section were reported in a peer reviewed article:

- L. Frenck, P. Lennartz, D. Y. Parkinson, M. Winter, N. P. Balsara, G. Brunklaus: Failure Mechanisms at the Interfaces between Lithium Metal Electrodes and a Single-Ion Conducting Polymer Gel Electrolyte*, ACS Applied Materials and Interfaces,* 14, 48, 53893 – 53903, 2022, [https://doi.org/10.1021/acsami.2c16869].

The considered electrochemical cells include single-ion conducting gel polymers sandwiched between two Li metal electrodes. A set of three cells was galvanostatically cycled by applying a current density of 0.1 mA cm^{-2} for 4 h, followed by a relaxation step of 45 min (as well as subsequent EIS measurements) before the current was reversed to -1 mA cm^{-2} for 4 h. This was repeated until the cells failed, for example due to a short circuit between both electrodes. Another set of three cells was cycled at current densities of ±0.3 mA cm^{-2} for 4 h.

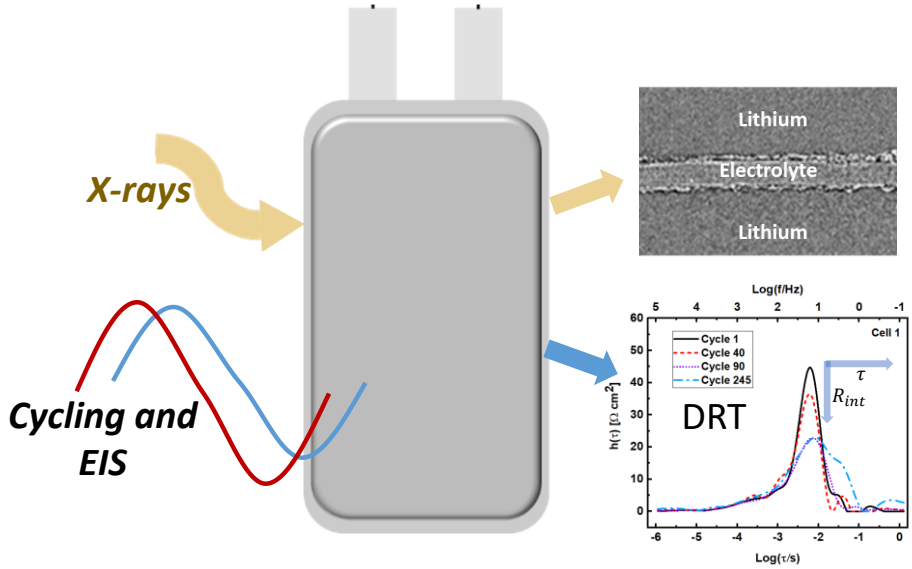

Figure 37: *Overview of the analysis methods and obtained results of the investigation of Li||Li cells during constant-current cycling. Reprinted with permission from ref.[53] Copyright © 2024 American Chemical Society.*

Ten conditioning cycles were performed during the first 100 h at a small current density of 0.02 mA cm^{-2} to stabilize the electrode|electrolyte interfaces. All experiments were performed at a temperature of 25 °C. The cells were imaged by X-ray microtomography prior to cycling, after 40 cycles, after 87 cycles and after cell failure. The open circuit voltage of the cells was close to zero (ca. 2 mV, see Appendix ***Figure A3***), as anticipated for Li||Li cells. Hence, the recorded voltage profiles can be considered as pure overvoltage curves that result from faradaic and non-faradaic contributions. In particular, these contributions comprise an instantaneous response due to the Ohmic resistance of the assembled cells and contributions from mass transfer across the electrodes. At comparably low current densities of ±0.1 mA cm^{-2} the overvoltage of cell 1 initially amounts to ±300 mV and decreases to ±240 mV during 100 cycles (ca. 1000 h), before increasing to ±340 mV until cell failure (***Figure 38a***). The almost square-wave-like shape of the overvoltage curves is characteristic for single-ion conducting electrolytes, where a formation of concentration gradients is largely prevented due to immobilized anions. Therefore, the overvoltage mainly results from Ohmic resistances that occur upon application of currents. Note that time gaps in ***Figure 38a*** correspond to times where the procedure was paused to perform X-ray microtomography (after 40 cycles and 87 cycles). Towards the end of cycling life, the overvoltage exhibits spikes, indicating micro cell shortages that eventually terminate cell operation after 245 cycles (2667 h). When the cells are cycled at a current density of ±0.3 mA cm^{-2}, the cell voltage after the conditioning cycles is roughly three times higher (800 mV) compared to that of the cells cycled at ±0.1 mA cm^{-2}, as anticipated from Ohm's law (***Figure 38b***).

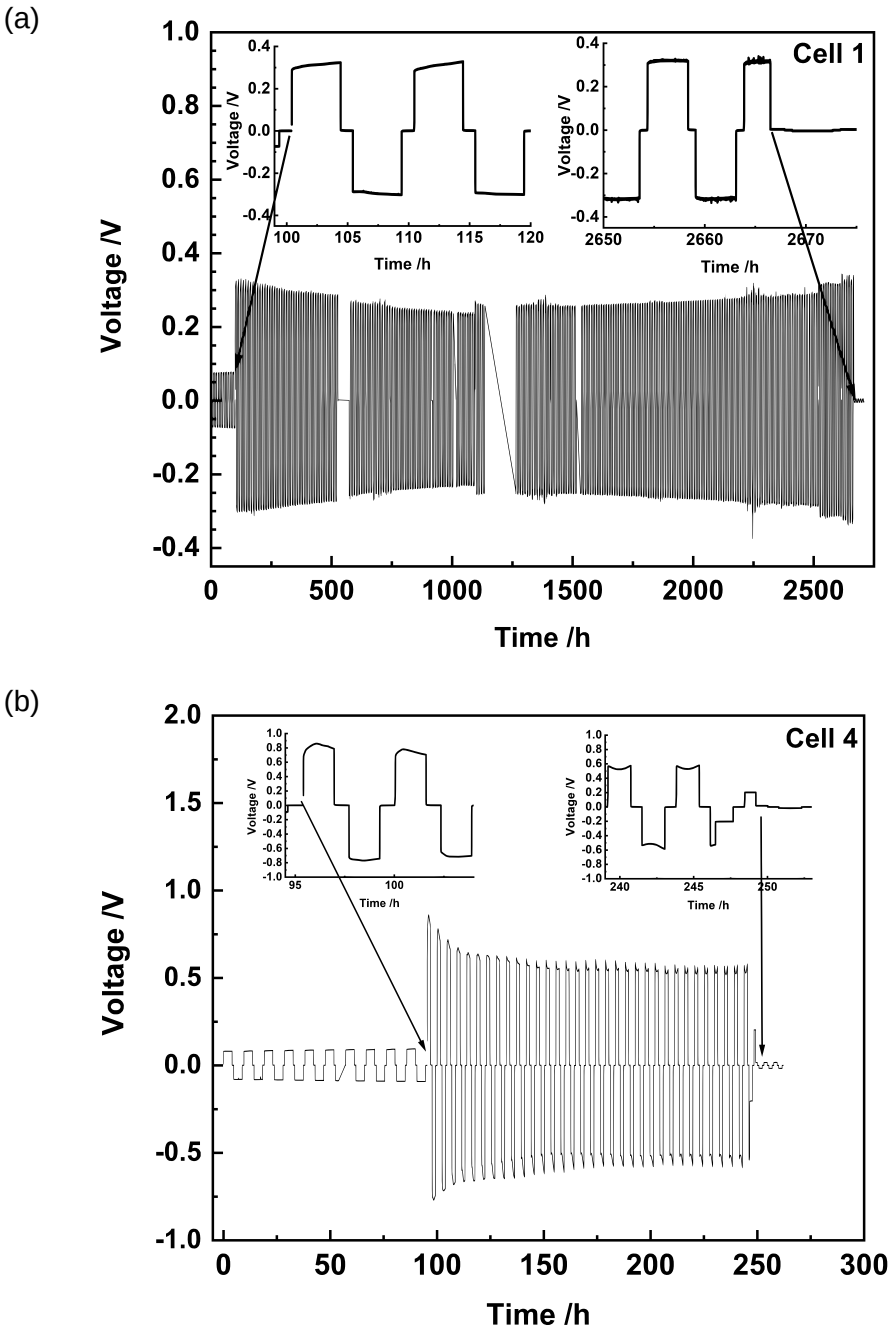

Figure 38: *Overvoltage as a function of time for (a) cell 1 operated at a current density of 0.1 mA cm^{-2} (corresponding to a capacity of 0.4 mAh cm^{-2} per half cycle) and (b) cell 4 cycled at a current density of 0.3 mA cm^{-2} (1.2 mAh cm^{-2}). A lower current density of 0.02 mA cm^{-2} is applied to all the cells during the first 100 h for conditioning. The time gaps correspond to experimental time at the beamline. Reprinted with permission from ref.[53] Copyright © 2024 American Chemical Society.*

Note that the voltage profiles appear less square-wave-like, which is an indication of mass transport limitations and polarization effects.[74] After five cycles, the overvoltage stabilizes at ca. 500 mV before an abrupt cell failure at cycle 31. All three cells cycled at 0.3 mA cm^{-2} achieved similar cell lifetimes with an average of 28 ± 3 cycles. As the overvoltage curves alone generally do not allow straightforward diagnosis of cell failures, the interfacial resistance

is quantified with EIS and DRT and visualized as function of cycle number in ***Figure 39***. The observable resistances are comparable to other reported single-ion conducting gel polymer electrolytes at 25 °C.[75,76] Note that the bulk resistance was subtracted from the total impedance and quantification was done by integrating the corresponding DRT spectra in a frequency window of 1 Hz to 14 kHz (***Figure A4*** in the Appendix).

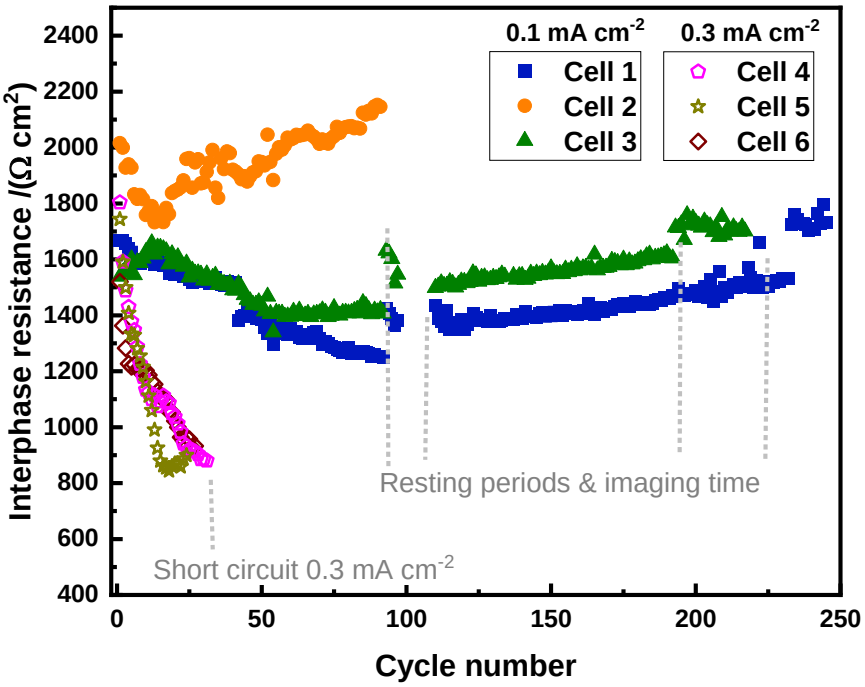

Figure 39*: Interphase resistances with respect to the cycle number at current densities of 0.1 mA cm^{-2} (cells 1, 2, 3) and 0.3 mA cm^{-2} (cells 4, 5, 6), respectively. Due to software issues, no impedance data was recorded between cycles 97 and 110. Abrupt changes in interphase resistances for cells 1 and 3 are caused by open circuit resting periods (beam line imaging time) and are marked accordingly. Reprinted with permission from ref.[53] Copyright © 2024 American Chemical Society.*

The interphase resistances of cells 1 to 3 qualitatively follow the same trend, in that an initial decline is followed by an increase in resistance. For cells 1 and 3, the interphase resistances decrease during to the first 100 cycles from 1600 Ω cm² to 1200 Ω cm² and 1400 Ω cm², respectively, and subsequently increase until the cycling ends (> 220 cycles). The decrease and subsequent increase of the resistance occurs within a shorter time frame for cell 2. Even though all six investigated cells were principally built the same way and comprised the same materials, cell 2 is an outlier. The average initial interphase resistance of the other five cells after formation is (1655 ± 111) Ω cm², which corresponds to a relative standard deviation of ± 6.7 %. In contrast, the interphase resistance of cell 2 after formation is more than 20 % higher than the average (2015 Ω cm²). Cell 2 likely contained an electrolyte membrane with different properties (e.g., due to different solvent content), which in turn caused an interphase with increased resistance during the formation cycles and eventually led to a comparably early cell

failure after 91 cycles. In contrast to cells 1, 2, and 3, the cells cycled at higher current density (0.3 mA cm^{-2}) show a different behavior with a strong decrease in interphase resistance from 1600 Ω cm^2 to 900 Ω cm^2 after less than 30 cycles. It was hypothesized that the decrease in interphase resistance for all the cells is caused by an increase in microscopical surface area of the Li metal deposits. X-ray microtomographic images confirm this hypothesis (see following pages). Upon cycling, the Li electrodes become increasingly rougher so that the effective interfacial area increases. As the same amount of current now passes through a larger effective interfacial area, the observed resistances are lower. To further support this hypothesis and relate the observed impedance to charge transfer processes, DRT analysis of the acquired impedance spectra is conducted. The DRT spectra and Nyquist plots of cell 1 (cycled at 0.1 mA cm^{-2}) are presented in ***Figure 40a*** and ***b***, respectively.

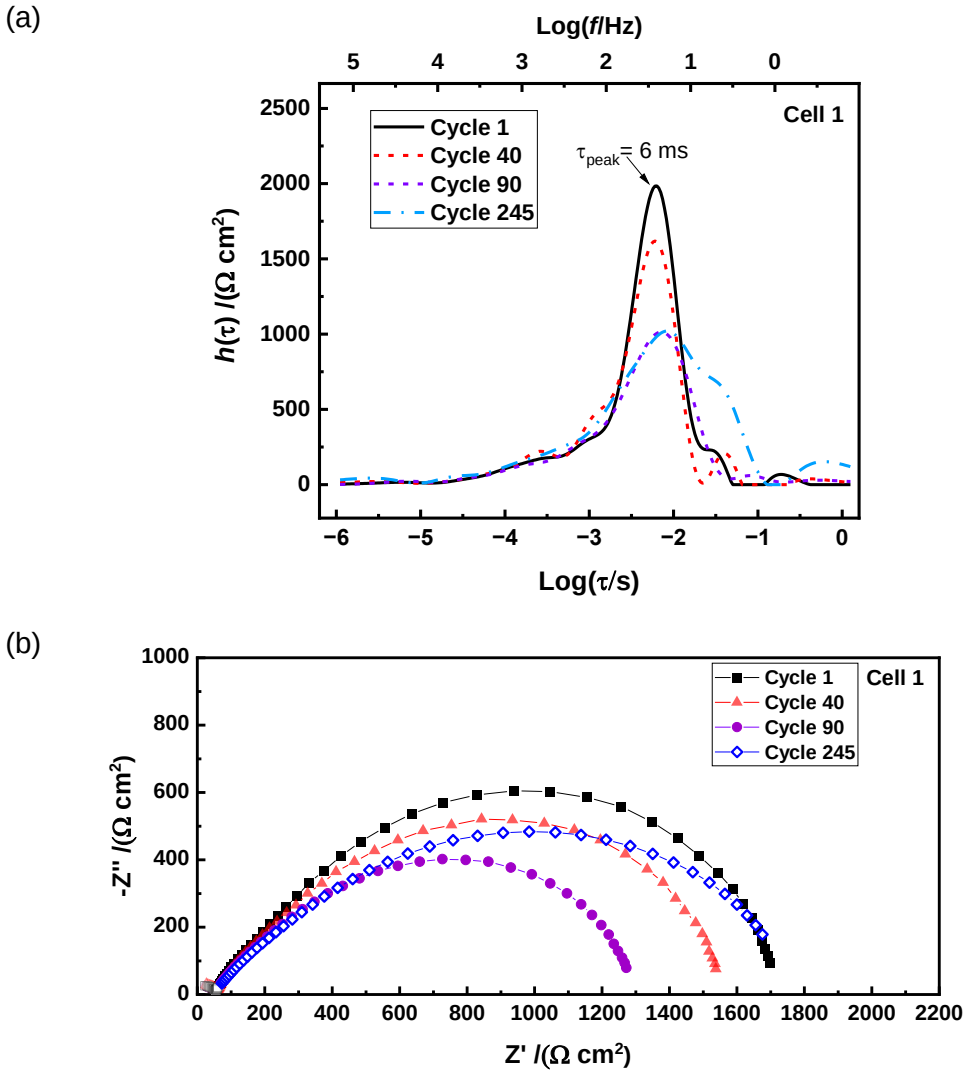

Figure 40*: (a) DRT spectrum of overall impedances of cell 1 at cycles 1, 40, 90, and 245 (cycling current density of 0.1 mA cm^{-2}). (b) Nyquist plot of the normalized areal impedances of cell 1. Reprinted with permission from ref.*[53] *Copyright © 2024 American Chemical Society.*

The characteristic time constants of interfacial charge transfer are given by the peak position of the DRT spectra and are at about $\tau_{\mathrm{peak}} = 6\ \mathrm{ms}$ for all cells, initially. In addition, occurring peaks at lower time constants are less distinct. The reduction in the peak area between cycles 1 and 40 is consistent with the declining interphase resistance. While the peak area decreases further during the first 90 cycles, the peak time constant remains constant, indicating only minimal variation in the composition of the SEI and associated reaction rates. Instead, augmentation of the interfacial area is the root cause of the decrease in interphase resistance. The additional interfacial area at cell cycle 90 ranges between 15 % and 20 % in case of the cells 1 and 3, relative to the pristine cells.

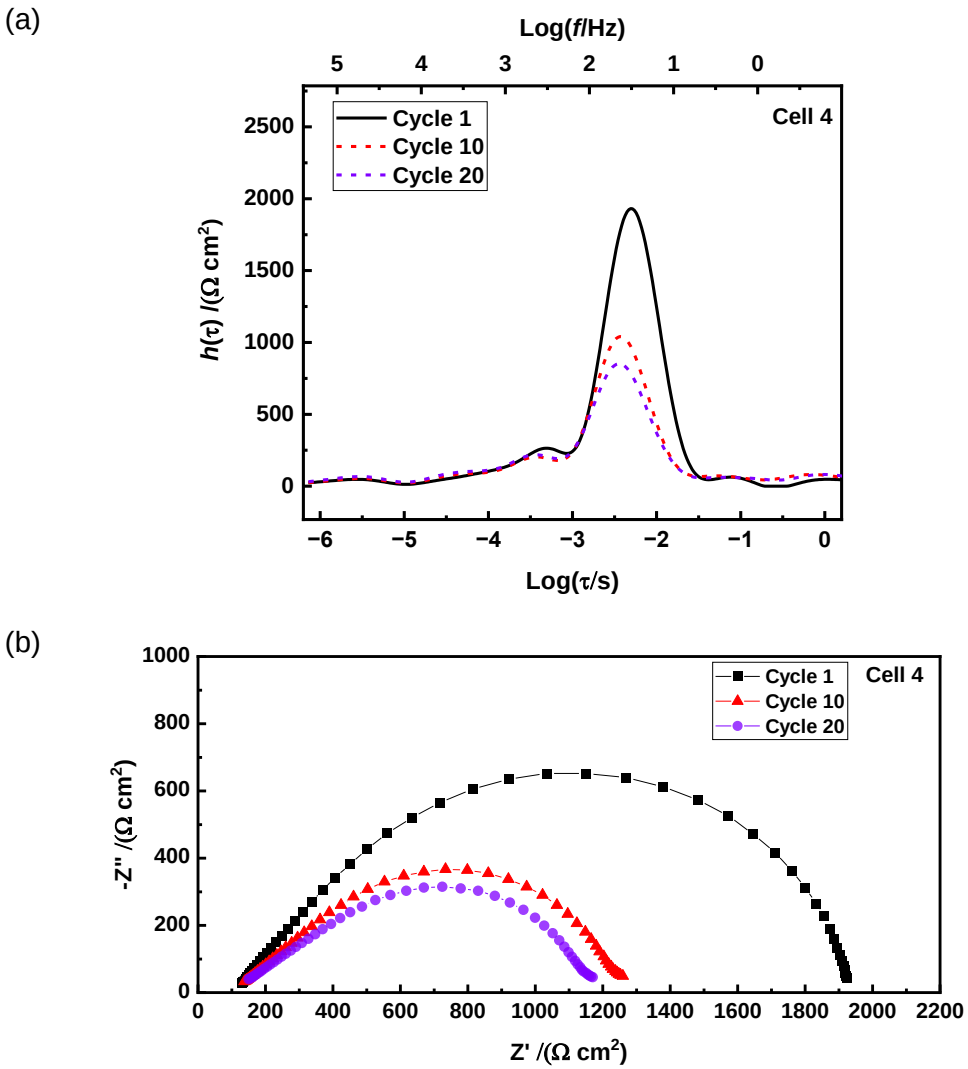

***Figure 41**: (a) DRT spectrum of the overall impedances of cell 4 for cycles 1, 10, and 20 (cycling current density of 0.3 mA cm^{-2}). (b) Nyquist plot of normalized areal impedances of cell 4. Reprinted with permission from ref.*[53] *Copyright © 2024 American Chemical Society.*

Upon prolonged cycling for >90 cycles, the increasing interphase resistance is associated with the occurrence of slower transport processes, as indicated by an additional peak at higher time constants. The Nyquist and DRT plots of cell 2 and cell 3 are provided in ***Figure A8*** and ***Figure***

A9 in the Appendix, respectively. The DRT and Nyquist plots of cell 4 are shown in ***Figure 41a*** and ***b***, as a representative for the cells cycled at higher current densities of 0.3 mA cm^{-2}. Here, the interphase resistance decreases substantially faster compared to that of cell 1. The peak time constant slightly shifts from 6 ms to 4 ms throughout the experiment, potentially indicating enhanced interfacial processes and associated changes in the nature of the SEI. The additional interfacial area at cell failure relative to the pristine cell is about 40 % for cells 4, 5 and 6. The Nyquist and DRT plots of cell 5 and cell 6 are provided in ***Figure A10*** and ***Figure A11*** in the Appendix, respectively.

To further exemplify the interfacial changes upon cycling, hard X-ray microtomography measurements of the cells was performed after the conditioning cycles, then after 40 cycles, 87 cycles, and after cell failure. After 10 conditioning cycles, three characteristic regions could be identified in the reconstructed X-ray tomogram (***Figure 42a***). Here, the cartesian coordinates are defined so that the z-direction is parallel to the nominal direction of the applied current. The top and bottom dark grey bands are the bulk Li metal, while the lighter band in the middle is the polymer electrolyte membrane with a thickness of 50 µm. In general, materials with lower X-ray absorption coefficients appear darker (e.g., Li metal), whereas materials with higher X-ray absorption coefficients (e.g., polymers that contain heavier atoms than Li) appear brighter.[77] The dark and bright thin bands at the interfaces between Li metal and polymer electrolytes is caused by Fresnel phase contrast.[78,79] Two types of impurities could be detected in the illuminated cells, namely darker spots in the Li metal, as well as brighter spots in the electrolyte. ***Figure 42b*** and ***c*** further present top views of Li metal and electrolyte, respectively. The Li impurities vary in size and shape and could be observed in previous studies. They could be identified as crystalline impurity particles comprising lithium oxide (Li_2O), lithium nitride (Li_3N), or lithium hydroxide (LiOH).[80,81] The impurities in the polymer electrolyte are randomly distributed across the membrane and vary in size from 3 µm to 50 µm (cf. ***Figure A12*** in the Appendix). Considering their random distribution and bright X-ray contrast, the polymer impurities are most likely attributed to undissolved components during fabrication of the membranes. The single-ion conducting polymer membrane and the co-polymer PVDF-HFP were added to the solvent (NMP) and stirred overnight at 60 °C, indicating that longer stirring periods may be required in the future to minimize impurities.

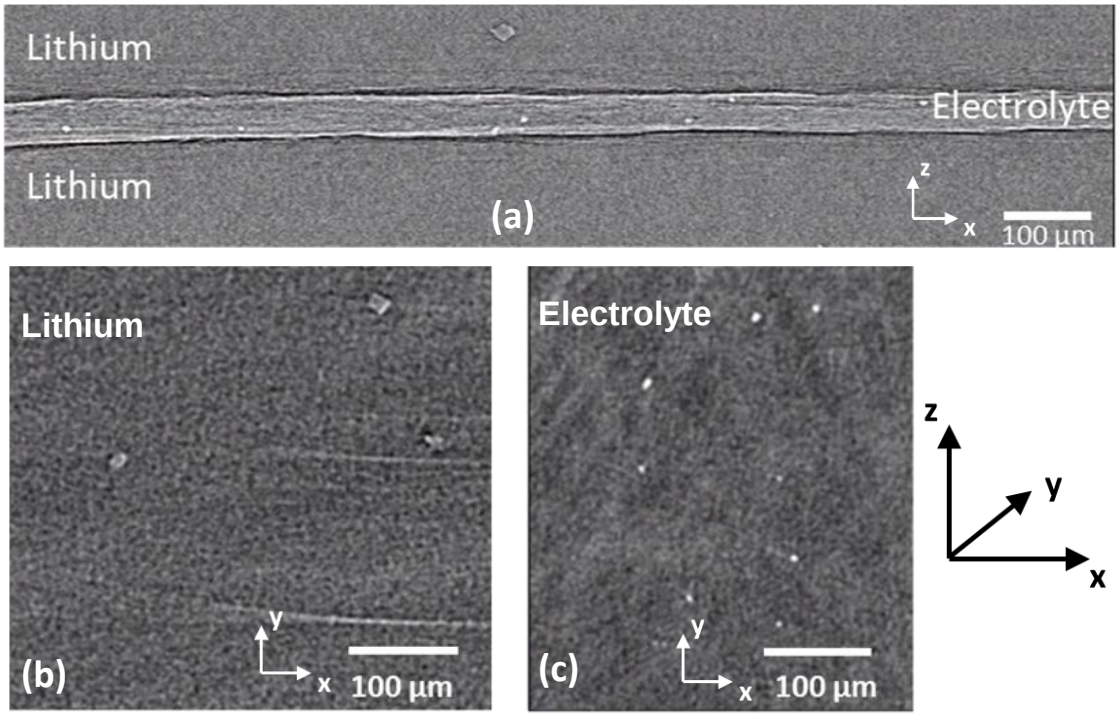

Figure 42: *X-ray microtomograhic images of an exemplary cell after 10 formation cycles with a current density of 0.02 mA cm^{-2}. (a) Cross-sectional slice (xz-plane) through the conditioned Li||Li cell containing a single-ion conducting gel polymer electrolyte. (b) Top view (xy-plane) of the Li metal electrode. (c) Top view (xy-plane) of the single-ion conducting gel polymer electrolyte. Reprinted with permission from ref.[53] Copyright © 2024 American Chemical Society.*

Imaging of the cells during cycling with a current density of 0.1 mA cm^{-2} revealed that these impurities are key to non-homogeneous Li deposition and act as hotspots for growth of non-planar Li metal. In ***Figure 43***, three different types of Li protrusions are visualized after 40 and 87 cycles. A large globular defect nucleated from electrolyte impurities, which caused a substantial thinning of the electrolyte membrane (***Figure 43a***). The cross-sectional (xz-plane) diameter of the Li protrusion increased from 41 µm to 62 µm, thus corresponding to a growth of 50 % in just 47 cycles. Another Li deposit growth could be observed at no visible impurity (***Figure 43b***). Here, the growth is less pronounced and can be characterized as more mossy-like compared to the deposits near the electrolyte impurities. Also, a larger part of the deposits is located in the electrode rather than the electrolyte. It is likely that the impurity was too small to be resolved. The deposit that nucleated at a Li metal impurity (***Figure 43c***) did not grow substantially during cycling.

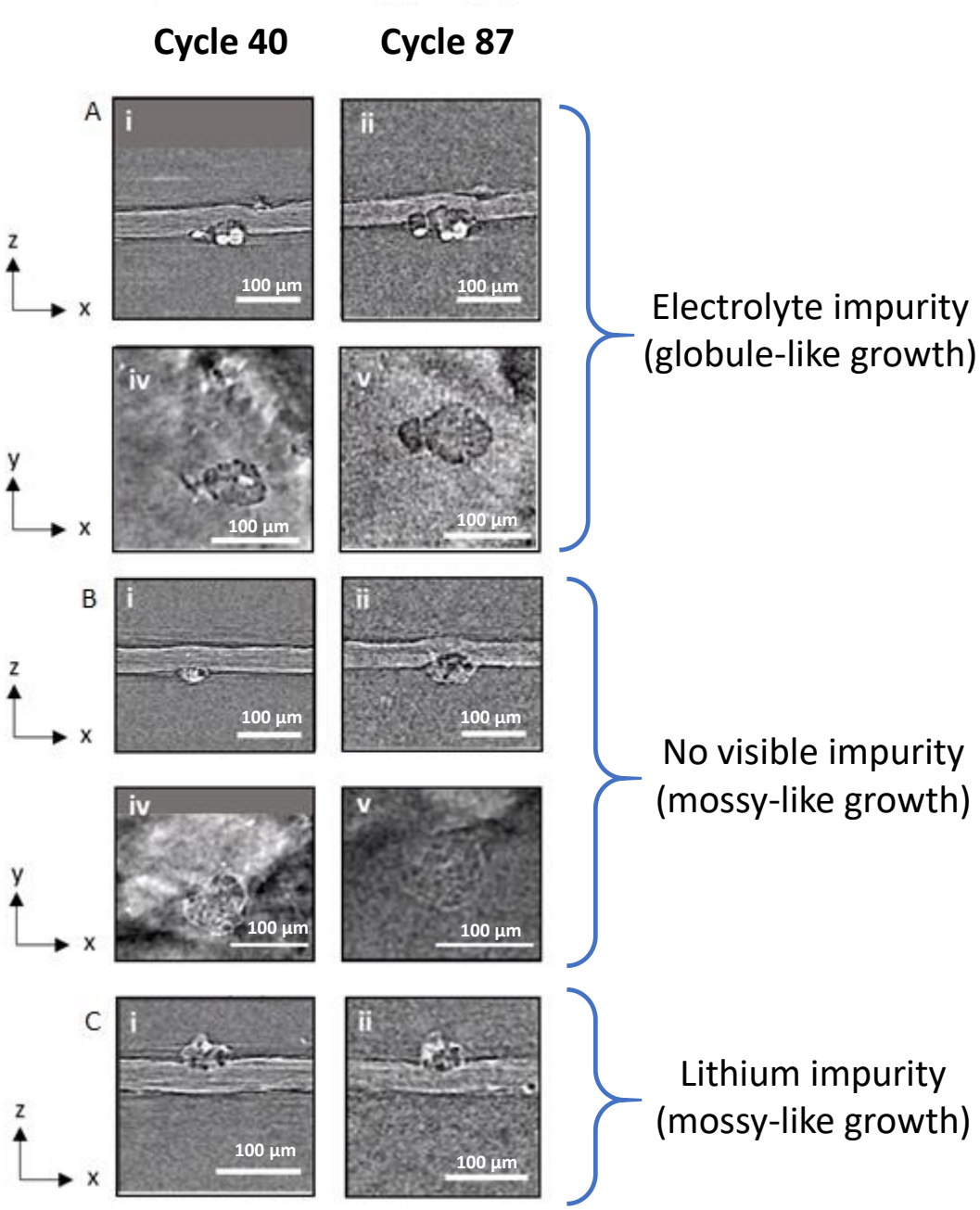

Figure 43: *Cross-sectional slices of a Li||Li cell after 40 and 87 cycles, focusing on the same impurities inside the cell over time. (a) Electrolyte impurities and associated globular growth of Li deposits. (b) Mossy-like growth of Li deposits at no visible impurity. (c) Li impurities and associated mossy growth of Li deposits. Reprinted with permission from ref.[53] Copyright © 2024 American Chemical Society.*

Upon continuous cycling with a current density of 0.1 mA cm^{-2}, the globular deposits nucleating at electrolyte impurities eventually caused a rupture of the electrolyte membrane, as visualized in ***Figure 44***. The globular structure not only grows into the electrode, but also into the electrolyte. All of the cells cycled at 0.1 mA cm^{-2} showed similar short circuit characteristics by these membrane ruptures. Despite that the majority of the cross-sections did not reveal

globular but rather planar Li growth (cf. ***Figure A13***), the hotspots of globular nucleation at impurities is the dominant failure mode at a current density of 0.1 mA cm^{-2}.

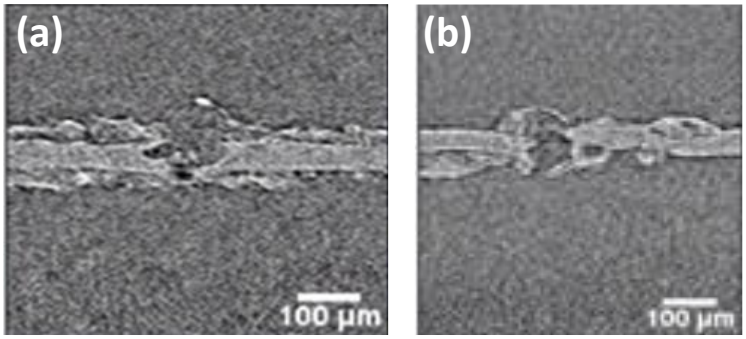

Figure 44: *Cross-sectional slices (xz-plane) of a Li||Li cell (cell 1) after cell failure (cycling with 0.1 mA cm^{-2}), focusing on the a single Li protrusion after 240 cycles. The protrusion originated from an electrolyte impurity and eventually caused a short ciruit of the cell. Images (a) and (b) show the same protrusion from different angles. Reprinted with permission from ref.[53] Copyright © 2024 American Chemical Society.*

The cells cycled at 0.3 mA cm^{-2} could only be monitored by X-ray microtomography after cell failure, as they failed before the first planned tomography experiment at 40 cycles. At a current density of 0.3 mA cm^{-2}, the observed microstructures were strikingly different from that of the cells cycled at 0.1 mA cm^{-2} (***Figure 45***). Instead of large globular deposits, the electrodes were largely covered with mossy Li deposits and showed partly planar Li growth (***Figure 45b*** *right side*). Short circuits by rupturing of the membrane could not be observed, indicating that the pathways for electronic conduction could be in the form of thin filamentous structures (e.g., dendritic Li) that could not be resolved in the experiment. The augmentation of the interfacial area, as hypothesized from the EIS/DRT experiments (***Figure 41***) could be confirmed. Thus, it can be concluded that at the higher current density of 0.3 mA cm^{-2}, the dominating failure mode is based on kinetic limits of the electrolyte and substantial growth of high surface area Li (mossy-type), which further promotes electrolyte degradation through surface reactions.

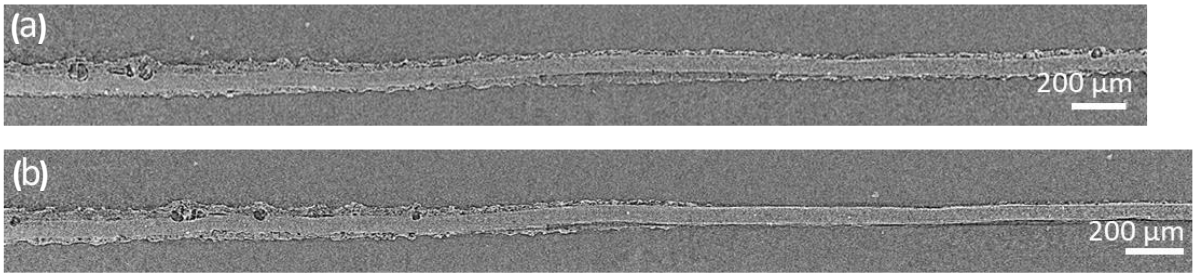

Figure 45: *Cross-sectional slices (xz-plane) of a Li||Li cell after cell failure (cycling with 0.3 mA cm^{-2}). Images (a) and (b) show the same membrane at different positions, highlighting regions with high and low amount of mossy Li deposits. Reprinted with permission from ref.[53] Copyright © 2024 American Chemical Society.*

4.2.2 Li microstructures on modified Li electrodes

In collaboration with Prof. Donghai Wang (Pennsylvania State University, (PSU)), Li metal anodes were modified with polymer-based coatings and characterized with EIS/DRT and *in situ* ^{7}Li NMR spectroscopy. The artificial coatings were designed to afford homogeneous Li metal deposition based on tailored interphase formation and thereby enhance cell longevity.[56] PSU provided the polymer coating solutions consisting of polyethylene oxide (PEO)-functionalized silica (PEOS), as well as crown-ether-functionalized silica (CES) dissolved in NMP. The coating solutions were applied in Münster to Li metal anodes by blade-casting, with further details provided in the experimental section. Parts of this section were already published:[56]

- G. Li, P. Lennartz, G. Brunklaus, D. Wang et al.: Interfacial solvation-structure regulation for stable Li metal anode by a desolvation coating technique, *Proceedings of the National Academy of Sciences of the United States of America*, 121, 2024, [https://doi.org/ 10.1073/pnas.2311732121]

As a proof-of-concept, Li||Li cells with and without PEOS coatings were assembled and their electrochemical impedance was compared to that of untreated Li metal anodes. The employed liquid electrolyte was LP47 (1 M $LiPF_6$ in EC/DEC 3:7 wt.), an established electrolyte for operation of Li metal based systems.[59] ***Figure 46*** displays the impedance spectra of Li||Li cells with and without PEOS-based coatings (a), as well as the corresponding DRT spectra (b).

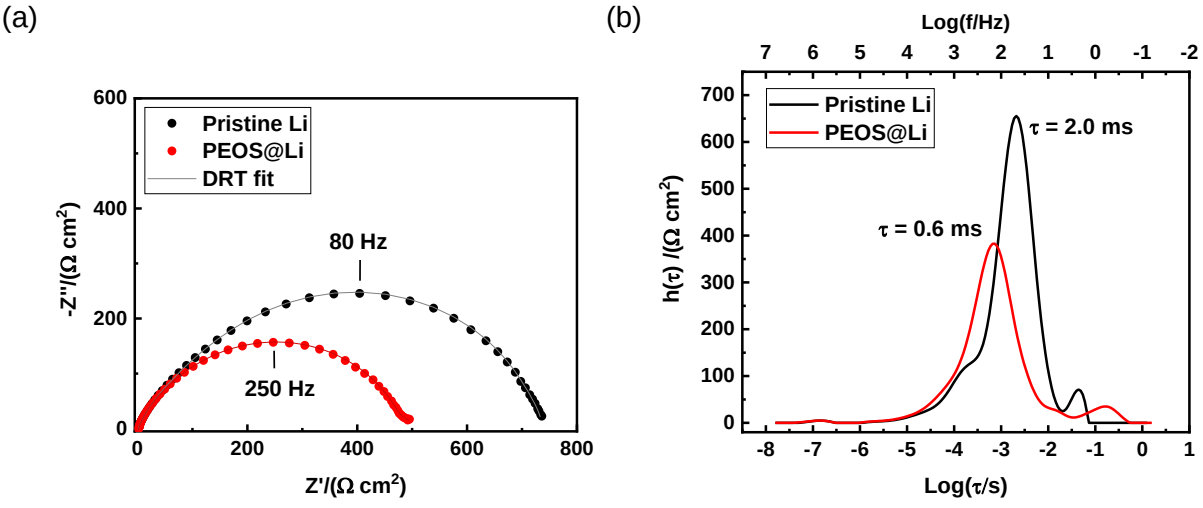

Figure 46*: Impedance (a) and corresponding DRT spectra (b) of Li||Li cells with pristine and PEOS-coated Li metal electrodes, operated with electrolyte LP47 (1 M $LiPF_6$ in EC/DEC 3:7 wt). The regularization parameter was set to* $\lambda = 0.2$.

The interfacial resistances of 490 Ω cm^2 for the coated system are smaller than those of the uncoated systems (730 Ω cm^2). The corresponding DRT not only illustrates the lower interfacial

resistance (smaller peak area), but also enables analysis in either the frequency or time dimension. Large parts of the processes occurring at electrode interfaces reflect contributions from charge transfer across interfaces, as documented by the corresponding frequencies between 10 Hz and 1000 Hz. This is not only associated with lesser resistances for cells operated with coated electrodes, but also with faster transfer rates (at higher frequencies or lower relaxation times). Here, a shift from 2.1 ms (76 Hz) to 0.65 ms (245 Hz) is observable in ***Figure 46b***. Thus, the PEOS coating on Li metal is initially beneficial for charge transfer reactions. The impact of the PEOS coating on the Li deposit morphology is further analyzed by applying a constant current density of 1 mA cm^{-2} for 4 hours while simultaneously monitoring the evolution of ^{7}Li NMR chemical shifts of the Li metal species via *in situ* ^{7}Li NMR spectroscopy.

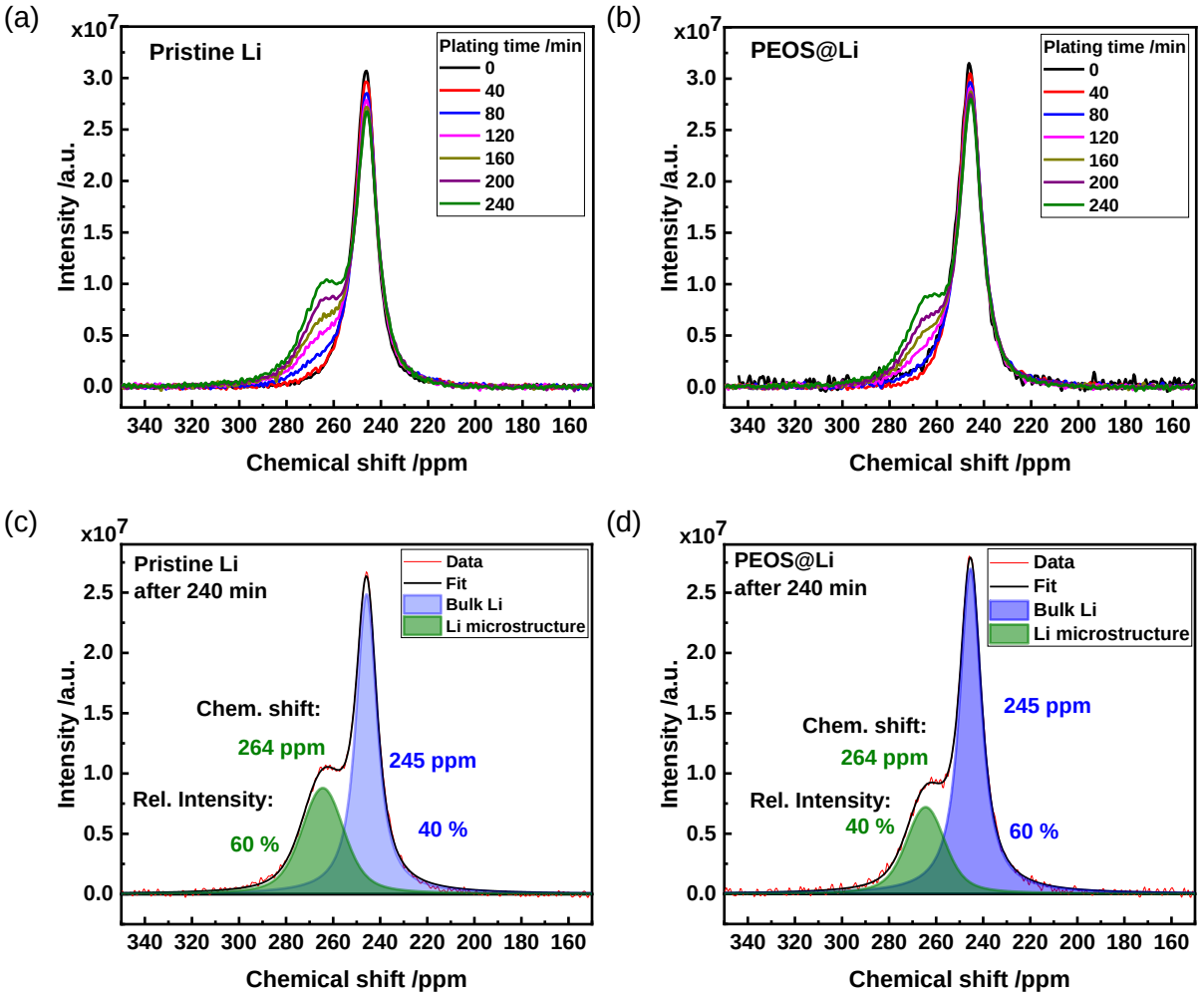

Figure 47: *In situ ^{7}Li NMR spectra of Li||Li cells containing (a) untreated and (b) PEOS-coated Li electrodes and liquid electrolyte LP47. The spectra were devonvoluted by using a custom-made Matlab script and Gauss-Lorentz peaks.*

The chemical shifts of the metallic Li species are correlated with its morphology, based on the bulk magnetic susceptibility effect of the paramagnetic Li metal.[47,82] Initially, a single peak is

visible at 245 ppm for both PEOS-coated and uncoated electrodes, resembling smooth bulk Li metal (***Figure 47a*** and ***b***). Upon continuous plating of Li metal, a shoulder develops at ≈264 ppm, which is characteristic for Li metal deposit microstructures that are 'rougher' than the bulk Li metal (shift of 245 ppm). The chemical shift of this peak is similar for PEOS-coated and uncoated electrodes, which indicates similar morphology towards the end of the experiments. However, the relative intensity of the peaks is lower for the coated electrodes (for example, after 240 minutes, 40 % compared to 60 % for uncoated electrodes, ***Figure 47c*** and ***d***). Even though the NMR spectra are not quantitative due to the thick Li electrodes, the relative difference indicates less occurrence of rough microstructures on the coated electrodes. The voltage profiles as a function of time (***Figure 48a***) show that the coating initially causes a lower overvoltage (at t=0 s), in accordance with the EIS results at OCV in ***Figure 46***. Upon continuous plating, i.e. the passage of constant current, the overvoltage of the cell with coated electrodes increases to a plateau of 0.4 V and slowly decreases until reaching a value of 0.1 V after 160 min. The overvoltage of the cell with uncoated electrodes strongly decreases during the first 10 min, until it reaches a constant value of 0.1 V. The different shapes of the voltage curves can be attributed to the nucleation processes that occur during plating. At the coated electrodes, redox reactions and subsequent plating are partially hindered due to the additional layer, resulting in a characteristic nucleation overvoltage. This effect is not visible with EIS under initial OCV conditions, as no current and low overvoltage amplitudes (10 mV) are applied during EIS. In ***Figure 48b***, the chemical shift of the two contributions from bulk Li and Li microstructures is displayed as a function of time. The peak corresponding to the Li microstructures is not visible during the first 100 min due to the limited detectability of small amounts of deposited Li (< 1 mAh cm^{-2}). The chemical shift of the Li microstructure peaks of both investigated systems becomes increasingly similar, but that of the system with coated electrodes is initially lower. Notably, the break-even point at 175 min, where both systems show similar overvoltage, is visible in both the chemical shift and voltage profile. At this point, the effect of the coating is not observable anymore. In a battery application, this would translate into a maximum plating capacity of 2.9 mAh cm^{-2} until the coating becomes ineffective. The results highlight that, despite the additional resistance (associated with higher overvoltage) of the coating, more homogeneous Li microstructures can be achieved. Nevertheless, further adjustments are required to decrease the overvoltage and reduce loss of charges due to side reactions.

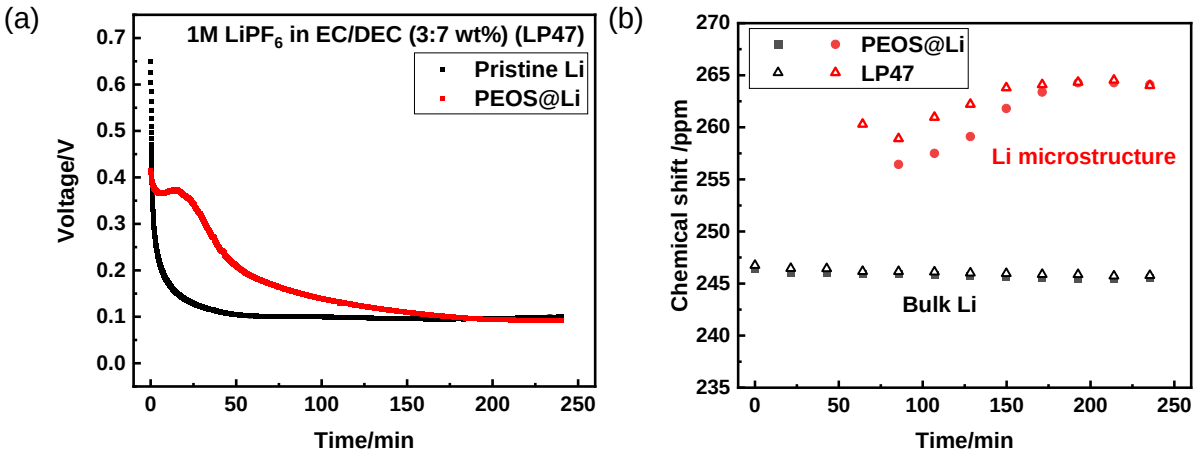

Figure 48: *Overvoltage profile (a) and chemical shift (b) of Li||Li cells containing untreated and PEOS-coated Li electrodes as function of time during plating with a current density of 1 mA cm^{-2}.*

Before further analysis of the coatings, the liquid electrolyte was adapted by an addition of 15 wt% fluoroethylene carbonate (FEC) to the solution while adjusting the EC/DEC composition, in this way yielding electrolyte formulations comprised of 1 M $LiPF_6$ in EC/DEC (1:1 vol.) and 15 wt% FEC. This particular composition was suggested by the project partners, based on the beneficial overall electrochemical cell cycling performance when combined with modified Li metal electrodes. FEC is known to decompose at the Li anode and form rather dense and LiF-rich SEI layers, thereby stabilizing the electrode|electrolyte interphases and adjacent interfacial reactions.[83,84] The actual solvation of Li ions by organic solvents (including FEC) plays a key role in interfacial reactions, and is often not controlled but rather randomly occurring.[85] Here, the coatings are intentionally introduced to govern which kind of solvated Li ion species is participating at interphase reactions. It is hypothesized that the coatings serve as selective de-solvation layers that foster displacement of strongly Li ion coordinating solvents (e.g., EC and DEC) and enrichment of FEC at the interphases, which eventually yield an organic-less but LiF-rich SEI layer. A rigorous combination of multiple analytical tools, including NMR spectroscopy, X-ray photoelectron spectroscopic depth profiling, and cryogenic transmission electron microscopy supports the selective de-solvation effect of the coatings and associated enrichment of LiF in the SEI. Further details about these results go beyond the scope of this thesis and can be found in the publication by Li et al.[56] The cells containing the modified electrolyte and the coated electrodes were analyzed by *in situ* ^{7}Li NMR spectroscopy during charging with a current density of 1 mA cm^{-2} for 4 h. The overvoltage curves are displayed in ***Figure 49a***. Remarkably, the overvoltages of the cells with coated electrodes are relatively low, with 35 mV after 200 min compared to that the reference system (110 mV after 200 min). In contrast to the system with FEC-free electrolyte, the overvoltage curves are smooth and do not show additional nucleation plateaus, demonstrating the beneficial effect of

the coatings in combination with FEC. The relative intensity of the Li microstructure peaks as a function of time corroborates this (***Figure 49b***).

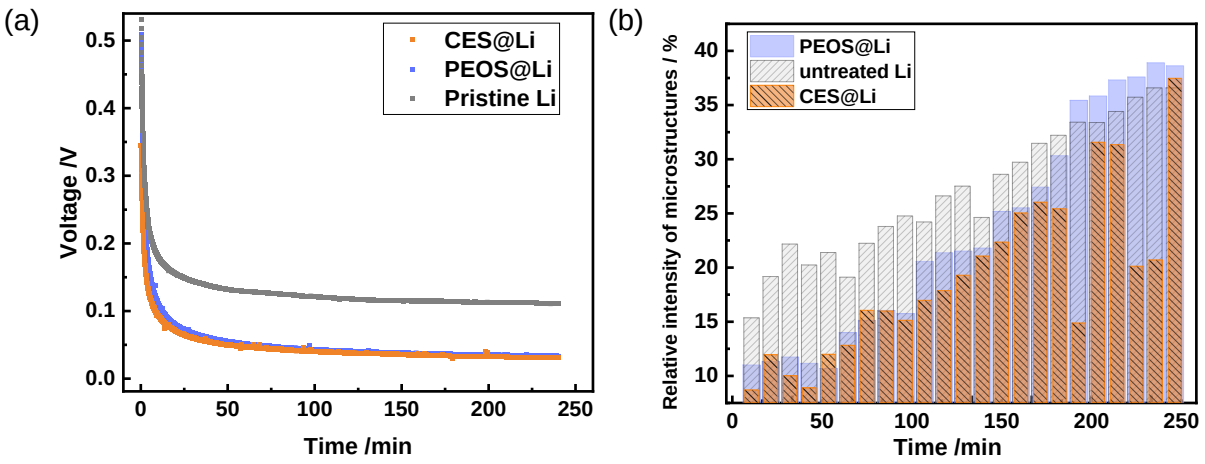

Figure 49: *Overvoltage profile (a) and relative intensity of Li microstructures (b) of Li||Li cells containing untreated and coated Li electrodes as function of time during plating with a current density of 1 mA cm^{-2}. The liquid electrolyte is 1 M $LiPF_6$ in EC/DEC (1:1 vol.) and 15 wt% FEC. Adapted with permission from ref.[56] Copyright © 2024 PNAS.*

The chemical shifts of 260 ppm and 264 ppm (***Figure 50***) after 240 min in the case of untreated and coated Li metal electrodes, respectively, indicate that the Li microstructures are mostly mossy. Interestingly, the chemical shift of the cells with coated electrodes is slightly higher than that with the uncoated electrodes after plating for 240 min, indicating a more perpendicular orientation of the Li deposits relative to the Li electrode. This could be attributed to interfacial reactions that roughen the Li surface to a larger extent compared to the bare Li. Further details of the NMR peak deconvolution are presented in ***Figure A14*** in the Appendix.

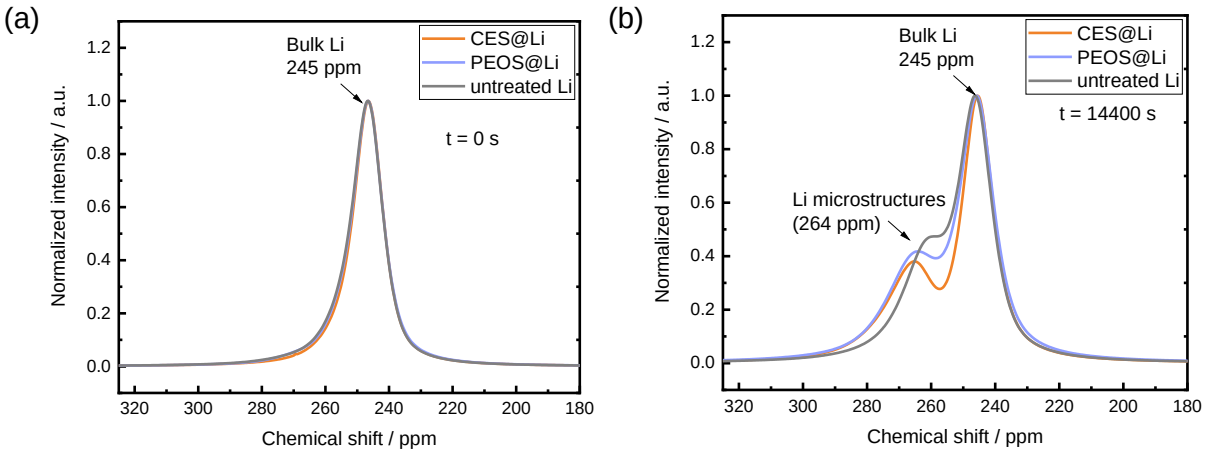

Figure 50: *In situ ^{7}Li NMR spectra of Li||Li cells at (a) t = 0 min and (b) t = 240 min, containing liquid electrolyte 1 M $LiPF_6$ in EC/DEC (1:1 vol.) and 15 wt% FEC and either untreated or coated electrodes. Adapted with permission from ref.[56] Copyright © 2024 PNAS.*

4.2.3 Key achievements of this chapter

In two collaborative works, the changes of Li microstructures upon application of currents were monitored *in situ*, showcasing that homogeneous Li deposition is highly relevant for enabling cycling longevity and faster charging capability.

Li microstructures and cell failure [53]

- By combining DRT and X-ray microtomography, failure modes in Li||Li cells at different current densities could be analyzed.
- At a low current density of 0.1 mA cm^{-2}, large globular Li protrusions form after > 200 cycles that eventually rupture the single-ion conducting polymer electrolyte membrane. Interphase resistance initially decreases due to an increased surface area, which is visible in the DRT plot by decreasing peak heights with no shift in time domain. Upon prolonged cycling, the interphase resistance increases due to formation of additional interphases that exhibit slower charge transfer, as visible in the DRT spectra.
- At a higher current density of 0.3 mA cm^{-2}, mossy Li deposits accumulate comparably fast, resulting in increased SEI formation and electrolyte degradation that govern cell failure before the 30^{th} cycle. The interphase resistance strongly decreases until cell failure due to the substantial growth in microscopic surface area.
- Impurities within the electrolyte and at electrodes are hot-spots for Li nucleation and may eventually cause membrane rupture even at low current densities. Therefore, both electrode and electrolyte purity are relevant parameters for cell longevity.

Li microstructures on modified Li electrodes [56]

- Beneficial effects of Si-based polymeric interphases (CES and PEOS) on the reversibility of Li metal deposits could be demonstrated with *in situ* ^{7}Li NMR spectroscopy and constant current plating.
- Cells containing liquid electrolyte and PEOS-modified Li electrodes exhibit lower initial interphase resistances compared to cells with untreated Li electrodes. However, the overvoltage curves show that upon cell operation, the polymer coatings cause additional overvoltage likely associated to Li nucleation processes.
- In cells with a modified liquid electrolyte that contains 15 % FEC, both CES and PEOS exhibit lower overvoltage and ^{7}Li NMR spectroscopy reveals fewer relative amounts of microstructures on the coated electrodes.
- The results corroborate beneficial impact of polymer coatings on cell longevity, which selectively de-solvate electrolyte constituents that are beneficial for forming inorganic-rich SEI layers.

4.3 Li/polymer interface kinetics

Aside from EIS, charge transfer from the electrolyte to the electrode and vice-versa can be monitored with voltammetry. Since the charge transfer rate may eventually limit the charging capability of an electrode, its quantification is highly relevant for the tailored development of advanced active materials for electrodes and electrolytes. The interfacial charge transfer between the electrolyte and the electrodes is often modeled with the Butler-Volmer current-voltage relation.[11] However, the complex deposition and dissolution phenomena on Li metal electrodes require advanced models, such as the Marcus-Hush model of charge transfer.[86–88] Boyle et al. demonstrated the applicability of the Marcus-Hush model experimentally by conducting fast voltammetry at microelectrodes, where various liquid electrolytes were characterized based on their characteristic exchange current density and reorganization energy.[13] In this chapter, custom-made tungsten microelectrodes are presented that are able to capture Li deposition and dissolution phenomena at comparable fast sweep rates (>1 Vs^{-1}), thereby inhibiting side reactions that eventually result in an SEI. In contrast to cells from previous works[13], the developed microelectrodes are compatible with cells that can incorporate both liquid and solid polymer electrolytes.

4.3.1 Development of the micro electrode

The first versions of the micro electrodes were tested with liquid electrolyte LP47 and showed oscillation patterns at scan rates of 10 V s^{-1} and 30 V s^{-1} (***Figure 51***). Upon closer inspection, the distances between the oscillation maxima can be converted into a characteristic frequency by dividing the scan rate (in V s^{-1}) by the difference of the maxima (in V).

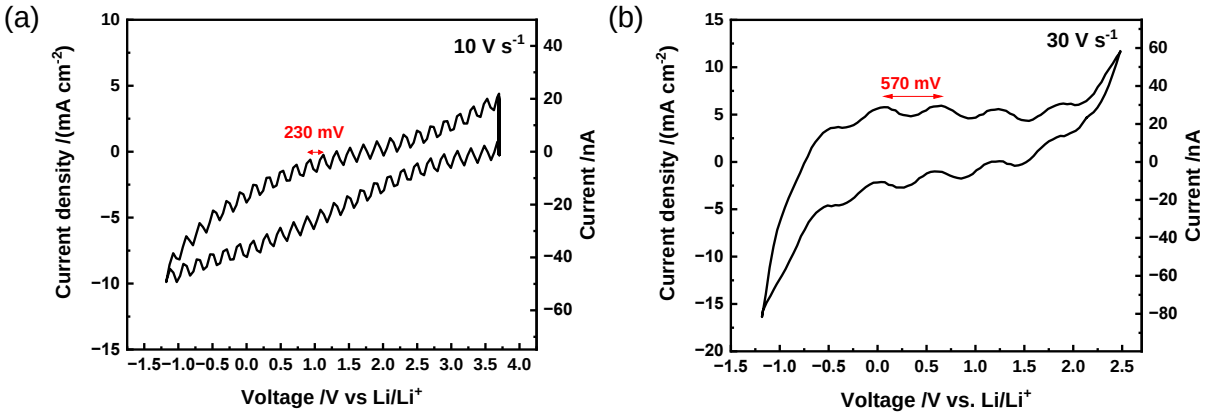

Figure 51: *Cyclovoltammograms of the micro electrodes with liquid electrolyte LP47 at 20 °C at scan rates of (a) 10 V s^{-1} and (b) 30 V s^{-1}. The voltage at the micro electrode was measured against a Li/Li^+ reference electrode in a Swagelok-type set-up on a lab bench.*

The resulting frequencies are 43 Hz and 53 Hz at 10 V s^{-1} and 30 V s^{-1}, respectively, and thus likely result from external electromagnetic fields (e.g., alternating current from the electric grid). Since the current amplitudes are in the range of tens of nanoamperes, the impact of

electromagnetic fields on the measured signal is particularly strong. Also, the expected Li plating and stripping peaks could not be observed, indicating that the intended electrochemical reactions do not occur. As a countermeasure, the microelectrodes were electrochemically cleaned by galvanostatic cycling between 0 V and 1 V at a constant current of 5 nA (1 mA cm^{-2}) prior to performing the cyclovoltammetry experiments. The oscillating noise was partially suppressed by placing the cells in an oven during the measurements (***Figure 52***).

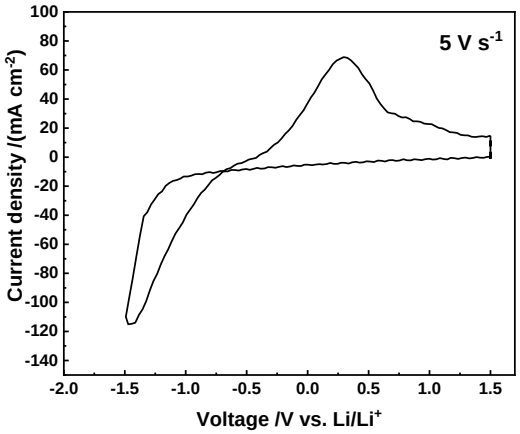

Figure 52: *Cyclovoltammogram of the micro electrodes with liquid electrolyte LP47 at 20 °C at a scan rates 5 V* s^{-1}.

A clear oxidation peak is visible at positive currents, representing the stripping (dissolution) of Li metal from the electrode. At negative currents, a Li plating peak is visible, though it is substantially deformed, which is indicative of irreversible processes and non-ideal reactions associated with a nucleation of Li onto the tungsten electrode. Similar Li plating and stripping peaks could be observed by Boyle et al.[13] The potential at no applied current should ideally be close to 0 V vs. Li/Li^+, since the measurement is performed against a Li reference. However, at zero current, the potential is in this case -0.4 V vs. Li/Li^+, indicating a mismatch between the reference system and the working electrode in terms of redox potentials. This could be due to the tungsten microelectrode which serves as nucleation site, whereas the reference electrode is a pure Li foil. In the next chapter, the voltage is measured in a two-electrode set-up, which yielded more reproducible results.

4.3.2 Cyclovoltammetry with a solid polymer electrolyte

The solid polymer electrolyte xGCD-PCL was invoked as exemplary polymer electrolyte that can be operated at 40 °C. When using macroelectrodes (***Figure 53a***), the shape of the cyclovoltammogram is unexpected and even at scan rates of 10 mV s^{-1}, the peaks for oxidation and reduction are not clearly resolved. Here, the applied voltage changes faster than the electrodes can establish defined electrode potentials. At a scan rate of 100 mV s^{-1}, the cell behaves like a resistor, since no defined potentials can be established during the measurement

time. In contrast, the microelectrode can be operated at the faster scan rates of 100 mVs^{-1} and 1 Vs^{-1} and clearly shows the expected plating and stripping peaks.

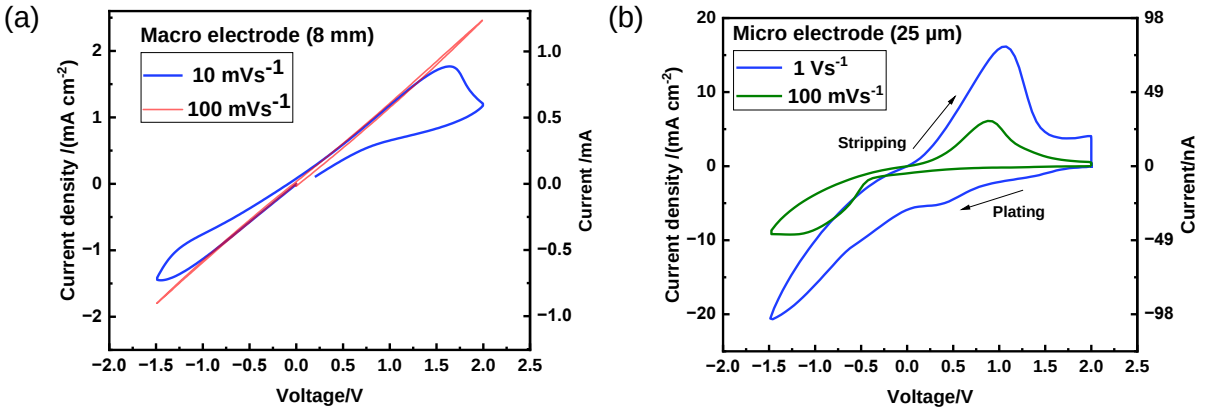

Figure 53: *Cyclovoltammogram of the polymer electrolyte xGCD-PCL at 40 °C with the working electrode being (a) a macroelectrode (0.5 cm²) and (b) microelectrode (4.9 x 10^{-6} cm²).*

To analyze the charge transfer kinetics, only the region of small overpotentials is considered. The voltage axis is normalized to the voltage measured at zero current, so that it can be considered as quasi equilibrium potential. On a logarithmic scale, the data points can be fitted according to a Marcus-Hush type model, whereas the Butler-Volmer model of charge transfer does not yield satisfactory fitting results (***Figure 54***).

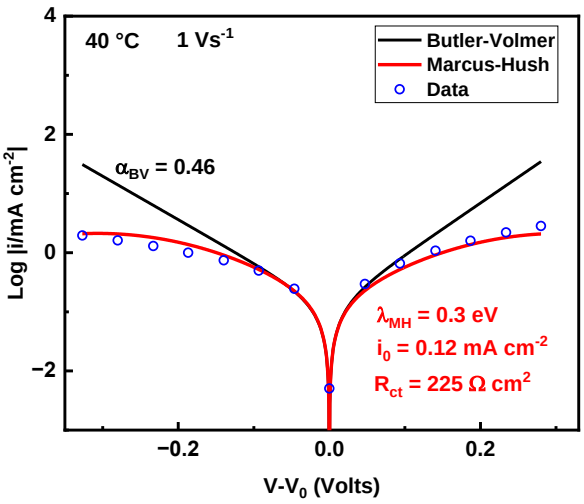

Figure 54: *Tafel plot of the small overvoltage region and corresponding Marcus-Hush and Butler-Volmer type model fits.*

The fit parameters of the Marcus-Hush type model include an exchange current density of 0.12 mA cm^{-2} and a reorganization energy of 0.3 eV. Compared to liquid electrolytes, the exchange current density is rather low. For example, $LiPF_6$ in EC/DEC has an exchange current density of 10.4 mA cm^{-2}.[13] Thus, polymer electrolytes not only exhibit slower bulk ionic charge transport, but also slower interfacial charge transfer reactions. A reorganization energy

of 0.3 eV is comparable to that of common liquid electrolyte systems. Notably, no solvents are present in the polymer electrolyte. Instead, the polymer chains seem to take the role of a solvent not only in bulk, but also close to the electrode.

4.3.3 Key achievements of this chapter

The charge transfer kinetics of Li deposition and dissolution was characterized with fast cyclovoltammetry invoking microelectrodes.

- A custom-made tungsten microelectrode was fabricated with an electrode area of 4.9 x 10^{-6} cm^2 that could be implemented into Swagelok-type cells.
- Li plating and stripping at the tungsten microelectrode was possible, as confirmed by cyclic voltammetry experiments.
- Similar to liquid electrolytes, the charge transfer kinetics at the Li|polymer interfaces can be modeled based on the Marcus-Hush theory of charge transfer, which considers the reorganization of solvent molecules upon redox reactions.
- The reorganization energy of 0.3 eV is comparable to that of liquid electrolytes, while an exchange current density of < 0.5 mA cm^{-2} is rather small, similar to the limited bulk ion transport properties of polymers.

4.4 From lab to industry: Projections of energy density

After exploring dynamic changes of Li metal deposit microstructures and associated kinetics of interfacial charge transfer, the following section introduces the achievable projected energy densities of larger cells, predicted in case of single- or multi-layered cells. With that, target values of energy density and specific energy are proposed and compared to available competing technologies. A key goal of this section is to propose possibilities to analyze the potential of early-stage cell chemistries more conveniently and to demonstrate present limitations of polymer-based Li metal batteries. Note that parts of this section were already published:[3,25]

- G. Brunklaus, P. Lennartz, M. Winter: Metal electrodes for next-generation re-chargeable batteries, *Nature Reviews Electrical Engineering*, **2024**, https://doi.org/ 10.1038/s44287-023-00006-5.

- P. Lennartz, B. A. Paren, A. Herzog-Arbeitman, X. C. Chen, J. A. Johnson, M. Winter, Y. Shao-Horn, G. Brunklaus: Practical considerations for enabling Li|polymer electrolyte batteries, *Joule*, 7, 1-25, **2023**, https://doi.org/10.1016/ j.joule.2023.06.006.

4.4.1 The long road to next generation batteries

Stages for the development of next-generation batteries range from early academic proof-of-concept explorations to actual assembly of demonstrator cells and broader-scale applications (***Figure 55***). Here, the Technology Readiness Level (TRL) that was originally introduced by the National Aeronautics and Space Administration (NASA) in 1989, provides a meaningful measure for evaluating technological maturity of the potential products.[89] This metric was employed in 2022 to shape the Battery 2030 roadmap for the battery research in Europe.[90] Indeed, a related roadmap, the "Battery Component Readiness Level," specifically outlines the progression of battery technological advancements, encompassing fundamental research and lab-scale prototypes to up-scaled systems and commercialization.[91] This involves a series of steps, spanning from fundamental materials research and identification of suitable anodes, cathodes or electrolytes, to showcasing cell chemistries through prototype applications. Once viable active components are established, the focus typically shifts to realizing appropriate cell designs that emphasize thinner and denser layers to yield enhanced energy densities of the cells. Also, cost-efficient scalability of actual cell systems with respect to materials availability or synthesis, manufacture as well as operational cell safety considerations become crucial. Finally, approved prototype cells are transferred to actual application scenarios and introduced to the market. Much of the research related to batteries concerns the exploration of novel materials and methods on a fundamental level and developing cell design strategies from these materials, thus being on TRLs of 1 to 3. Therefore, it is even more important to find means of evaluating promising material's potential for future application in larger batteries.

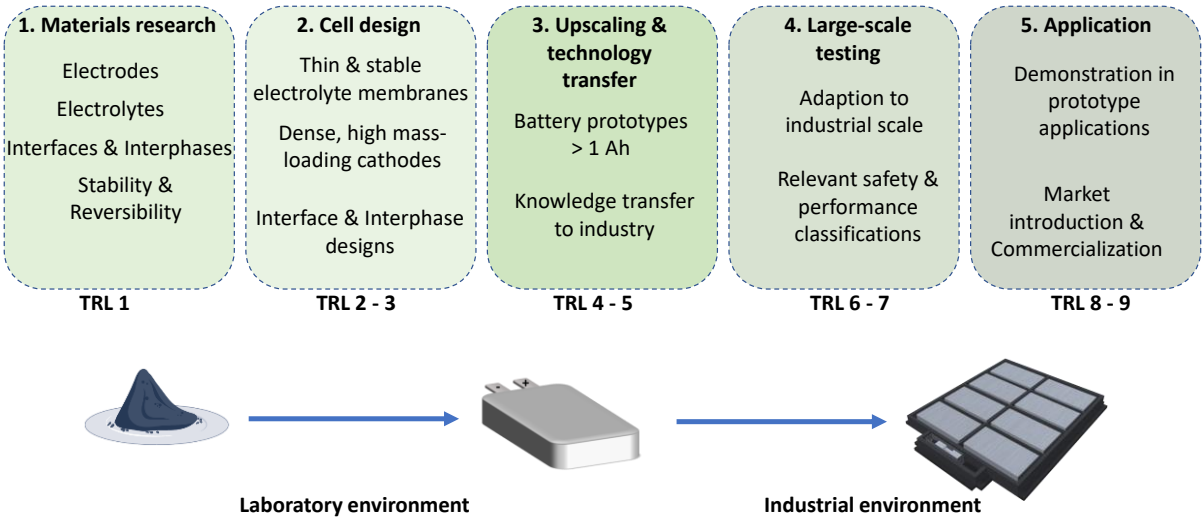

Figure 55: *Overview of the different stages involving the development of battery technologies, ranging from materials research to large scale applications. A technology readiness level (TRL) is indicated for better comparability with research areas outside the scope of batteries. Adapted from ref.[3]*

In the academic literature, the cycling performance of experimental cells is typically presented as specific capacity (in mAh g^{-1}) vs. the cycle number. While such notation provides a basis to evaluate how much of available theoretical capacity provided by cathodes may be accessed experimentally, it does not give an indication of the practical relevance of the cells for battery applications. For example, cells with $LiFePO_4$ cathodes with lower mass loadings (e.g. 2 mg cm^{-2}) likely perform excellent in terms of cell longevity and exploitation of the material's theoretical limit, but the amount of energy stored in these cells is below what is feasible for industrial use. Critical parameters such as cathode active mass loading and average operating voltage often vary substantially between different cell chemistries, thereby rendering direct comparison of reported cell data challenging. In an attempt to achieve better comparability of different cell chemistries presented in available literature and to identify promising active materials, the average energy per cycle and electrode area is introduced, as a reliable indicator for the amount of reversibly achievable energy.[25] This metric combines achievable capacities with corresponding average voltages and thus gives a good indication of the amounts of energy that can be stored per electrode area. Note that this metric is not comparable to an energy density, but is normalized to the electrode area, as most data available from literature does not include sufficient information to calculate total volume or mass of the cells. ***Figure 56*** visualizes how various systems with polymer-based electrolytes perform in comparison to solid-state inorganic electrolytes and liquid electrolytes. The majority of polymer-based cells are operated at average area specific energies <2 mWh cm^{-2} and comparably low cathode mass loadings ranging from 1 to 3 mg cm^{-2}. Here, Tesla's liquid electrolyte cycled in LFP||C Li ion batteries sets an impressive benchmark with 8.9 mWh cm^{-2} and cathode mass loadings of 21.5 mg cm^{-2}, despite that LFP is operated at lower average voltage than NMC-type cathodes.[92] Another impressive value was achieved with inorganic solid-state electrolytes (argyrodites) applied in NMC811||µSi cells.[93] In this case, the high ionic conductivity of the argyrodite enables fast-charge relevant current densities of up to 5 mA cm^{-2} (1C) at room temperature and cathode mass loadings of 25 mg cm^{-2}. However, cycling of the cells was only possible under substantial external pressure (50 MPa, or 500 bar), which is not realistic to maintain in larger cells or even battery packs. The required pressing force scales with the cell area and thus would necessitate heavy steel plates, thereby diminishing the advantage of energy density and specific energy.[25] The best performing polymer electrolyte-based cells contain flowable components, either as oligomers or ionic liquids that enable mass loadings > 6 mg cm^{-2} and area specific energies of > 3.5 mWh cm^{-2}.

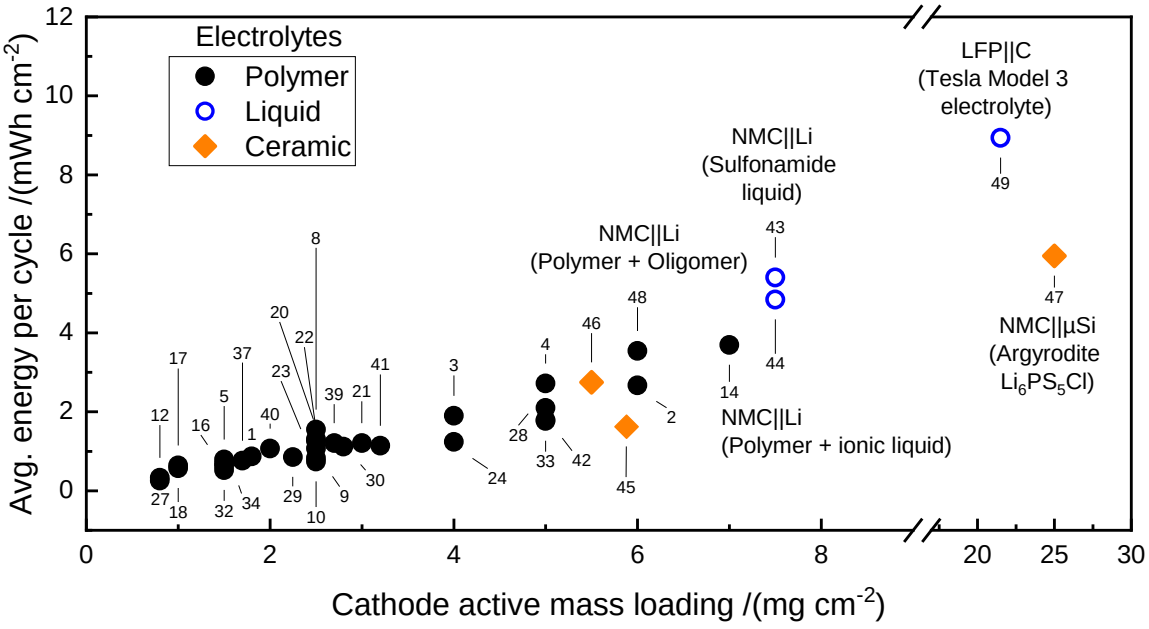

***Figure 56**: Average energy released per cycle vs. cathode active mass loading for several examples from recent literature (see also Lennartz et al.[25]). The indices correspond to the references listed in Table A2 in the Appendix. Labeled data points are representative highlights and correspond to the following references: Index 14: Wu et al.[94]; index 43: Xue et al.[95]; index 47: Tan et al.[93]; index 48: Chen et al.[61]; index 49: Stock et al.[92]*

To better understand why polymer electrolytes are mainly operated with comparably low mass loadings of cathodes, a simple density plot of required current densities is presented in ***Figure 57***.

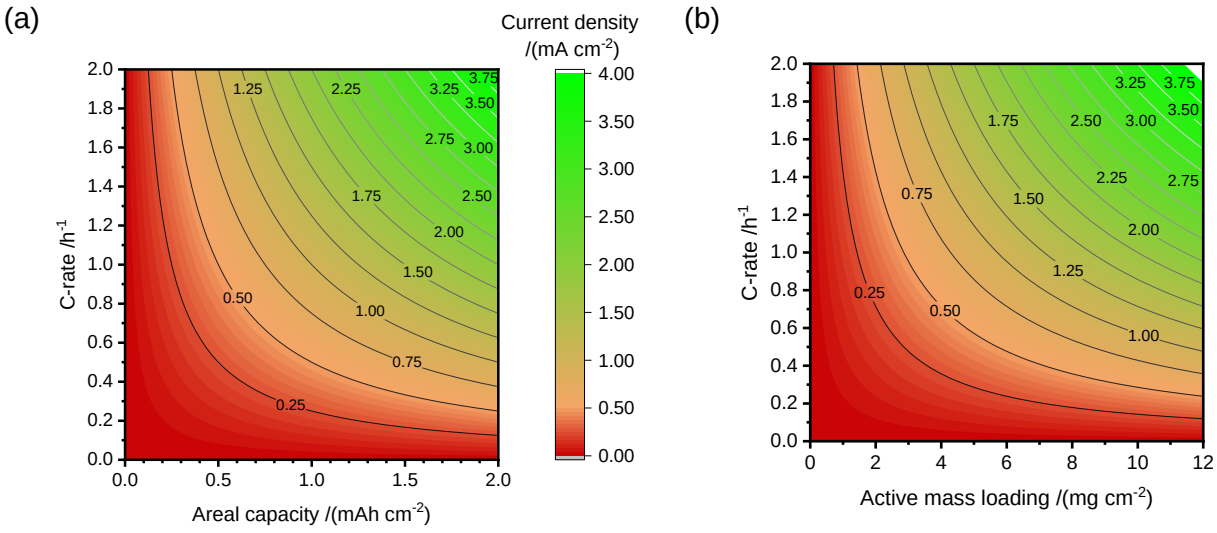

***Figure 57:** Current densities required to charge a battery at different C-rates with (a) varying cathode areal capacities and (b) varying active mass loadings. The active mass loadings are determined for an available specific capacity of 175 mAh g^{-1}in case of NMC622 cathodes.*

In case of cathodes with areal capacity of 1 mAh cm^{-2} (e.g., 6 mg_{NMC} cm^{-2}), a current density of 1 mA cm^{-2} is required to charge the corresponding battery at a rate of 1 C. Increasing the cathode mass loading to 12 mg_{NMC} cm^{-2} or 2 mAh cm^{-2}, the current density required for 1 C consequently doubles to 2 mA cm^{-2}. The limiting current density of polymer electrolytes, however, is often well below 1 mA cm^{-2}, thus excluding faster charging rates of up to 1 C when operating cathodes with areal capacities higher than 1 mAh cm^{-2}. This calculation demonstrates that for polymer electrolytes to be implemented in applications with faster charging rates (e.g., electric vehicles), limiting current densities must be increased. The limiting current density depends, according to Newman and Balsara, on various parameters, including diffusivity, charge carrier concentration, transference number and thickness of the electrolyte membranes.[12] Therefore, higher limiting current densities could only be achieved by boosting diffusivity (or conductivity), the salt concentration, cation transference number, or by decreasing electrolyte thickness.

4.4.2 A closer look: Energy density and specific energy

Specific energy and energy density strongly depend on the considered battery level, which can range from individual cells to battery packs (a complete battery unit to power electric vehicles). For example, the battery unit of the Volkswagen ID.3 (***Figure 58***) provides an energy density of 266 Wh L^{-1} at pack level, while the energy density at cell level is more than 2.5-fold higher (685 Wh L^{-1}).

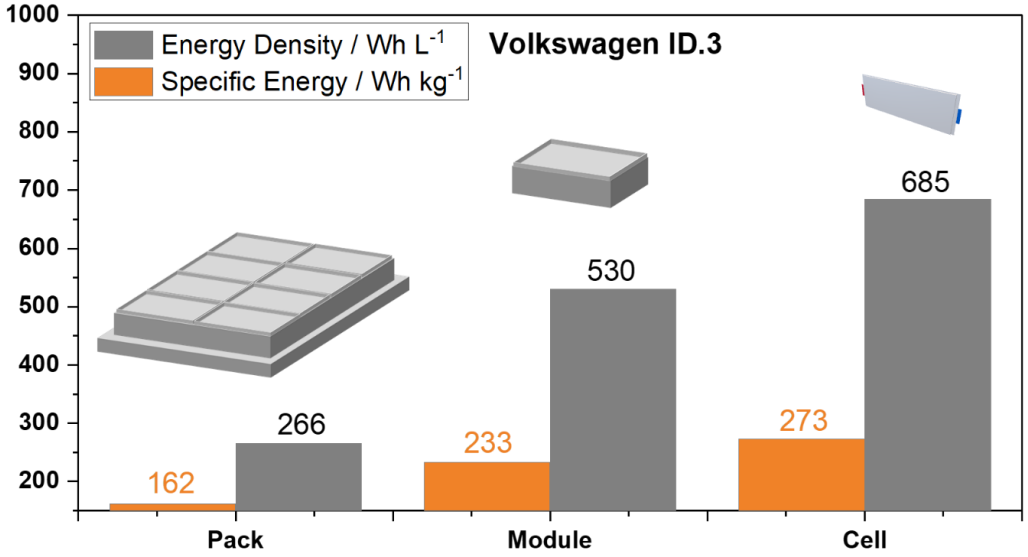

Figure 58*: Energy density and specific energy at different battery levels (battery pack, module and cell) for the example of a Volkswagen ID.3. Values based on Wassiliadis et al.*[96]

The losses in energy density and specific energy can be explained by the presence of additional electrochemically inactive components, such as module and pack housing, cooling elements or elements of the battery management system.[96] Note that volumetric losses are

more pronounced than gravimetric losses due to spacious components, emphasizing the importance of realizing high energy densities already at cell level. As part of this thesis, an interactive tool called ProSpecDense was developed to reliably project energy densities of considered batteries, explicitly motivated from discrepancies of laboratory results and key benchmarks presented by industrial cell manufactures. Existing tools, such as BatPac[97] or SolidPac[98] also enable projection of cell chemistries from battery modules and packs, but they require more input parameters, rendering their exploitation time consuming. The major advantage of ProSpecDense comprises the intuitive and dynamic graphical user interface, while at the same time allowing for extensive variation of relevant cell parameters through sliders and input fields. An early version based on Microsoft Excel was first released as part of a collaborative review published in *Joule*.[25] An advanced version of the tool was programmed in Python language and distributed as downloadable executable file.

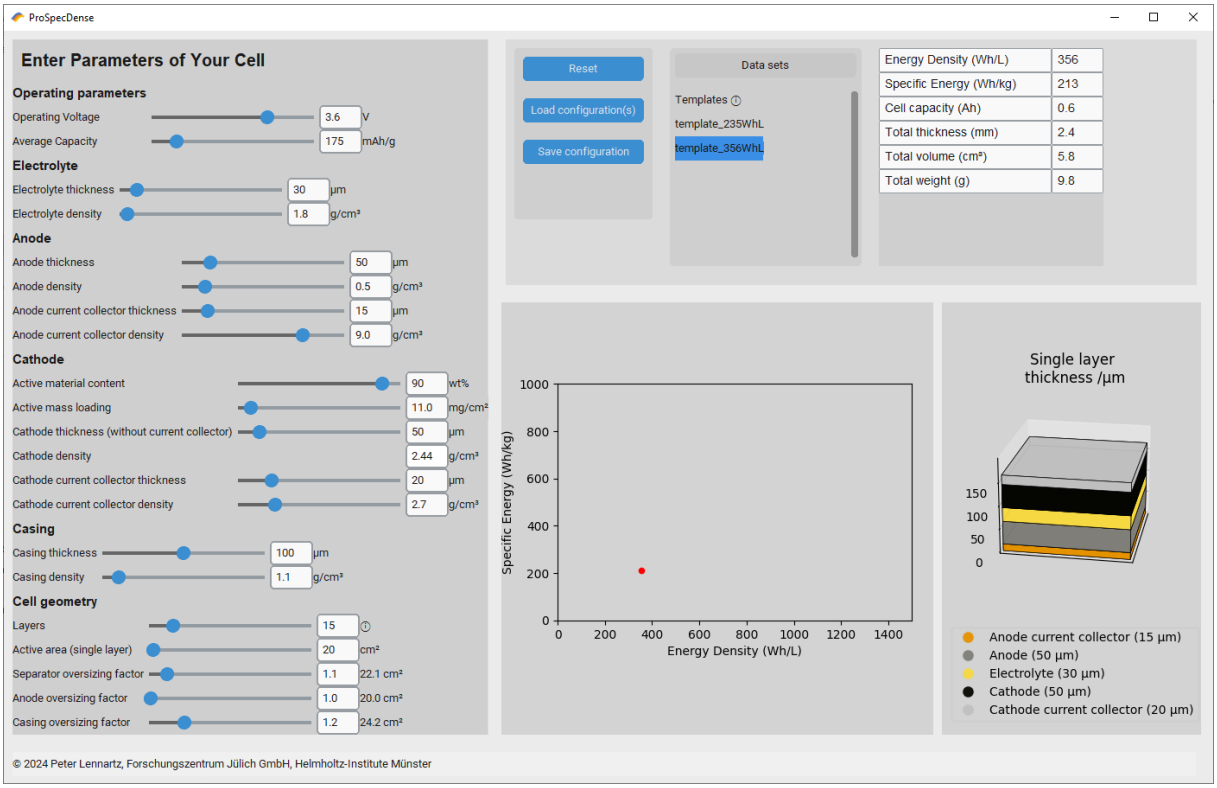

***Figure 59**: Graphical user interface of the python-based program ProSpecDense for the projection of energy density and specific energy.*

The intuitive graphical user interface (***Figure 59***) includes controls on the left panel and graphical presentation on the right panel, as well as an import and results section at the top. The input parameters to describe the investigated cell systems are divided into six categories: *Operating parameters*, *Electrolyte*, *Anode*, *Cathode*, *Casing*, and *Cell geometry*. Each of the parameters is either experimentally accessible or straightforwardly derived. The central plot window presents the projected specific energy vs. energy density and updates dynamically, thereby yielding valuable feedback to the user. A configuration of the relevant parameters can

be saved and reloaded simply by clicking on the respective buttons. Once loaded, the user can switch between different configurations by selecting them from the *Data sets* list. The graphic on the right visualizes a single layer of the model system with thicknesses of the individual layers in µm.

To obtain an impression of the impact of individual parameters on energy density and specific energy, in a first step, a single parameter is varied at a time. For that, an actual cell system that was published previously (consisting of a thin polymer electrolyte (30 µm), Li metal anode (50 µm), and NMC622 cathode (11 mg cm^{-2}, 90 wt% CAM, 50 µm))[61] serves as reference system. Further input data of this system is provided in the Appendix (***Table A1***). The most prominent boost in both energy density and specific energy can be achieved when increasing the cathode active mass loading (***Figure 60a***).

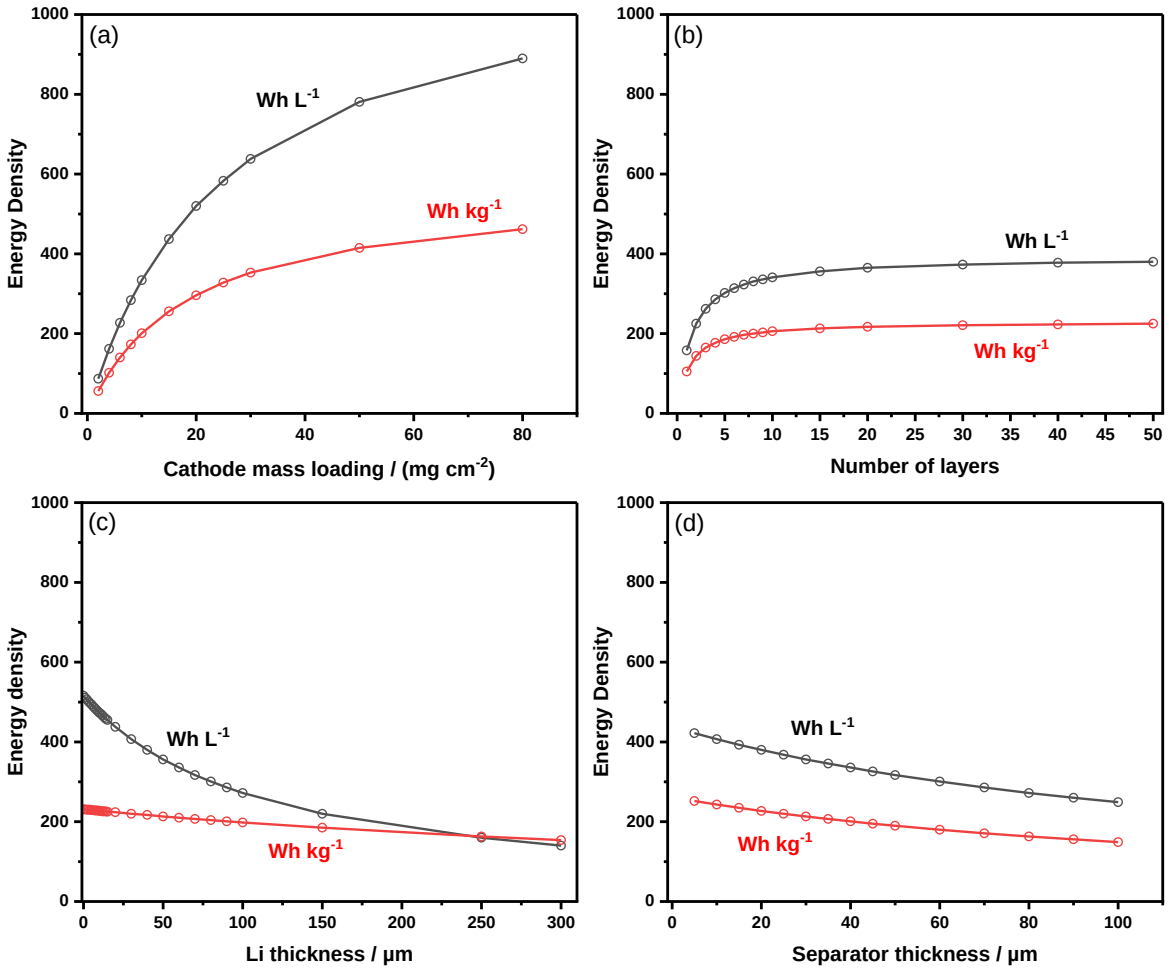

Figure 60: *Energy density (Wh L^{-1}) and specific energy (Wh kg^{-1}) as function of (a) cathode active mass loading, (b) number of layers, (c) Li thickness and (d) separator thickness. All data points were calculated with the custom-made ProSpecDense software.*

Doubling the active mass loading from 4 mg cm^{-2} to 8 mg cm^{-2} increases the energy density from 162 Wh L^{-1} to 284 Wh L^{-1} (increase of 75 %) and the specific energy from 102 Wh kg^{-1} to

173 Wh kg^{-1} (increase of 70 %). Note that the cathode density was kept constant, such that increasing the cathode active mass loading simultaneously results in thicker cathode layers. An industrially favorable mass loading of 20 mg cm^{-2} results in 520 Wh L^{-1} and 296 Wh kg^{-1}, though practical challenges such as charge transport within thick cathodes (90 µm) currently prevent realization of such high mass loadings in the case of solid systems (where no liquid electrolyte fills the pores of the cathode).[25] A higher number of layers is increasingly less effective at larger layer numbers (***Figure 60b***), attributed to the ratio of the weight and volume of the casing relative to the overall weight and volume of the cells (see also Eq. (36) and Eq. (37) in the Experimental section). Consequently, the energy density and specific energy of a multi-layer cell with a large number of layers are similar to those of a single-layer cell without casing. This is particularly helpful for an estimation of energy densities and specific energies in cases where weight and volume of the casing are not known. Reducing the excess Li layer thickness to a minimum is desirable in terms of energy density (***Figure 60c***). In the considered cell set-up, the cathode is initially fully lithiated, so that all of the Li at the anode is excess Li that serves as reservoir to account for active material losses through interphase formation.[15] The impact of Li thickness is especially high with respect to energy per volume rather than energy per mass, reflecting the low density of Li compared to other components (0.53 g cm^{-3}), that results in less changes in mass upon increasing or decreasing the Li thickness. Reducing the Li foil thickness from 50 µm to 20 µm yields an increase in energy density and specific energy from 356 Wh L^{-1} to 438 Wh L^{-1} (23 % increase) and 213 Wh kg^{-1} to 224 Wh kg^{-1} (5 % increase), whereas fully omitting initial excess Li foil yields a favorable energy density and specific energy of 516 Wh L^{-1} and 231 Wh kg^{-1}. Thinner electrolyte layers (***Figure 60d***) are also good for boosting achievable energy density and specific energy of the cells, though the effect is less pronounced than in case of Li metal due to a higher density of the electrolyte (1.8 g cm^{-3}) and fixed Li thickness of 50 µm.[61]

As a next step, more than one parameter is changed simultaneously to identify target values and compare projected energy densities and specific energies with commercial battery manufacturers.[25] In ***Table 6***, the input parameters for a model cell are presented and changes of individual parameters are indicated in bold letters in the respective columns. The model cell is operated at an average voltage of 3.5 V and delivers a specific discharge capacity of 175 mAh g^{-1}, a value that is common for Ni-rich cathodes such as NMC811 in combination with polymer electrolytes.[99]

Table 6: *Model parameters used for the projection of energy density and specific energy of cells. Differences compared to the single-layer model cells are in bold, as well as resulting values for capacity, specific energy and energy density.*

	Model cell	Projection I	Projection II	Projection III
Operating Voltage /V	3.5	3.5	3.5	3.5
Average capacity /(mAh g^{-1})	175	175	175	**200**
Electrolyte thickness /µm	50	50	**25**	**25**
Electrolyte density /(g cm^{-3})	1.5	1.5	1.5	1.5
Lithium thickness /µm	50	50	**20**	**20**
Cathode thickness /µm	65	65	**186**	**100**
Cath. active material cont. /wt%	60	60	60	**90**
Active mass loading /(mg cm^{-2})	7	7	**20**	**25**
Number of layers	1	**15**	**15**	**15**
Anode current collector thickness (Copper) /µm	10	10	10	10
Cathode current collector (Aluminum) thickness /µm	20	20	20	20
Casing thickness /µm	100	100	100	100
Casing area /cm^2	24	24	24	24
Current collector area /cm^2	22	22	22	22
Anode and cathode area /cm^2	20	20	20	20
Cell capacity /Ah	**0.025**	**0.4**	**1.1**	**1.5**
Specific energy /(Wh kg^{-1})	**68**	**135**	**256**	**413**
Energy density /(Wh L^{-1})	**90**	**184**	**392**	**837**

The resulting specific energies and energy densities are visualized in ***Figure 61***. The electrolyte and Li thickness of 50 µm are currently state-of-the-art for solid-state batteries.[61] The cathode is composed of 60 wt% active material at a mass loading of 7 mg cm^{-2}. Polymer electrolyte (catholyte) is added to the cathode to facilitate charge transport. The cell capacity of a single-layer model cell is comparably low with 25 mAh, corresponding to areal capacity of 1.25 mAh cm^{-2}. Consequently, the specific energy and energy density are low as well with 68 Wh kg^{-1} and 90 Wh L^{-1}, respectively. In projection I, the single layer of cathode, electrolyte and anode is stacked to a total of 15 layers, resulting in 0.4 Ah cells with energy density of 184 Wh L^{-1} and a specific energy of 135 Wh kg^{-1}. In another step, the electrolyte thickness is reduced to 25 µm (comparable to separators used for liquid electrolytes[36]), the Li thickness is limited to 20 µm, and cathode thickness is increased to 186 µm (corresponding to an active mass loading of 20 mg cm^{-2}). In this way, projection II yields values of 256 Wh kg^{-1} and 392 Wh L^{-1}, which are comparable to that of *BlueSolutions' Generation 3* solid polymer-based Li metal battery.[100] To be competitive with the hybrid (and often not fully dry) cell concepts of

QuantumScape, *SES* and others, the active mass loading is further increased to 25 mg cm^{-2}, and the cathode thickness is decreased to 100 µm, thus assuming densely packed cathodes with an active material content of 90 wt%. Projected values of 413 Wh kg^{-1} and 837 Wh L^{-1} exceed the USABC target value of 350 Wh kg^{-1}, but require advanced dry cathode engineering, as current cathode concepts do not reach such high mass-loadings without liquid additives (catholytes).

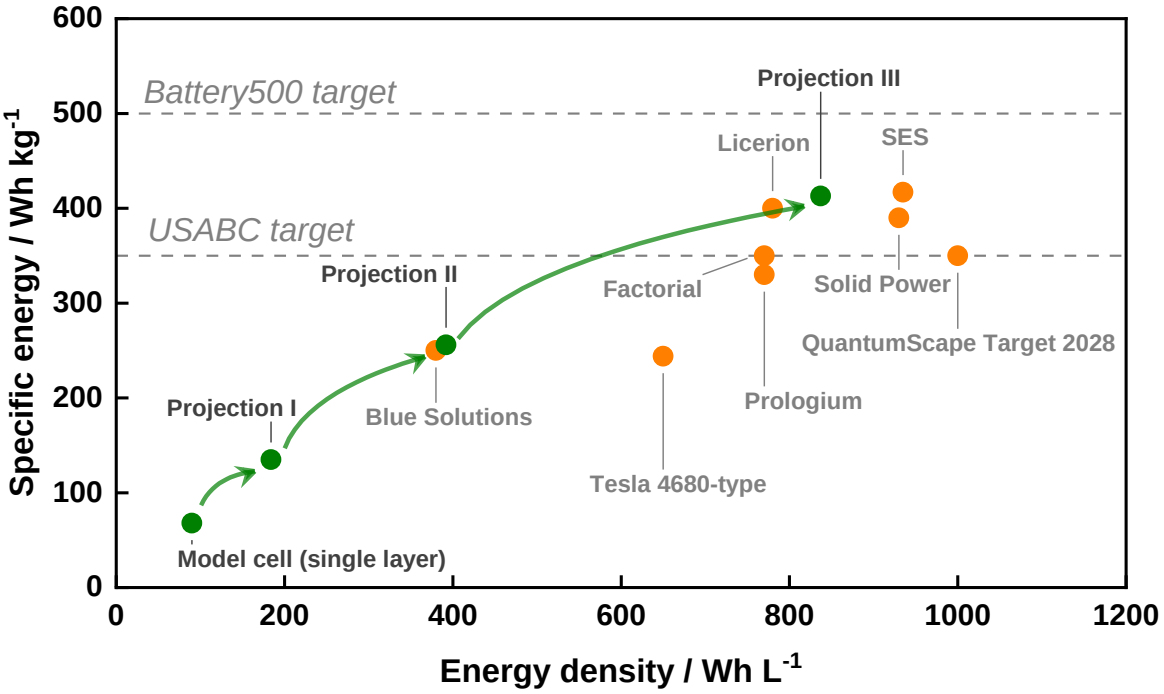

***Figure 61**: Energy density and specific energy of a projected model pouch cell from single-layer to multiple layers. Target values for commercial manufacturers are collected from the following references: Blue Solutions[100], Tesla[101], Licerion[102], QuantumScape[103], Solid Power[104], SES[105], Prologium[106], Factorial[107]. Reprinted with permission from ref.[25] Copyright © 2024 Joule Cell Press.*

Once a cell chemistry has proven to be promising in small-scale coin cells and could be projected towards competitive energy densities, the next step is to build larger cells. By increasing the electrode area and stacking of multiple layers, higher cell capacities can be achieved. Cell capacities around 1 Ah are common to exploit developed cell chemistries in application-oriented scenarios.[21] Cells that provide such capacity usually have single electrode areas of tens of cm^2 (e.g. 4 cm x 10 cm per layer) and contain multiple layers (e.g. 15), so that any volume changes during cycling, as well as the amounts of active material within the cells, are substantially larger compared to academic single-layer cells. This approach enables a more realistic assessment of both cell performance and safety.[108] Since the total active area ultimately determines the cell capacity for a given active mass loading

(areal capacity), both the number of layers and active area of individual layers are relevant parameters in this regard. Larger electrode areas increase the risk of defects and exacerbate electrode handling, while more layers increase the risk of misalignment between the different sheets. To identify a compromise between adding more layers and increasing electrode areas, two cases are visualized in ***Figure 62a*** and ***b***. At a comparably low cathode areal capacity of 1 mAh cm^{-2}, single electrode areas of >20 cm^2 are required when using less than 50 layers to achieve a capacity of 1 Ah. A good compromise would be 32 layers at electrode areas of 32 cm^2, assuming that both increasing electrode areas and adding additional layers is equally challenging. At a cathode areal capacity of 2 mAh cm^{-2}, 15 layers with an electrode area of 34 cm^2 are already sufficient for a 1 Ah cell.

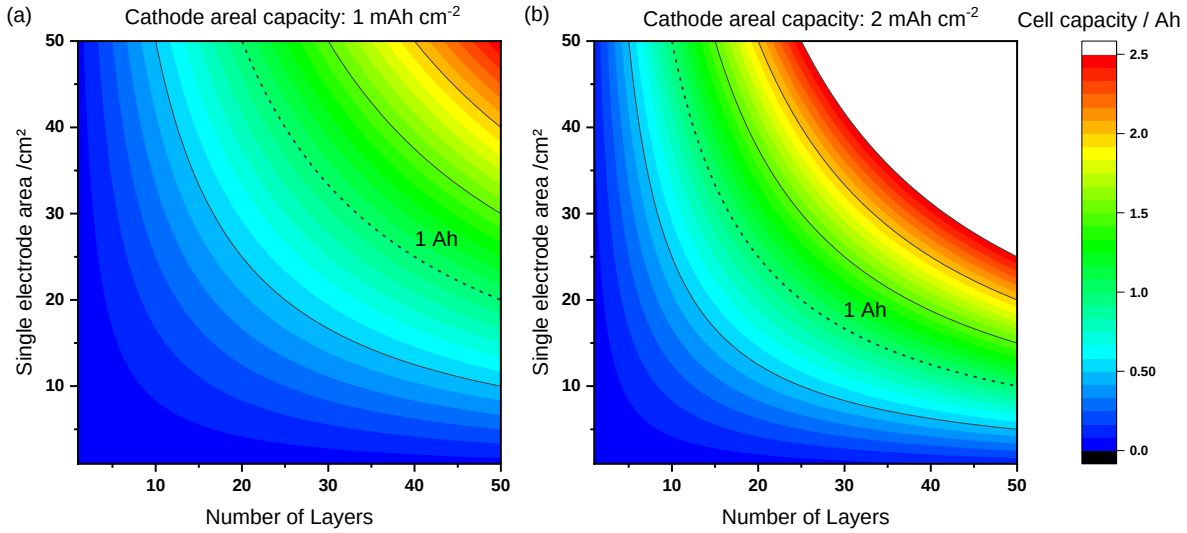

Figure 62*: Contour plots of the cell capacity as a function of single electrode area and number of layers utilizing cathode areal capacities of (a) 1 mAh cm^{-2} and (b) 2 mAh cm^{-2}. The lines represent equal capacity, the dotted lines indicate a cell capacity of 1 Ah.*

4.4.3 Prototype cell and pack implementation

The future potential of polymer-based Li metal batteries in electric vehicles was evaluated in collaboration with the company FEV (Feel EVolution). FEV is a leading global engineering service provider in vehicle and powertrain development and located in Aachen.[109] A cell prototype was built in Münster and taken as model cell for a projection towards larger multi-layer cells. Further implementation in modules and packs was projected specifically for application in state-of-the-art battery electric vehicles. The cell design involves a cathode active area of 36.4 cm^2 and a total cell stack thickness of 155 µm, as demonstrated in ***Figure 63***. The cell dimensions, in particular the ratio of length and width of 2.75 : 1, were set based on recommendations by FEV for optimized pack implementation (including venting paths and steel cross beams). The main cell components comprise a commercially available NMC83 cathode (CustomCells, 2 mAh cm^{-2}) on Al-foil, a free-standing Li metal foil (Honjo, 50 µm), a

free-standing polymer electrolyte membrane (50 µm, sandwich-type hybrid[61]), as well as metal tabs and pouch foil. The Li metal is oversized to ensure full covering of the cathode active area and the electrolyte is oversized to prevent short circuits due to misalignment.

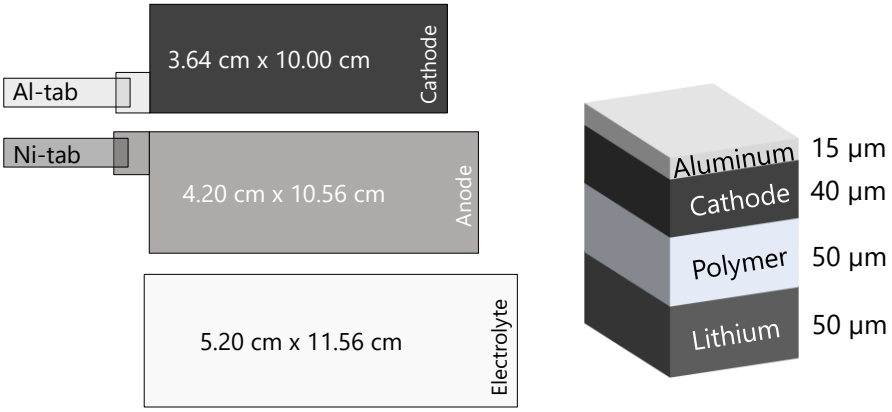

Figure 63: *Cell dimensions of the single-layer prototype pouch cell containing free-standing Li metal foil and an NMC83 cathode (mass loading 12 mg cm^{-2}).*

Various challenges and potential error sources could be identified during manufacturing of the prototype cell. The preparation of the electrolyte membrane with dimensions of 5.20 cm x 11.56 cm was possible by hot-pressing, although this procedure yielded a large standard deviation of the membrane's thickness with (50 ± 20) µm throughout the membrane area.

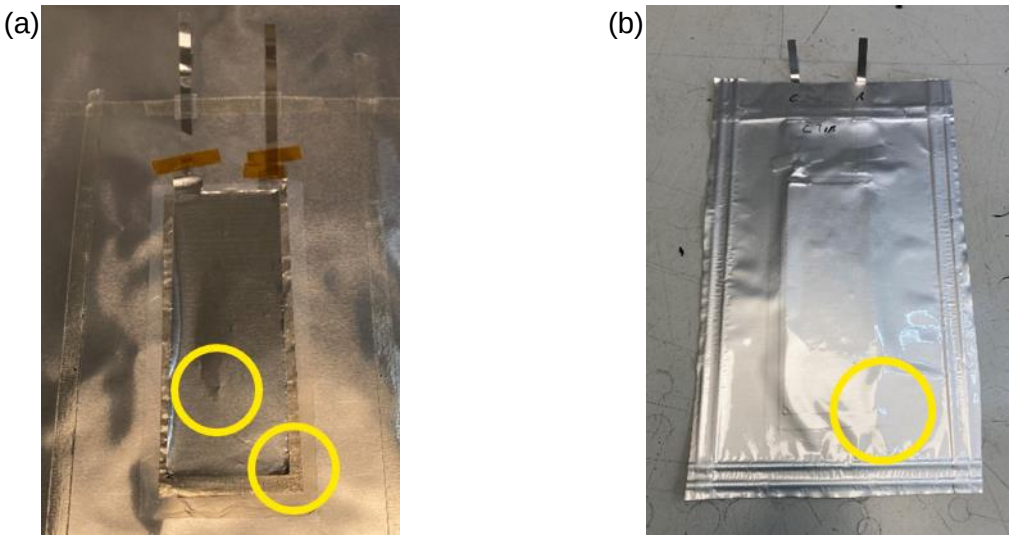

Figure 64: *Pictures of the large prototype pouch cell before (a) and after (b) sealing the pouch foil. Potentially critical errors are marked in yellow, including micro-cracks at the edge and center of the electrodes, as well as pouch foil folds due to non-ideal sealing.*

As illustrated in ***Figure 64a***, the manual assembly and handling of the large electrodes caused visible surface damages to both anode and cathode. Handling of 50 µm thin Li metal inevitably caused folds within the metal, which could be partly smoothened by adding light pressure with a transparent foil (Mylar® foil). Stacking of the individual layers was comparably unproblematic due to the largely oversized anode and electrolyte membrane. Vacuum sealing of the large

pouch cell, however, led to sealing folds. Each individual component, as well as the complete prototype cell was weighed to get an estimation of the impact of individual components on the total weight. As demonstrated in ***Figure 65a***, the pouch foil, tapes and current collector tabs make up 87 % of the total weight, mostly due to the large excess of the pouch foil compared to the cell stack. To reduce the excess mass, special sealing procedures and equipment needs to be utilized in the future. Semi-automatized cell assembly would also enable non-oversized electrodes due to higher stacking precision. The second largest contribution to the weight comes from the cathode, with the composition shown in which is shown in ***Figure 65b***. The active material takes 59 wt% of the cathode, followed by the current collector and the catholyte (oligomer). In a multi-layered cell, the active material content would increase further, as aluminum current collector would be coated with active material on both sides. The electrolyte (***Figure 65c***) mostly consists of the polymer (49 wt%), followed by the Li salt and the separator. Here, thin layered electrolytes are important, as the salt is the costly part. Reducing the salt content would not be favorable in terms of electrochemical properties (i.e., ionic conductivity), thus the overall amount of the electrolyte should be kept as low as possible, without compromising electrochemical performance. Detailed masses of the individual components are given in ***Table A3***, ***Table A4***, and ***Table A5*** in the Appendix.

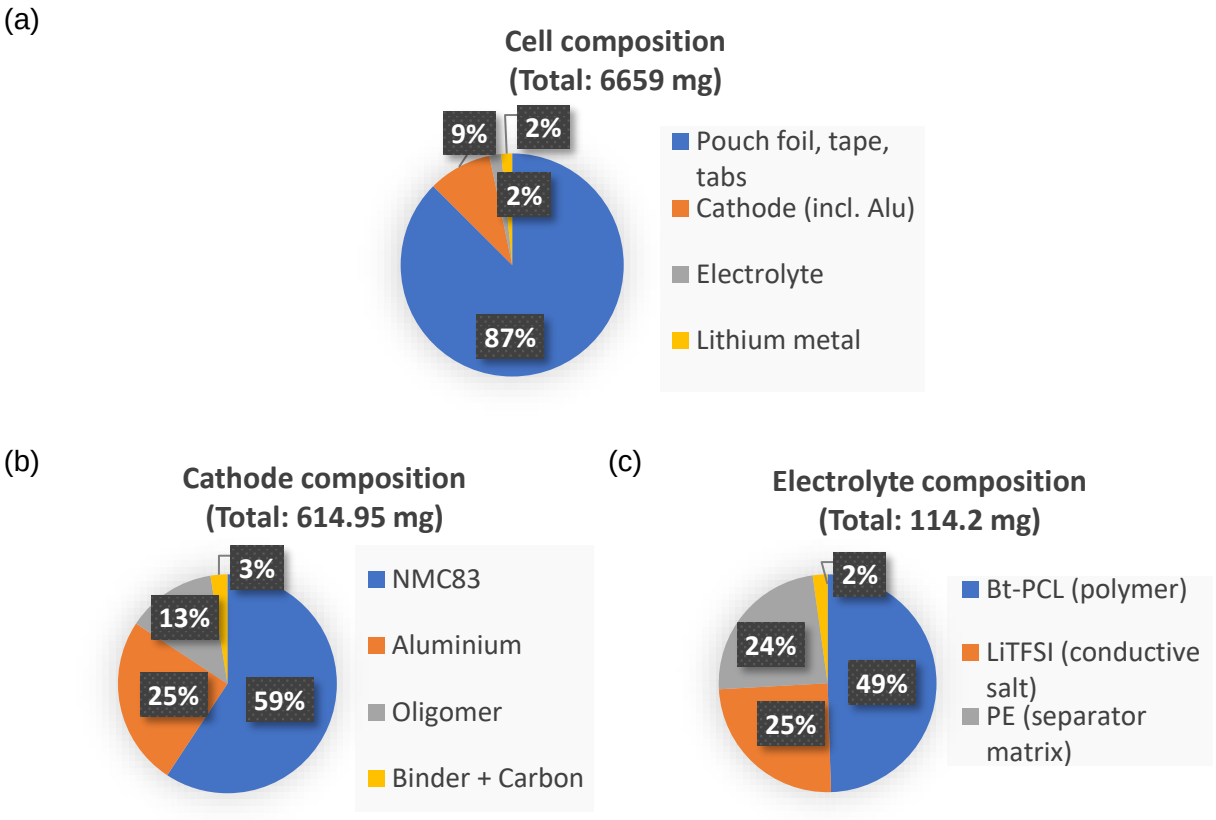

Figure 65: *Prototype single-layer pouch cell composition (a), cathode composition (b), and electrolyte composition (c).*

Projections of the energy density and specific energy based on the prototype cell are visualized in ***Figure 66***. In a first step, the number of layers is increased to 16, which drastically increases both specific energy and energy density due to the decreasing impact of the casing. The cell capacity of projection I with 1.2 Ah is in a realistic range for multi-layer prototype cells.[108] In steps B and C, the cell dimensions are scaled up for optimized implementation in battery packs. Here, increasing the area to 31.0 x 11.2 cm² and avoiding oversized anodes (step B) is more effective than increasing the number of layers from 16 to 60 (step C). With a total cell thickness of 7.6 mm, projection III can be implemented in a battery pack, as designed by FEV. In an even more optimistic scenario, the cell area is further in increased to 68.1 x 11.2 cm², yielding a cell capacity of 189.6 Ah at an energy density and specific energy of 800 Wh L^{-1} and 490 Wh kg^{-1}, respectively.

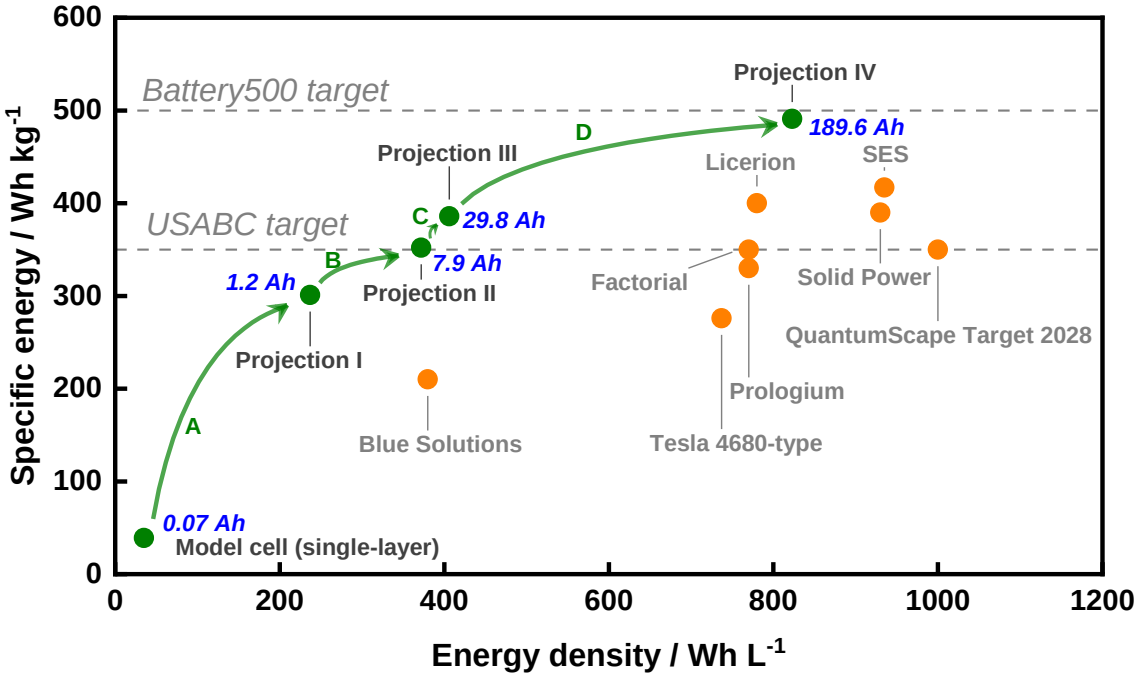

Figure 66: *Projection of energy density and specific energy, beginning with single-layer model cells.*

The cell projections III and IV were further considered for implementation in battery packs, based on state-of-the-art battery designs in electric vehicles (***Figure 67***). The battery size of 1,705 x 1,393 x 138 mm³ was kept the same for both projections, yielding 62 kWh and 136 kWh for projection III and projection IV, respectively. The larger cell design (projection IV) drastically increased the pack energy density, since additional metal bars and other passive elements could be omitted.

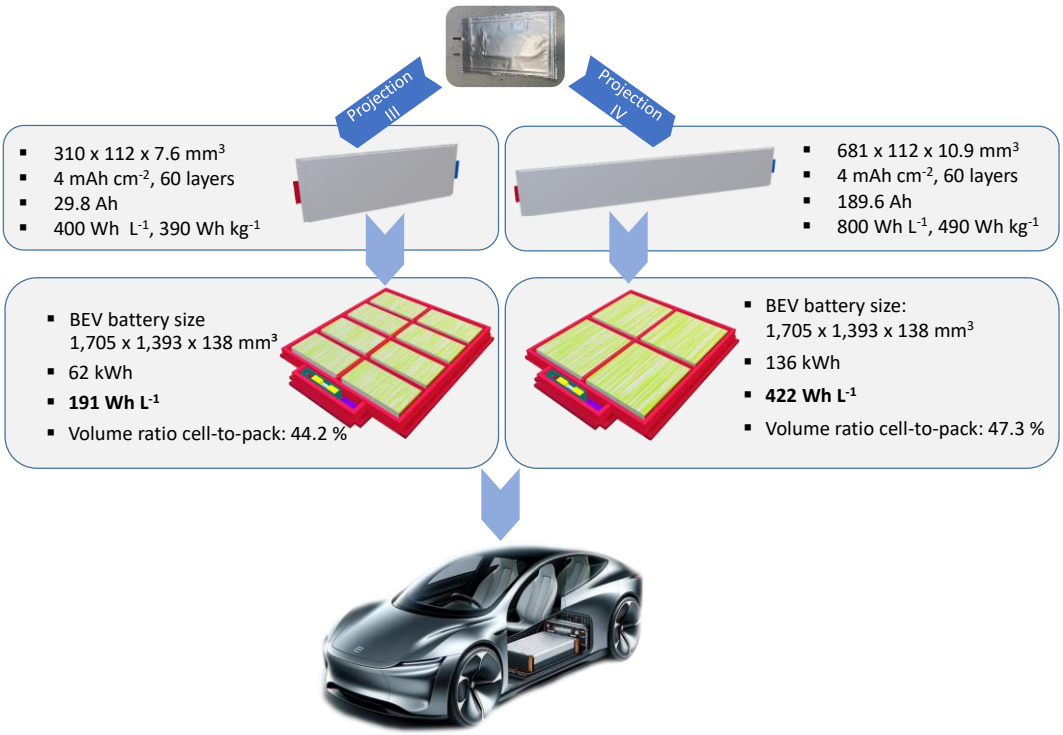

Figure 67: *Cell-to-pack projections for the implementation in electric vehicles, from individual cells to of two different sizes to pack designs and implementation in electric vehicles.*

To put the projected values on pack level into perspective, the energy content of the battery packs of both projections is considered, anticipating potential driving ranges of electric vehicles that contain these batteries. Various state-of-the-art battery electric vehicles are compared regarding their battery pack energy and achievable driving ranges. In ***Figure 68***, the estimated driving ranges of electric vehicles available on the market are visualized in combination with their battery pack energy to get an impression of potential ranges of the projected battery systems. The data was retrieved from an online data base[110] and includes small vehicles with low ranges (e.g., Renault Twingo Electric, 135 km), as well as high-end luxury cars (e.g., Mercedes EQS 450+ with a reported range of 690 km). With a pack energy of 62 kWh, electric vehicles with the battery from projection III would yield moderate driving ranges of 300 to 400 km. Nevertheless, with an average annual mileage of 12.670 km in Germany (as of 2022)[111], the average distance to be covered per week is 244 km, thus charging would be required only once in 1 to 2 weeks. Electric vehicles with batteries from projection IV would enable ranges beyond 700 km that are competitive with most combustion cars.

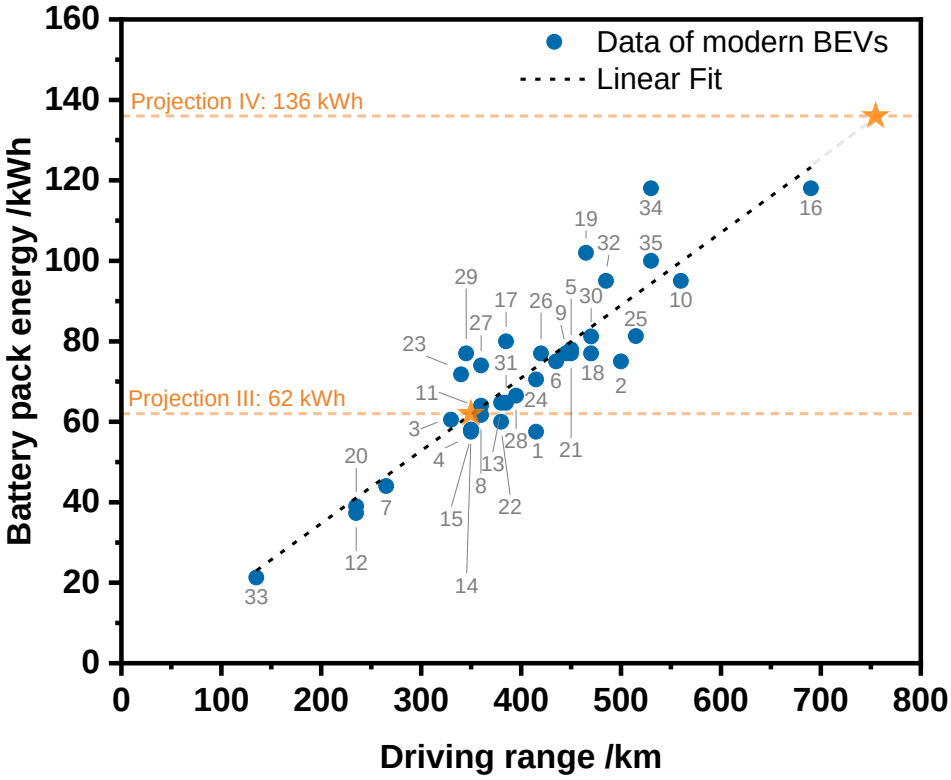

1	Tesla Model 3	**13**	BMW iX1 xDrive30	**25**	BMW i4 eDrive40
2	Tesla Model 3 Long Range	**14**	VW ID3 Pro	**26**	Audi Q4 e-tron 45
3	BYD Atto 3	**15**	Cupra Born	**27**	Kia EV6 GT
4	Tesla Model Y	**16**	Mercedes EQS 450+	**28**	Mercedes EQA 250
5	Kia EV3 Long Range	**17**	Hyundai IONIQ5 N	**29**	VW ID.Buzz Pro
6	Tesla Model Y Long Range	**18**	VW ID7 Pro	**30**	BMW i5 eDrive 40 Sedan
7	Citroen e-C3	**19**	Rolls-Royce Spectre	**31**	Mini Countryman E
8	MG MG4	**20**	Nissan Leaf	**32**	Porsche Macan 4
9	VW ID4 Pro	**21**	Skoda Enyaq 85	**33**	Renault Twingo Electric
10	Tesla Model S Plaid	**22**	Renault Megane E-Tech	**34**	Mercedes EQS SUV 500
11	Volvo EX30 Single Motor	**23**	BYD SEAL U	**35**	Lotus Emeya S
12	Fiat 500e	**24**	Mercedes EQB 250+		

***Figure 68**: Battery pack energies and driving ranges of various battery electric vehicles (BEVs) available on the market. Data retrieved from EV Database.[110] For comparison, the projections of the polymer-based Li metal battery are marked in orange. The linear fit demonstrates the relation between average pack energy and driving range, with an average of (0.18 ± 0.01) kWh km^{-1}.*

Though it is yet unclear if manufacturing and operation of cells based on projection IV will be feasible in the future from a safety perspective, it impressively demonstrates the potential of polymer electrolyte-based Li metal batteries for employment in electric vehicles. While a cell-to-pack design enables outstanding ranges and energy densities, further upscaling and safety tests of larger prototype cells with capacities > 1Ah are required to gain deeper insight to the features of the proposed cell chemistries.

4.4.4 Key achievements of this chapter

Energy densities and specific energies of multilayered cells can be estimated based on small-scale single-layer cell data, exploiting a straightforward interactive graphical tool. In particular, the following results could be achieved.

The long road to next generation batteries [3,25]

- There is a mismatch of fundamental scientific results for the development of polymer-based electrolytes and technological realization. To achieve smoother transfer between academic research and industrially relevant performance parameters, a new metric was introduced: The average energy output per unit area and cycle.
- The energy output is based on purely academic research data, such as average specific capacity, operating voltage and active electrode mass loadings. Most polymer electrolyte-based systems presented in literature are operated at low cathode mass loadings (< 6 mg cm^{-2}), yielding unfavorable average energy outputs (< 3 mWh cm^{-2}).

Having a closer look: Energy density and specific energy [25]

- At early development stages of cell chemistries, manufacture of larger cells is often challenging due to materials scarcity. Nevertheless, to evaluate the potential of a cell system, a projection towards larger cells is required, where parameters such as energy density and specific energy are relevant performance indicators.
- The program ProSpecDense was developed using Python for the projection of energy density and specific energy of multi-layered pouch-type cells, and allows straightforward control of input parameters by sliders and entry fields. All parameters are experimentally accessible even at early stages of the research.
- Projections of energy density and specific capacity based on experimental polymer-based Li metal batteries reveal that high cathode mass loadings (> 10 mg cm^{-2}), as well as thin electrolyte layers (< 30 µm) and thin metal anodes (< 20 µm) are required to achieve competitive values (> 250 Wh kg^{-1}, > 400 Wh L^{-1})
- At a constant charging rate, cells with higher cathode mass loadings must be capable to withstand higher current densities, which can be identified as a major challenge for polymer electrolytes. Hybrid systems offering with higher ionic conductivity (e.g. mixtures of polymers with flowable liquids or inorganic solids) present a promising strategy to achieve higher current densities and with that, higher cathode mass loadings at decent charging rates (> 0.5 C).

Prototype cell and pack implementation [112]

- The projections of energy density and specific energy were further used to evaluate the application potential in battery electric vehicles (BEVs), especially considering state-of-the-art cell-to-pack design strategies.
- Based on an experimental prototype, two scenarios were evaluated: A small cell with areal dimensions of 31 x 11 cm^2 and a large cell with dimensions of 68 x 11 cm^2. The latter could achieve a projected energy of 136 kWh in a complete battery pack suitable for the implementation in BEVs, yielding an impressive pack energy density of 422 Wh L^{-1}.
- The obtained performance parameters were translated into an average driving range and compared to state-of-the-art BEVs. The (perhaps more realistic) scenario of the smaller battery with an energy content of 62 kWh yielded a competitive range of 300 to 400 km, while the most optimistic scenario yielded an extraordinary range of 750 km.

5. Conclusion and outlook

In four sections, polymer-based Li metal batteries were analyzed from different perspectives, ranging from a better understanding of microscopic fundamental charge transfer to the assessment of the application potential of these batteries in electric vehicles. The key findings are summarized in ***Figure 69***. In the first section, the impedance of polymer electrolytes operated in various cell designs was determined by electrochemical impedance spectroscopy and further interpreted based on a distribution of relaxation times analysis (DRT). A custom-developed DRT fitting program allows to resolve the respective resistances in the time domain and to differentiate contributions of various processes to the overall impedance. DRT also enables the identification of ionic conductivities and, under suitable conditions, permittivity of the bulk polymer electrolytes, as well as quantification of the interphase resistances between polymer and Li metal and monitoring of changes thereof.

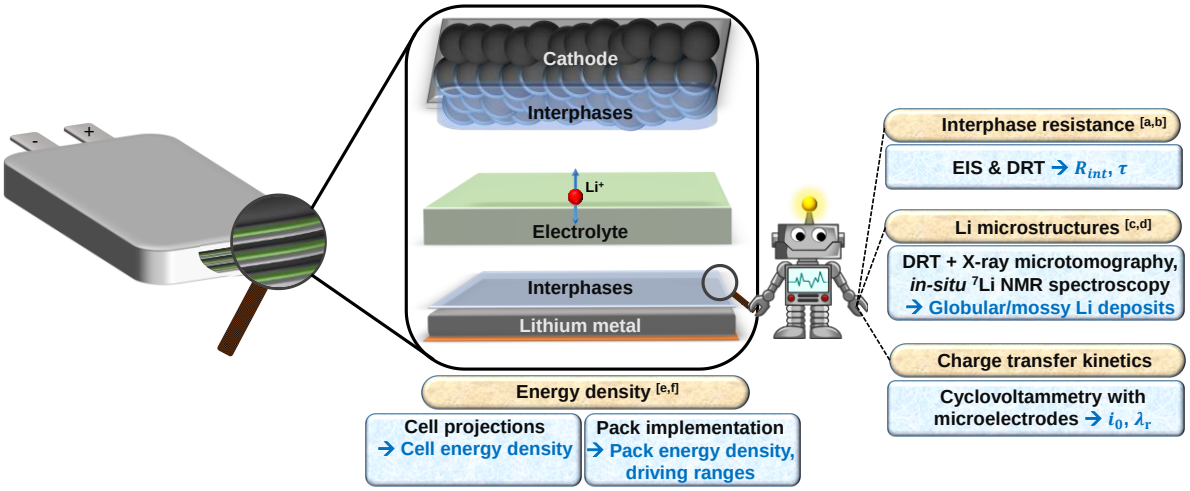

Figure 69: *Conclusive scheme of a pouch-type cell and its individual layers, focusing on the key observables analyzed and discussed. These include the interphase resistance R_{int} and associated time constant τ, Li metal deposit microstructures (globular/mossy), the exchange current density i_0 and the associated reorganization energy λ_r, as well as the energy density on both cell and pack level. The achievements of this thesis work are indicated with letters and refer to the following publications: [a] Lennartz et al.[62], [b] Chen et al.[61], [c] Frenck et al.[53], [d] Li et al.[56], [e] Lennartz et al.[25], [f] Brunklaus et al.[3]*

Due to the inherently ill-posed optimization problem of the DRT algorithm, regularization is required to prevent overfitting contributions from noise. Corresponding parameters ranging between 0.1 and 0.5 were identified in this work as suitable choices for most experiments. While fully dry polymer systems exhibit comparatively high interphase resistances on the order of 100 to 800 Ω cm^2 at elevated temperatures of 40 °C to 60 °C, gel-type electrolytes can also be operated at lower temperatures of 20 °C. Still, they exhibit large interphase resistances of, for example, 700 Ω cm^2 against Li metal electrodes at 20 °C. The benefits and applicability of DRT on polymer-based systems were demonstrated in multiple research papers.[61,62,113]

In the second section, Li metal deposit microstructures were monitored during galvanostatic cell operation. Here, a tailored combination of impedance spectroscopy, DRT and X-ray microtomography revealed that the cell failure upon cycling in case of gel polymer electrolytes mainly originates from two conditions: At low current densities (0.1 mA cm^{-2}), the formation of large globular Li metal protrusions at electrode and electrolyte impurities over a period of hundreds of cycles causes membrane ruptures and eventually short circuits. The occurrence of these protrusions was accompanied by increasing interfacial resistances and appearance of resistances at lower frequencies (higher relaxation times). At higher current densities (0.3 mA cm^{-2}), the presence of “mossy”, higher surface area lithium metal deposits constitutes the dominating failure mode and is reflected by decreasing interfacial resistances. The corresponding DRT spectra showed a rapid decrease in resistance without shifting towards higher or lower time constants, thus indicating that the microscopic growth at the electrodes is mainly contributing to the impedance decay. A collaborative paper was published based on these results.[53] In another work, the Li metal deposit microstructures established on pristine and modified Li metal electrodes upon galvanostatic charging were monitored with *in situ* ^{7}Li NMR spectroscopy. The noted trends of the ^{7}Li NMR chemical shifts and relative intensity of signals attributed to the individual Li metal deposit microstructures compared to “smooth” bulk Li metal electrodes (a condition after cell assembly) corroborated beneficial effects of artificial electrode coatings, that is, enrichment of fluorinated anions at the electrode surface by selectively displacing the strongly coordinating solvent molecules form the first solvation shell of solvated Li ions. Indeed, a resulting organic-less and LiF-rich SEI layer substantially enhanced achievable electrochemical performances of Li metal-based cells, as jointly demonstrated with project partners.[56] The presented results of this section unambiguously highlight that Li metal deposit microstructures represent a key indicator for assessment of cell performances, which requires the availability of non-destructive analytical methods to monitor changes thereof upon cell operation. In this respect, a combined approach by X-ray microtomography, NMR and impedance spectroscopy turned out to be very useful.

In the third section, interfacial charge transfer at or across Li metal|polymer electrolyte interfaces is explored by fast cyclovoltammetry. Since the necessary fast scan rates of up to 10 V s^{-1} required a proper design of microelectrodes, custom-made tungsten electrodes were fabricated that act as reaction site for both Li metal plating and stripping. Observations from literature, where the current-voltage relation follows Marcus-Hush type kinetics in case of liquid electrolytes that are in contact with Li metal electrodes, could be confirmed to hold true also for cells operating polymer-based electrolytes. However, in this case, explicitly achievable exchange current densities of the cells (at equilibrium) are ten to a hundred times lower than those of typical liquid electrolytes, reflecting the comparably slow charge transfer kinetics of polymer electrolytes. The estimated reorganization energy of 0.3 eV is comparable to that of

liquid electrolytes, but nevertheless highlighting, that the intrinsic capability of charge transfer is more limited in case of polymer electrolytes compared to liquid electrolytes. Thus, challenges remain not only to enable better bulk ionic conductivities, but also in view of enhancing the rate of interfacial charge transfer.

In the fourth section, the application potential of polymer-based Li metal batteries was critically evaluated by projecting energy densities and specific energies of academic cell systems. Upon introducing an application-oriented figure of merit, the average energy density per area and cycle, it was evidenced that most academic electrochemical results regarding polymer electrolytes emphasize cycling procedures that are not practically relevant, particularly considering cathode active material mass loadings of well below 6 mg cm^{-2}. Thus, to afford a more successful transition of lab research results into practical relevance, a custom-made software ("ProSpecDense") was developed that allows to conveniently project specific energies and energy densities of application-oriented multi-layered cells. Essential parameters to achieve competitive energy densities and specific energies include cathode active material mass loadings > 10 mg cm^{-2}, as well as polymer electrolyte thicknesses of < 30 µm and exploitation of rather thin Li metal anodes (< 20 µm). In terms of further improvement of battery components, the major residual challenges comprise the achievement of 1) sufficient ionic and electronic conductivity within composite cathodes to enable competitive mass loadings, 2) larger-scale implementation of thin electrolyte membranes that provide ionic conductivities > 1 mS cm^{-1} to grant sufficient cell charging rates of > 0.5 C, and establishment of 3) reversible low-excess Li metal anodes that offer limited Li excess to compensate for capacity losses during cell formation, but not more than that. Finally, a single-layer prototype cell was built and utilized as model cell for further projections towards successful implementation in suitably sized battery packs for long-term operation in battery electric vehicles. Accounting for the presumably enhanced operational safety of the pack, granted by in principle leakage-free hybrid polymer electrolytes, rather competitive pack energy densities of up to 422 Wh L^{-1} could be predicted, thereby enabling an energy content of 136 kWh, which could provide average driving ranges of up to 750 km. Notably, the results were disseminated in two review papers and a conference talk.[3,25,112]

In summary, no individual cell chemistry can currently claim the spot as "the" next generation solution of rechargeable batteries. To date, polymer-based Li metal batteries are particularly promising, not least due their demonstrated commercial application in public buses in France (Blue Solution). However, inherent limitations of polymer electrolytes in view of charge transfer rates at electrodes and overall ionic conductivity narrows their chances to be considered for industrial fast charge applications (e.g. exploitation in premium battery electric vehicles). Here, other cell chemistries, such as silicon-based anodes operated with liquid or

hybrid electrolytes, or innovative pack designs may provide benefits, not only for stationary storage but also for cost-effective “medium” battery electric vehicle applications. Despite the claimed superior operational safety of solid polymer electrolytes (attributed to their leakage-free operation), polymer constituents are still flammable under certain conditions, similar to the Li metal that is present at the anodes. A transition of a newly introduced cell chemistries towards applications in view of industry would require adequate safety and performance tests of substantially larger cells that afford capacities well beyond 1 Ah. In this respect, a tailored combination of inorganic ceramic particles and suitably designed polymer electrolytes is probably among the most promising contemporary cell chemistries that could enable application of polymer-based Li metal batteries. In these hybrid systems, inorganic particles may act as mechanical stabilizer, while eventually promoting ionic conductivity. A limited addition of intrinsically safer and affordable flowable components (such as oligomers or ionic liquids) may be a salient strategy to promote charge carrier transport within composite cathodes and across electrode interfaces, in this way eventually yielding solutions for next-generation batteries.

6. References

[1] J. Baars, T. Domenech, R. Bleischwitz, H. E. Melin, O. Heidrich, *Nat. Sustain.* **2020**, *4*, 71, DOI: 10.1038/s41893-020-00607-0.

[2] United States Advanced Battery Consortium, Retrieved from: https://uscar.org/usabc/, 29.05.2023.

[3] G. Brunklaus, P. Lennartz, M. Winter, *Nat. Rev. Electr. Eng.* **2024**, DOI: 10.1038/s44287-023-00006-5.

[4] M. Winter, B. Barnett, K. Xu, *Chem. Rev.* **2018**, *118*, 11433, DOI: 10.1021/acs.chemrev.8b00422.

[5] P. Kurzweil, *J. Power Sources* **2010**, *195*, 4424, DOI: 10.1016/j.jpowsour.2009.12.126.

[6] J. B. Baker, *Sci. Am.* **1911**, *104*, 30, DOI: https://www.jstor.org/stable/26020853.

[7] C. Kittel, *Introduction to solid state physics*, 8th ed., Wiley, Hoboken, NJ, **2005**.

[8] N. W. Ashcroft, N. D. Mermin, *Solid state physics*, Holt, Rinehart and Winston, New York, **1976**.

[9] R. G. Compton, C. E. Banks, *Understanding voltammetry*, Third edition., World Scientific, New Jersey, **2018**.

[10] P. W. Atkins, J. De Paula, *Atkins' Physical chemistry*, 8th ed., W.H. Freeman, New York, **2006**.

[11] A. J. Bard, L. R. Faulkner, H. S. White, *Electrochemical methods: fundamentals and applications*, Third edition., Wiley, Hoboken, NJ, USA Chichester, West Sussex, UK, **2022**.

[12] J. S. Newman, N. P. Balsara, *Electrochemical systems*, Fourth edition., Wiley, Hoboken, NJ, **2019**.

[13] D. T. Boyle, X. Kong, A. Pei, P. E. Rudnicki, F. Shi, W. Huang, Z. Bao, J. Qin, Y. Cui, *ACS Energy Lett* **2020**, *5*, 701, DOI: 10.1021/acsenergylett.0c00031.

[14] N. Pereira, G. G. Amatucci, M. S. Whittingham, R. Hamlen, *J. Power Sources* **2015**, *280*, 18, DOI: 10.1016/j.jpowsour.2015.01.056.

[15] J. Liu, Z. Bao, Y. Cui, E. J. Dufek, J. B. Goodenough, P. Khalifah, Q. Li, B. Y. Liaw, P. Liu, A. Manthiram, Y. S. Meng, V. R. Subramanian, M. F. Toney, V. V. Viswanathan, M. S. Whittingham, J. Xiao, W. Xu, J. Yang, X.-Q. Yang, J.-G. Zhang, *Nat. Energy* **2019**, *4*, 180, DOI: 10.1038/s41560-019-0338-x.

[16] J.-N. Chazalviel, *Phys. Rev. A* **1990**, *42*, 7355, DOI: 10.1103/PhysRevA.42.7355.

[17] H. Yang, H. Li, J. Li, Z. Sun, K. He, H. Cheng, F. Li, *Angew. Chem. Int. Ed.* **2019**, *58*, 11978, DOI: 10.1002/anie.201814031.

[18] C.-J. Huang, B. Thirumalraj, H.-C. Tao, K. N. Shitaw, H. Sutiono, T. T. Hagos, T. T. Beyene, L.-M. Kuo, C.-C. Wang, S.-H. Wu, W.-N. Su, B. J. Hwang, *Nat. Commun.* **2021**, *12*, 1452, DOI: 10.1038/s41467-021-21683-6.

[19] Z. M. Konz, B. D. McCloskey, *Nat. Energy* **2022**, *7*, 1005, DOI: 10.1038/s41560-022-01142-2.

[20] F. Duffner, N. Kronemeyer, J. Tübke, J. Leker, M. Winter, R. Schmuch, *Nat. Energy* **2021**, *6*, 123, DOI: 10.1038/s41560-020-00748-8.

[21] C. Niu, D. Liu, J. A. Lochala, C. S. Anderson, X. Cao, M. E. Gross, W. Xu, J. G. Zhang, M. S. Whittingham, Xiao, *Nat. Energy* **2021**, *6*, 723, DOI: 10.1038/s41560-021-00852-3.

[22] M. Winter, *Z. Für Phys. Chem.* **2009**, *223*, 1395, DOI: 10.1524/zpch.2009.6086.

[23] M. Winter, H. Wiemhöfer, R. Kostecki, X. Chen, *Batter. Supercaps* **2020**, *3*, 212, DOI: 10.1002/batt.201900148.

[24] E. Peled, S. Menkin, *J. Electrochem. Soc.* **2017**, *164*, A1703, DOI: 10.1149/2.1441707jes.

[25] P. Lennartz, B. A. Paren, A. Herzog-Arbeitman, X. C. Chen, J. A. Johnson, M. Winter, Y. Shao-Horn, G. Brunklaus, *Joule* **2023**, *7*, 1471, DOI: 10.1016/j.joule.2023.06.006.

[26] Z. Huang, S. Choudhury, N. Paul, J. H. Thienenkamp, P. Lennartz, H. Gong, P. Müller-Buschbaum, G. Brunklaus, R. Gilles, Z. Bao, *Adv. Energy Mater.* **2022**, *12*, 2103187, DOI: 10.1002/aenm.202103187.

[27] N. Li, Y. Shi, Y. Yin, X. Zeng, J. Li, C. Li, L. Wan, R. Wen, Y. Guo, *Angew. Chem. Int. Ed.* **2018**, *57*, 1505, DOI: 10.1002/anie.201710806.

[28] X. Yu, P. Lennartz, R. Sahore, N. Dudney, G. Brunklaus, N. P. Balsara, In *Macromolecular Engineering* (Eds.: Hadjichristidis, N.; Gnanou, Y.; Matyjaszewski, K.; Muthukumar, M.), Wiley, **2022**, pp. 1–19.

[29] M. Kirchhöfer, J. Zamory, E. Paillard, S. Passerini, *Int J Mol Sci* **2014**, *15*, 14868, DOI: 10.3390/ijms150814868.
[30] M. Schalenbach, B. Hecker, B. Schmid, Y. E. Durmus, H. Tempel, H. Kungl, R. Eichel, *Electrochem. Sci. Adv.* **2023**, *3*, e2100189, DOI: 10.1002/elsa.202100189.
[31] A. Mistry, Z. Yu, L. Cheng, V. Srinivasan, *J. Electrochem. Soc.* **2023**, *170*, 110536, DOI: 10.1149/1945-7111/ad0c66.
[32] K. Xu, *Chem. Rev.* **2014**, *114*, 11503, DOI: 10.1021/cr500003w.
[33] K. Xu, *Chem. Rev.* **2004**, *104*, 4303, DOI: 10.1021/cr030203g.
[34] J. Landesfeind, J. Hattendorff, A. Ehrl, W. A. Wall, H. A. Gasteiger, *J. Electrochem. Soc.* **2016**, *163*, A1373, DOI: 10.1149/2.1141607jes.
[35] R. B. MacMullin, G. A. Muccini, *AIChE J.* **1956**, *2*, 393, DOI: 10.1002/aic.690020320.
[36] P. Arora, Z. (John) Zhang, *Chem. Rev.* **2004**, *104*, 4419, DOI: 10.1021/cr020738u.
[37] A. J. Manly, W. E. Tenhaeff, *J. Mater. Chem. A* **2022**, *10*, 10557, DOI: 10.1039/D1TA10730E.
[38] K. M. Abraham, *Electrochimica Acta* **1993**, *38*, 1233, DOI: 10.1016/0013-4686(93)80054-4.
[39] D. Diddens, A. Heuer, *ACS Macro Lett.* **2013**, *2*, 322, DOI: 10.1021/mz3006457.
[40] Z. Song, F. Chen, M. Martinez-Ibañez, W. Feng, M. Forsyth, Z. Zhou, M. Armand, H. Zhang, *Nat. Commun.* **2023**, *14*, 4884, DOI: 10.1038/s41467-023-40609-y.
[41] Q. Zhao, S. Stalin, C.-Z. Zhao, L. A. Archer, *Nat. Rev. Mater.* **2020**, *5*, 229, DOI: 10.1038/s41578-019-0165-5.
[42] V. Bocharova, A. P. Sokolov, *Macromolecules* **2020**, *53*, 4141, DOI: 10.1021/acs.macromol.9b02742.
[43] K. Borzutzki, J. Thienenkamp, M. Diehl, M. Winter, G. Brunklaus, *J Mater Chem Mater* **2019**, *7*, 188, DOI: 10.1039/C8TA08391F.
[44] M. E. Orazem, B. Tribollet, *Electrochemical impedance spectroscopy*, Wiley, Hoboken (New Jersey), **2008**.
[45] J. R. Macdonald, *Impedance Spectroscopy, Theory, Experiment, and Applications 2nd edition, p.37*, 2nd ed., **2005**.
[46] O. Pecher, J. Carretero-González, K. J. Griffith, C. P. Grey, *Chem. Mater.* **2017**, *29*, 213, DOI: 10.1021/acs.chemmater.6b03183.
[47] H. J. Chang, N. M. Trease, A. J. Ilott, D. Zeng, L.-S. Du, A. Jerschow, C. P. Grey, *J. Phys. Chem. C* **2015**, *119*, 16443, DOI: 10.1021/acs.jpcc.5b03396.
[48] C. W. Groetsch, *The theory of Tikhonov regularization for Fredholm equations of the first kind*, Pitman Advanced Pub. Program, Boston, **1984**.
[49] J. Hadamard, *Lectures on Cauchy's problem in linear partial differential equations*, Dover Publications, Mineola, N.Y, **2003**.
[50] A. N. Tikhonov, A. V. Goncharsky, V. V. Stepanov, A. G. Yagola, *Numerical Methods for the Solution of Ill-Posed Problems*, Springer Netherlands, Dordrecht, **1995**.
[51] M. Hahn, S. Schindler, L.-C. Triebs, M. A. Danzer, *Batteries* **2019**, *5*, 43, DOI: 10.3390/batteries5020043.
[52] C. L. Lawson, R. J. Hanson, *Solving least squares problems*, SIAM, Philadelphia, **1995**.
[53] L. Frenck, P. Lennartz, D. Y. Parkinson, M. Winter, N. P. Balsara, G. Brunklaus, *ACS Appl. Mater. Interfaces* **2022**, *14*, 53893, DOI: 10.1021/acsami.2c16869.
[54] K. Borzutzki, K. Dong, J. R. Nair, B. Wolff, F. Hausen, R.-A. Eichel, M. Winter, I. Manke, G. Brunklaus, *Cell Rep Phys Sci* **2021**, *2, 100496*, DOI: 10.1016/j.xcrp.2021.100496.
[55] R. J. Pandolfi, D. B. Allan, E. Arenholz, L. Barroso-Luque, S. I. Campbell, T. A. Caswell, A. Blair, F. De Carlo, S. Fackler, A. P. Fournier, G. Freychet, M. Fukuto, D. Gürsoy, Z. Jiang, H. Krishnan, D. Kumar, R. J. Kline, R. Li, C. Liman, S. Marchesini, A. Mehta, A. T. N'Diaye, D. Y. Parkinson, H. Parks, L. A. Pellouchoud, T. Perciano, F. Ren, S. Sahoo, J. Strzalka, D. Sunday, C. J. Tassone, D. Ushizima, S. Venkatakrishnan, K. G. Yager, P. Zwart, J. A. Sethian, A. Hexemer, *J. Synchrotron Radiat.* **2018**, *25*, 1261, DOI: 10.1107/S1600577518005787.
[56] G.-X. Li, P. Lennartz, V. Koverga, R. Kou, A. Nguyen, H. Jiang, M. Liao, D. Wang, N. Dandu, M. Zepeda, H. Wang, K. Wang, A. T. Ngo, G. Brunklaus, D. Wang, *Proc. Natl. Acad. Sci.* **2024**, *121*, e2311732121, DOI: 10.1073/pnas.2311732121.
[57] Y. Chen, Y. Hsieh, K. L. Liu, L. Wichmann, J. H. Thienenkamp, A. Choudhary, D. Bedrov, M. Winter, G. Brunklaus, *Macromol. Rapid Commun.* **2022**, *43*, 2200335, DOI: 10.1002/marc.202200335.

[58] M.-H. Chiou, E. Verweyen, D. Diddens, L. Wichmann, C. Schmidt, K. Neuhaus, A. Choudhary, D. Bedrov, M. Winter, G. Brunklaus, *ACS Appl. Energy Mater.* **2023**, *6*, 4422, DOI: 10.1021/acsaem.3c00571.
[59] Y.-C. Hsieh, J. H. Thienenkamp, C.-J. Huang, H.-C. Tao, U. Rodehorst, B. J. Hwang, M. Winter, G. Brunklaus, *J. Phys. Chem. C* **2021**, *125*, 252, DOI: 10.1021/acs.jpcc.0c09771.
[60] Y.-C. Hsieh, M. Leißing, S. Nowak, B.-J. Hwang, M. Winter, G. Brunklaus, *Cell Rep. Phys. Sci.* **2020**, *1*, 100139, DOI: 10.1016/j.xcrp.2020.100139.
[61] Y. Chen, P. Lennartz, K. L. Liu, Y. Hsieh, F. Scharf, R. Guerdelli, A. Buchheit, M. Grünebaum, F. Kempe, M. Winter, G. Brunklaus, *Adv. Funct. Mater.* **2023**, 2300501, DOI: 10.1002/adfm.202300501.
[62] P. Lennartz, K. Borzutzki, M. Winter, G. Brunklaus, *Electrochimica Acta* **2021**, *388*, 138526, DOI: 10.1016/j.electacta.2021.138526.
[63] E. Ivers-Tiffée, A. Weber, *J. Ceram. Soc. Jpn.* **2017**, *125*, 193, DOI: 10.2109/jcersj2.16267.
[64] M. A. Danzer, *Batteries* **2019**, *5*, 53, DOI: 10.3390/batteries5030053.
[65] M. E. Orazem, *J. Solid State Electrochem.* **2023**, DOI: 10.1007/s10008-023-05755-9.
[66] D. S. Hall, J. Self, J. R. Dahn, *J. Phys. Chem. C* **2015**, *119*, 22322, DOI: 10.1021/acs.jpcc.5b06022.
[67] U. Krewer, F. Röder, E. Harinath, R. D. Braatz, B. Bedürftig, R. Findeisen, *J. Electrochem. Soc.* **2018**, *165*, A3656, DOI: 10.1149/2.1061814jes.
[68] R. Guo, D. Wang, L. Zuin, B. M. Gallant, *ACS Energy Lett.* **2021**, *6*, 877, DOI: 10.1021/acsenergylett.1c00117.
[69] R. Guo, B. M. Gallant, *Chem. Mater.* **2020**, *32*, 5525, DOI: 10.1021/acs.chemmater.0c00333.
[70] Y. Ma, J. Wan, Y. Yang, Y. Ye, X. Xiao, D. T. Boyle, W. Burke, Z. Huang, H. Chen, Y. Cui, Z. Yu, S. T. Oyakhire, Y. Cui, *Adv. Energy Mater.* **2022**, *12*, 2103720, DOI: 10.1002/aenm.202103720.
[71] M.-H. Chiou, K. Borzutzki, J. H. Thienenkamp, M. Mohrhardt, K.-L. Liu, V. Mereacre, J. R. Binder, H. Ehrenberg, M. Winter, G. Brunklaus, *J. Power Sources* **2022**, *538*, 231528, DOI: 10.1016/j.jpowsour.2022.231528.
[72] P. Lennartz, Master thesis: Cross-linked viscoelastic polysiloxanes as artificial coating on Li metal anodes, Universität Duisburg-Essen, **2019**.
[73] J. Becking, A. Gröbmeyer, M. Kolek, U. Rodehorst, S. Schulze, M. Winter, P. Bieker, M. C. Stan, *Adv. Mater. Interfaces* **2017**, *4*, 1700166, DOI: 10.1002/admi.201700166.
[74] K. Borzutzki, J. R. Nair, M. Winter, G. Brunklaus, *ACS Appl Mater Interfaces* **2022**, *14*, 5211, DOI: 10.1021/acsami.1c19097.
[75] Y. Ding, X. Shen, J. Zeng, X. Wang, L. Peng, P. Zhang, J. Zhao, *Solid State Ion.* **2018**, *323*, 16, DOI: 10.1016/j.ssi.2018.05.009.
[76] L. Porcarelli, A. S. Shaplov, F. Bella, J. R. Nair, D. Mecerreyes, C. Gerbaldi, *ACS Energy Lett* **2016**, *1*, 678, DOI: 10.1021/acsenergylett.6b00216.
[77] C. W. Hewlett, *Phys. Rev.* **1921**, *17*, 284, DOI: 10.1103/PhysRev.17.284.
[78] A. Groso, M. Stampanoni, R. Abela, P. Schneider, S. Linga, R. Müller, *Appl. Phys. Lett.* **2006**, *88*, 214104, DOI: 10.1063/1.2207221.
[79] F. Maia, A. MacDowell, S. Marchesini, H. A. Padmore, D. Y. Parkinson, J. Pien, A. Schirotzek, C. Yang, (Eds.: Bones, P. J.; Fiddy, M. A.; Millane, R. P.), San Diego, California, USA, **2010**, p. 78000F.
[80] K. J. Harry, X. Liao, D. Y. Parkinson, A. M. Minor, N. P. Balsara, *J. Electrochem. Soc.* **2015**, *162*, A2699, DOI: 10.1149/2.0321514jes.
[81] A. S. Ho, P. Barai, J. A. Maslyn, L. Frenck, W. S. Loo, D. Y. Parkinson, V. Srinivasan, N. P. Balsara, *ACS Appl. Energy Mater.* **2020**, *3*, 9645, DOI: 10.1021/acsaem.0c01175.
[82] R. Bhattacharyya, B. Key, H. Chen, A. S. Best, A. F. Hollenkamp, C. P. Grey, *Nat. Mater.* **2010**, *9*, 504, DOI: 10.1038/nmat2764.
[83] X. Zhang, X. Cheng, X. Chen, C. Yan, Q. Zhang, *Adv. Funct. Mater.* **2017**, *27*, 1605989, DOI: 10.1002/adfm.201605989.
[84] D. Weintz, S. P. Kühn, M. Winter, I. Cekic-Laskovic, *ACS Appl. Mater. Interfaces* **2023**, *15*, 53526, DOI: 10.1021/acsami.3c12797.

[85] L. Sheng, Q. Wang, X. Liu, H. Cui, X. Wang, Y. Xu, Z. Li, L. Wang, Z. Chen, G.-L. Xu, J. Wang, Y. Tang, K. Amine, H. Xu, X. He, *Nat. Commun.* **2022**, *13*, 172, DOI: 10.1038/s41467-021-27841-0.
[86] R. A. Marcus, *Annu. Rev. Phys. Chem.* **1964**, *15*, 155, DOI: 10.1146/annurev.pc.15.100164.001103.
[87] N. S. Hush, *Trans. Faraday Soc.* **1961**, *57*, 557, DOI: 10.1039/tf9615700557.
[88] C. E. D. Chidsey, *Science* **1991**, *251*, 919, DOI: 10.1126/science.251.4996.919.
[89] National Aeronautics and Space Administration, *Technology Readiness level*, Retrieved from: https://www.nasa.gov/directorates/heo/scan/engineering/technology/technology_readiness_level, 19.07.2023.
[90] K. Edström, R. Dominko, M. Fichtner, S. Perraud, *Battery 2030+ Roadmap*, Uppsala University, **2020**.
[91] M. Greenwood, J. M. Wrogemann, R. Schmuch, H. Jang, M. Winter, J. Leker, *J. Power Sources Adv.* **2022**, *14*, 100089, DOI: 10.1016/j.powera.2022.100089.
[92] S. Stock, J. Hagemeister, S. Grabmann, J. Kriegler, J. Keilhofer, M. Ank, J. L. S. Dickmanns, M. Schreiber, F. Konwitschny, N. Wassiliadis, M. Lienkamp, R. Daub, *Electrochimica Acta* **2023**, *471*, 143341, DOI: 10.1016/j.electacta.2023.143341.
[93] D. H. S. Tan, Y.-T. Chen, H. Yang, W. Bao, B. Sreenarayanan, J.-M. Doux, W. Li, B. Lu, S.-Y. Ham, Sayahpour, *Science* **2021**, *373*, 1494, DOI: 10.1126/science.abg7217.
[94] H. Wu, Y. Xu, X. Ren, B. Liu, M. H. Engelhard, M. S. Ding, P. Z. El-Khoury, L. Zhang, Q. Li, K. Xu, C. Wang, J. Zhang, W. Xu, *Adv. Energy Mater.* **2019**, *9*, 1902108, DOI: 10.1002/aenm.201902108.
[95] W. Xue, M. Huang, Y. Li, Y. G. Zhu, R. Gao, X. Xiao, W. Zhang, S. Li, G. Xu, Y. Yu, *Nat. Energy* **2021**, *6*, 495, DOI: 10.1038/s41560-021-00792-y.
[96] N. Wassiliadis, M. Steinsträter, M. Schreiber, P. Rosner, L. Nicoletti, F. Schmid, M. Ank, O. Teichert, L. Wildfeuer, J. Schneider, A. Koch, A. König, A. Glatz, J. Gandlgruber, T. Kröger, X. Lin, M. Lienkamp, *eTransportation* **2022**, *12*, 100167, DOI: 10.1016/j.etran.2022.100167.
[97] K. Knehr, J. Kubal, P. Nelson, S. Ahmed, *Battery Performance and Cost Modeling for Electric-Drive Vehicles (A Manual for BatPaC v5.0)*, **2022**, p. ANL/CSE-22/1, 1877590, 176234.
[98] M. Dixit, A. Parejiya, R. Essehli, N. Muralidharan, S. U. Haq, R. Amin, I. Belharouak, *Cell Rep. Phys. Sci.* **2022**, *3*, 100756, DOI: 10.1016/j.xcrp.2022.100756.
[99] H. Sun, X. Xie, Q. Huang, Z. Wang, K. Chen, X. Li, J. Gao, Y. Li, H. Li, J. Qiu, W. Zhou, *Angew. Chem.* **2021**, *133*, 18483, DOI: 10.1002/ange.202107667.
[100] S. Perticarari, *AABC Eur. 2023* **2023**.
[101] Tesla 4680 Cell, Battery Design, Retrieved from: https://www.batterydesign.net/tesla-4680-cell/, 09.11.2023.
[102] Licerion Products Sion, Retrieved from: https://sionpower.com/products/, 09.11.2023.
[103] Technology, *QuantumScape*, Retrieved from: https://www.quantumscape.com/technology/, 09.11.2023.
[104] SolidPower, Retrieved from: https://www.solidpowerbattery.com/, 09.11.2023.
[105] SES, Retrieved from: https://ses.ai/li-metal-batteries/, 29.05.2023.
[106] ProLogium Debuts Its Next-Generation Solid-State Battery Technologies at the 2022 Paris Motor Show, Batteries News, Retrieved from: https://batteriesnews.com/prologium-debuts-next-generation-solid-state-battery-technologies-2022-paris-motor-show/., 09.11.2023.
[107] Factorial announces 40 Ah solid-state cells, electrive, Retrieved from: https://www.electrive.com/2021/04/22/factorial-announces-40-ah-solid-state-cellls/, 09.11.2023.
[108] C. Niu, H. Lee, S. Chen, Q. Li, J. Du, W. Xu, J.-G. Zhang, M. S. Whittingham, J. Xiao, J. Liu, *Nat. Energy* **2019**, *4*, 551, DOI: 10.1038/s41560-019-0390-6.
[109] FEV, Retrieved from: https://www.fev.com/ueber-fev/, 07.06.2024.
[110] Electric Vehicle Database, Retrieved from: https://ev-database.org/, 07.06.2024.
[111] Deutsche Automobil Treuhand GmbH, *Jahresfahrleistung der Pkw-Halter*, Retrieved from: https://www.dat.de/news/jahresfahrleistung/, 14.06.2024.
[112] F. Pampel, P. Lennartz, H. Löbberding, M. Teuber, M. Winter, G. Brunklaus, M. Stapelbroek, *Conf. Talk Adv. Automot. Battery Conf.* **2023**.

[113] G. M. Overhoff, M. Y. Ali, J.-P. Brinkmann, P. Lennartz, H. Orthner, M. Hammad, H. Wiggers, M. Winter, G. Brunklaus, *ACS Appl. Mater. Interfaces* **2022**, *14*, 53636, DOI: 10.1021/acsami.2c13408.
[114] Z. Wei, S. Chen, J. Wang, Z. Wang, Z. Zhang, X. Yao, Y. Deng, X. Xu, *J Mater Chem Mater* **2018**, *6*, 13438, DOI: 10.1039/C8TA04477E.
[115] H. Zhang, F. Chen, O. Lakuntza, U. Oteo, L. Qiao, M. Martinez-Ibañez, H. Zhu, J. Carrasco, M. Forsyth, M. Armand, *Angew Chem Int Ed* **2019**, *58*, 12070, DOI: 10.1002/anie.201905794.
[116] M. Martinez-Ibañez, E. Sanchez-Diez, L. Qiao, Y. Zhang, X. Judez, A. Santiago, I. Aldalur, J. Carrasco, H. Zhu, M. Forsyth, *Adv. Funct. Mater.* **2020**, *30*, 2000455, DOI: 10.1002/adfm.202000455.
[117] C. Wang, T. Wang, L. Wang, Z. Hu, Z. Cui, J. Li, S. Dong, X. Zhou, G. Cui, *Adv. Sci.* **2019**, *6, 1901036*, DOI: 10.1002/advs.201901036.
[118] J. Chai, Z. Liu, J. Ma, J. Wang, X. Liu, H. Liu, J. Zhang, G. Cui, L. Chen, *Adv. Sci.* **2017**, *4*, 1600377, DOI: 10.1002/advs.201600377.
[119] P. Hovington, M. Lagacé, A. Guerfi, P. Bouchard, A. Mauger, C. M. Julien, M. Armand, K. Zaghib, *Nano Lett* **2015**, *15*, 2671, DOI: 10.1021/acs.nanolett.5b00326.
[120] N. Boaretto, A. Bittner, C. Brinkmann, B.-E. Olsowski, J. Schulz, M. Seyfried, K. Vezzù, M. Popall, V. Noto, *Chem Mater* **2014**, *26*, 6339, DOI: 10.1021/cm5024647.
[121] B. Zhou, Y. H. Jo, R. Wang, D. He, X. Zhou, X. Xie, Z. Xue, *J Mater Chem Mater* **2019**, *7*, 10354, DOI: 10.1039/C9TA01214A.
[122] W. Tang, S. Tang, X. Guan, X. Zhang, Q. Xiang, J. Luo, *Adv. Funct. Mater.* **2019**, *29*, 1900648, DOI: 10.1002/adfm.201900648.
[123] H. Huo, Y. Chen, J. Luo, X. Yang, X. Guo, X. Sun, *Adv. Energy Mater.* **2019**, *9*, 1804004, DOI: 10.1002/aenm.201804004.
[124] F. Kaneko, S. Wada, M. Nakayama, M. Wakihara, J. Koki, S. Kuroki, *Adv. Funct. Mater.* **2009**, *19*, 918, DOI: 10.1002/adfm.200800789.
[125] J. Jie, Y. Liu, L. Cong, B. Zhang, W. Lu, X. Zhang, J. Liu, H. Xie, L. Sun, *J En Chem* **2020**, *49*, 80, DOI: 10.1016/j.jechem.2020.01.019.
[126] T. Dong, J. Zhang, G. Xu, J. Chai, H. Du, L. Wang, H. Wen, X. Zang, A. Du, Q. Jia, *Energy Env. Sci* **2018**, *11*, 1197, DOI: 10.1039/C7EE03365F.
[127] X. Liu, G. Ding, X. Zhou, S. Li, W. He, J. Chai, C. Pang, Z. Liu, G. Cui, *J Mater Chem Mater* **2017**, *5*, 11124, DOI: 10.1039/C7TA02423A.
[128] L. Zhao, J. Fu, Z. Du, X. Jia, Y. Qu, F. Yu, J. Du, Y. Chen, *J Memb Sci* **2019**, *593*, 117428, DOI: 10.1016/j.memsci.2019.117428.
[129] H. Wu, Y. Cao, H. Su, C. Wang, *Angew Chem Int Ed* **2018**, *57*, 1361, DOI: 10.1002/anie.201709774.
[130] L. Porcarelli, M. A. Aboudzadeh, L. Rubatat, J. R. Nair, A. S. Shaplov, C. Gerbaldi, D. Mecerreyes, *J. Power Sources* **2017**, *364*, 191, DOI: 10.1016/j.jpowsour.2017.08.023.
[131] R. Bouchet, S. Maria, R. Meziane, A. Aboulaich, L. Lienafa, J.-P. Bonnet, T. N. T. Phan, D. Bertin, D. Gigmes, D. Devaux, *Nat. Mater.* **2013**, *12*, 452, DOI: 10.1038/nmat3602.
[132] F. Lu, G. Li, Y. Yu, X. Gao, L. Zheng, Z. Chen, *Chem Eng J* **2020**, *384*, 123237, DOI: 10.1016/j.cej.2019.123237.
[133] Y. Chen, G. Xu, X. Liu, Q. Pan, Y. Zhang, D. Zeng, Y. Sun, H. Ke, H. Cheng, *RSC Adv* **2018**, *8*, 39967, DOI: 10.1039/C8RA07557C.
[134] H.-D. Nguyen, G.-T. Kim, J. Shi, E. Paillard, P. Judeinstein, S. Lyonnard, D. Bresser, C. Iojoiu, *Energy Env. Sci* **2018**, *11*, 3298, DOI: 10.1039/C8EE02093K.
[135] P.-Y. Ji, J. Fang, Y.-Y. Zhang, P. Zhang, J.-B. Zhao, *Chem Electro Chem* **2017**, *4*, 2352, DOI: 10.1002/celc.201700256.
[136] Q. Pan, Y. Chen, Y. Zhang, D. Zeng, Y. Sun, H. Cheng, *J. Power Sources* **2016**, *336*, 75, DOI: 10.1016/j.jpowsour.2016.10.033.
[137] Y. Chen, H. Ke, D. Zeng, Y. Zhang, Y. Sun, H. Cheng, *J Memb Sci* **2017**, *525*, 349, DOI: 10.1016/j.memsci.2016.12.011.
[138] D. Du, X. Hu, D. Zeng, Y. Zhang, Y. Sun, J. Li, H. Cheng, *ACS Appl Energy Mater* **2020**, *3*, 1128, DOI: 10.1021/acsaem.9b02180.
[139] C. Cao, Y. Li, Y. Feng, C. Peng, Z. Li, W. Feng, *Energy Storage Mater* **2019**, *19*, 401, DOI: 10.1016/j.ensm.2019.03.004.

[140] K. Deng, J. Qin, S. Wang, S. Ren, D. Han, M. Xiao, Y. Meng, *Small* **2018**, *14*, 1801420, DOI: 10.1002/smll.201801420.
[141] K. Deng, S. Wang, S. Ren, D. Han, M. Xiao, Y. Meng, *J. Power Sources* **2017**, *360*, 98, DOI: 10.1016/j.jpowsour.2017.06.006.
[142] D. Shin, J. E. Bachman, M. K. Taylor, J. Kamcev, J. G. Park, M. E. Ziebel, E. Velasquez, N. N. Jarenwattananon, G. K. Sethi, Y. Cui, *Adv. Mater.* **2020**, *32, 1905771*, DOI: 10.1002/adma.201905771.
[143] P.-F. Cao, B. Li, G. Yang, S. Zhao, J. Townsend, K. Xing, Z. Qiang, K. D. Vogiatzis, A. P. Sokolov, J. Nanda, *Macromolecules* **2020**, *53*, 3591, DOI: 10.1021/acs.macromol.9b02683.
[144] Z. Chen, D. Steinle, H.-D. Nguyen, J.-K. Kim, A. Mayer, J. Shi, E. Paillard, C. Iojoiu, S. Passerini, D. Bresser, *Nano Energy* **2020**, *77, 105129*, DOI: 10.1016/j.nanoen.2020.105129.
[145] B. Qin, Z. Liu, G. Ding, Y. Duan, C. Zhang, G. Cui, *Electrochim Acta* **2014**, *141*, 167, DOI: 10.1016/j.electacta.2014.07.004.
[146] C. Li, B. Qin, Y. Zhang, A. Varzi, S. Passerini, J. Wang, J. Dong, D. Zeng, Z. Liu, H. Cheng, *Adv. Energy Mater.* **2019**, *9*, 1803422, DOI: 10.1002/aenm.201803422.
[147] X. Ren, L. Zou, X. Cao, M. H. Engelhard, W. Liu, S. D. Burton, H. Lee, C. Niu, B. E. Matthews, Zhu, *Joule* **2019**, *3*, 1662, DOI: 10.1016/j.joule.2019.05.006.
[148] A. Cronk, Y.-T. Chen, G. Deysher, S.-Y. Ham, H. Yang, P. Ridley, B. Sayahpour, L. H. B. Nguyen, J. A. S. Oh, J. Jang, *ACS Energy Lett* **2023**, *8*, 827, DOI: 10.1021/acsenergylett.2c02138.
[149] Z. Zhang, S. Chen, J. Yang, J. Wang, L. Yao, X. Yao, P. Cui, X. Xu, *ACS Appl. Mat Int* **2018**, *10*, 2556, DOI: 10.1021/acsami.7b16176.

7. Abbreviations and symbols

Abbreviation/Symbol	Definition
α	Transfer coefficient
AC	Alternating current
BEV	Battery electric vehicle
BMS	Bulk magnetic susceptibility
C	Capacitance (unit: F)
C_{dl}	Double layer capacitance
C_{O}^{*}	Bulk concentration of the oxidized species
C_{R}^{*}	Bulk concentration of the reduced species
CEI	Cathode electrolyte interphase
CES	Crown-ether-functionalized silica
CPE	Constant phase element
DBTDL	Dibutyltindilaurate
ΔE	Electrode potential difference
ΔG	Gibbs energy ('free energy')
$\Delta G^{\ddagger}$	Gibbs energy (barrier for oxidation or reaction)
$\Delta_r G^{\ominus}$	Standard Gibbs energy of a reaction
$\Delta_r H^{\ominus}$	Standard reaction enthalpy
$\Delta_r S^{\ominus}$	Standard reaction entropy
DEC	Diethyl carbonate
DRT	Distribution of relaxation times
$\boldsymbol{E}$	Electric field
E	Measured (electrode) potential
$E^{0\prime}$	Formal potential
E_{eq}	Equilibrium potential
EIS	Electrochemical impedance spectroscopy
η	Surface overpotential ($E - E_{\mathrm{eq}}$)
EC	Ethylene carbonate
EIS	Electrochemical impedance spectroscopy
f	Frequency (unit: Hz)
f	Thermal constant (F/RT)
F	Faraday constant (96485.3 C mol^{-1})
FEC	Fluoroethylene carbonate
FID	Free induction decay
$G(t)$	Distribution function
i	Current density (unit: mA cm^{-2})
i_0	Exchange current density (unit: mA cm^{-2})
i_{f}	Faradaic current
I	Current (unit: A, mA)
IHP	Inner Helmholtz plane
k	Rate constant
k^0	Standard rate constant

$\bar{k}$	Force constant in Marcus theory
L	Inductance (unit: H)
λ	Tikhonov regularization parameter
λ_{r}	Reorganization energy (unit: eV, J)
LBNL	Lawrence Berkeley National Laboratory
LED	Light emitting diode
LFP	$LiFePO_4$
LiTFSI	Lithium bis(trifluoromethane)sulfonimide
LP47	1 M $LiPF_6$ in EC/DEC 3:7 wt.
$\mathrm{m_{act}}$	Active mass (loading) (unit: g, mg cm^{-2})
m_{i}	Mass of species i
M_i	Molar mass of species i
m_l	Mass of a single cathode/electrolyte/anode layer (unit: g)
μ	Chemical potential
$\bar{\mu}_j$	Electrochemical potential
n_j	Number of a chemical species j
n	Number of layers in a multilayered cell
NMC*xyz*	$LiNi_{0.x}Mn_{0.y}Co_{0.z}O_2$ (cathode material)
NMP	N-Methyl-2-pyrrolidone
NMR	Nuclear magnetic resonance
OCV	Open circuit voltage
OHP	Outer Helmholtz plane
ω	Radial frequency (unit: s^{-1})
PC	Propylene carbonate
PEEK	Polyether ether ketone
PEO	Polyethylene oxide
PEOS	Polyethylene oxide-functionalized silica
ϕ	Electric potential
PSA	Polysulfonamide
PSU	Pennsylvania State University
PVDF-HFP	Poly(vinylidene fluoride-co-hexafluoropropylene)
Q	Charge
q	Charge (unit: Ah, C)
q_{spec}, $\mathrm{Q_S}$	Specific capacity (unit: mAh g^{-1})
$q^{\ddagger}$	Marcus reaction coordinate of transition
q_{O}	Marcus reaction coordinate of oxidation
q_{R}	Marcus reaction coordinate of reduction
R	Resistance (unit: Ω or Ω cm^2)
$\bar{R}$	Universal gas constant (8.314 J mol^{-1} K^{-1})
R_{ct}	Charge transfer resistance
R_{int}	Interfacial/interphase resistance (unit: Ω or Ω cm^2)
R_{Ω}	Ohmic resistance (unit: Ω or Ω cm^2)
R_{b}	Bulk electrolyte resistance
RF	Radio frequency

ρ	Density (unit g cm^{-3})
S_r	Sum of squared residuals
SEI	Solid electrolyte interphase
SHE	Standard hydrogen electrode
σ	Ionic conductivity (unit: S cm^{-1})
t	Time (unit: h, min, s)
T	Temperature
τ	Time constant (unit: s)
τ_+	Transference number
USABC	United States Advanced Battery Consortium
$V_{tot.}$	Total volume (unit: cm^3)
z_j	Valency of species *j*
Z	Impedance

8. Acknowledgements

This thesis would not have been possible without the help of many individuals, whom I would like to thank in this chapter. First and foremost, I would like to thank my supervisor at the Helmholtz-Institute Münster, Gunther Brunklaus, for providing guidance from day one, giving me opportunities to develop both as a person and as a scientist. I would like to thank Prof. Hermann Nienhaus for accepting the supervision from Duisburg without hesitation, and for his support during the years. I would also like to thank Prof. Martin Winter for giving me the opportunity to do my research at the Helmholtz-Institute Münster and for acknowledging my work. I would like to thank Hinrich Meyer for his support during the writing of this thesis and for giving helpful advices regarding my scientific career. I would like to thank the U.S. partners, including Prof. Nitash Balsara, Louise Frenck, Dilworth Parkinson, Prof. Donghai Wang, Guoxing Li, Prof. Yang Shao-Horn, Benjamin Parren, Abraham Herzog-Arbeitman, and Chelsea Chen for the great collaboration. In particular, I would like to thank Louise Frenck, Benjamin Parren and Guoxing Li for jointly working on the paper drafts and conducting experiments. I would like to thank my colleagues at Münster for creating a work environment that promotes creativity and does not leave much space for monotony. In particular, I would like to thank Melanie Mitchell and Johannes Thienenkamp for reviewing my thesis and providing helpful suggestions. I would also like to thank Susanna Krämer for her feedback, as well as Min-Huei Chiou, Kun Ling Liu and Yi-Hsuan Chen for providing polymer electrolytes and additional data. I would like to thank Johannes Thienenkamp, Melanie Mitchell, and Karin Sowa for the great time after work, especially when playing music and cooking together. I would also like to thank all current and former members of the HIMS which I did not mention here. Last but not least, I would like to thank my family and friends for the support throughout the years. Thank you Katrin for your unconditional love and support and for being there for me anytime.

9. List of publications

First and co-first authorship:

- G. Brunklaus, **P. Lennartz**, M. Winter: Metal electrodes for next-generation rechargeable batteries, *Nature Reviews Electrical Engineering*, **2024**, [https://doi.org/10.1038/s44287-023-00006-5].
- **P. Lennartz**, B. A. Paren, A. Herzog-Arbeitman, X. C. Chen, J. A. Johnson, M. Winter, Y. Shao-Horn, G. Brunklaus: Practical considerations for enabling Li|polymer electrolyte batteries, *Joule*, 7, 1-25, **2023**, [https://doi.org/10.1016/j.joule.2023.06.006].
- L. Frenck, **P. Lennartz**, D. Y. Parkinson, M. Winter, N. P. Balsara, G. Brunklaus: Failure Mechanisms at the Interfaces between Lithium Metal Electrodes and a Single-Ion Conducting Polymer Gel Electrolyte, *ACS Applied Materials and Interfaces*, 14, 48, 53893 – 53903, **2022**, [https://doi.org/10.1021/acsami.2c16869].
- **P. Lennartz**, K. Borzutzki, M. Winter, G. Brunklaus: Viscoelastic polyborosiloxanes as artificial solid electrolyte interphase on lithium metal anodes, *Electrochimica Acta*, 388, 138526, **2021**, [https://doi.org/10.1016/j.electacta.2021.138526].

Co-authorship:

- J. Wellmann, M. Hepp, C. O. Ogolla, M. Mohrhardt, B. Wankmiller, **P. Lennartz**, U. Rodehorst, M. R. Hansen, M. Winter, G. Brunklaus, B. Butz, E. Paillard: Tailoring the Solid Electrolyte Interphase Composition on Lithium Metal Anodes by the Choice of Ionic Liquid During Mechanochemical Modification, *manuscript submitted*
- J. Thienenkamp, **P. Lennartz**, M. Winter, G. Brunklaus: Experimental Correlation of Anionic Mass-Transport and Lithium Dendrite Growth in Solid-State Polymer-Based Lithium Metal Batteries, *manuscript submitted*
- F. Scharf, A. Krude, **P. Lennartz**, M. Clausnitzer, G. Shukla, A. Buchheit, F. Kempe, D. Diddens, P. Glomb, M. Mitchell, T. Danner, A. Heuer, A. Latz, M. Winter, G. Brunklaus: Synergistic Enhancement of Mechanical and Electrochemical Properties in Grafted Polymer/Oxide Hybrid Electrolytes, *manuscript accepted*
- G. Li, **P. Lennartz**, V. Koverga, R. Kou, A. Nguyen, H. Jiang, M. Liao, D. Wang, N. Dandu, M. Zepeda, H. Wang, K. Wang, A. Ngo, G. Brunklaus, D. Wang: Interfacial solvation-structure regulation for stable Li metal anode by a desolvation coating technique, *Proceedings of the National Academy of Sciences of the United States of America, 121,* **2024**, [https://doi.org/10.1073/pnas.2311732121].

- E. Esen, M. Mohrhardt, **P. Lennartz**, I. de Meatza, M. Schmuck, M. Winter, E. Paillard: Effect of prelithiation with passivated lithium metal powder on passivation films on high-energy NMC-811 and SiCx electrodes, *Materials Today Chemistry*, 30, 101587, **2023**, [https://doi.org/10.1016/j.mtchem.2023.101587].

- Y.-H. Chen, **P. Lennartz**, K. L. Liu, Y.-C. Hsieh, F. Scharf, R. Guerdelli, A. Buchheit, M. Grünebaum, F. Kempe, M. Winter, G. Brunklaus: Towards all-solid-state polymer batteries: going beyond PEO with hybrid concepts, *Advanced Functional Materials*, 2300501, **2023**, [https://doi.org/10.1002/adfm.202300501].

- G. M. Overhoff, M. Y. Ali, J.-P. Brinkmann, **P. Lennartz**, H. Orthner, M. Hammad, H. Wiggers, M. Winter, G. Brunklaus: Ceramic-in-Polymer Hybrid Electrolytes with Enhanced Electrochemical Performance, *ACS Applied Materials and Interfaces*, 14, 48, 53636-53647, **2022**, [https://doi.org/10.1021/acsami.2c13408].

- X. Yu, **P. Lennartz**, R. Sahore, N. Dudney, G. Brunklaus, N. P. Balsara: Ion Transport in Batteries with Polymer Electrolytes, *Macromolecular Engineering*, 2nd Edition, **2022**, [https://doi.org/10.1002/9783527815562.mme0042].

- Z. Huang, S. Choudhury, N. Paul, J.H. Thienenkamp, **P. Lennartz**, H. Gong, P. Müller-Buschbaum, G. Brunklaus, R. Gilles, Z. Bao: Effects of Polymer Coating Mechanics at Solid-Electrolyte Interphase for Stabilizing Lithium Metal Anodes, *Advanced Energy Materials*, 12(5), 2103187, **2021**, [https://doi.org/10.1002/aenm.202103187].

Conference contributions:

- **P. Lennartz**, L. Frenck, D.Y. Parkinson, G. Li, M. Winter, D. Wang, N. Balsara, G. Brunklaus: Advanced characterization of Li metal anodes in contact with polymer electrolytes and artificial protective layers, *Poster Presentation*, *BatteryCityMünster and Baccara Power Day Münster,* **2023**.

- **P. Lennartz**, K. Ling Liu, Y.-H. Chen, J. H. Thienenkamp, M. Winter, G. Brunklaus: Charge transfer at interfaces and interphases between lithium metal and polymer electrolytes, *Poster presentation*, *Advanced Battery Power Conference – Kraftwerk Batterie*, Aachen, **2023**.

- F. Pampel, **P. Lennartz**, H. Löbberding, M. Teuber, M. Winter, G. Brunklaus, M. Stapelbroek: High-End Sustainable Battery Pack Concept with Solid-State Cells, *Conference talk, Advanced Automotive Battery Conference*, Mainz, **2023**.

- **P. Lennartz**, M. H. Chiou, J. H. Thienenkamp, M. Winter, G. Brunklaus: In Depth Analysis of Interfacial Processes between Lithium Metal and Polymer Electrolyte Using Electrochemical Impedance Spectroscopy and Distribution of Relaxation Times, *Digital presentation*, *242nd ECS meeting*, Atlanta, USA, **2022.**

10. Appendix

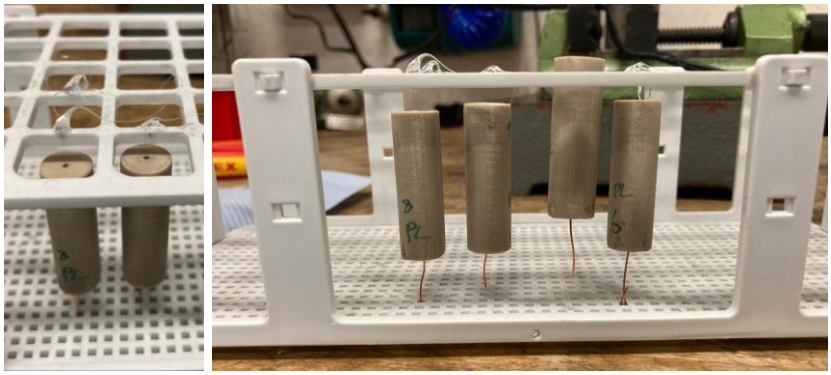

Figure A1: *Rack for curing the microelectrodes after filling the holes with epoxy resin. The tungsten wire is fixated with hot glue to the rack and is straightend by the weight of the cylinders.*

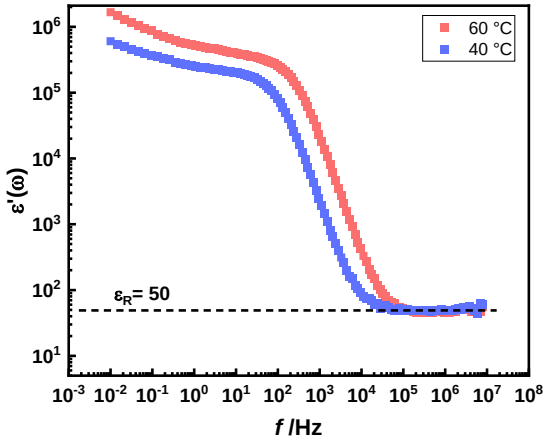

Figure A2: *Real part of the relative permittivity of the dry polymer electrolyte xGCD-PCL at temperatures of 40 °C and 60 °C.*

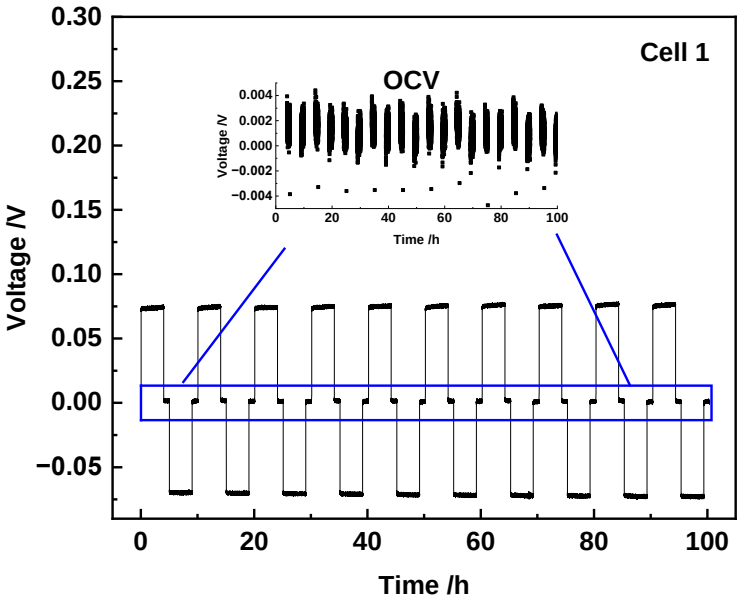

Figure A3: *Overvoltage of cell 1 during the formation cycles with relaxation steps that demonstrate an open circuit voltage (OCV) of 0 V.*

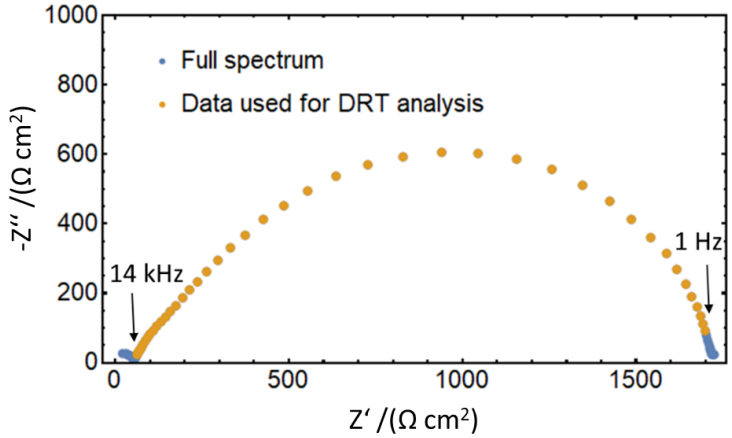

Figure A4: *Exemplary spectrum of Cell 1 before cycling at 25 °C to demonstrate the range of data points taken into consideration for DRT analysis. The high-frequency semi-circle contribution is associated with bulk electrolyte resistance (geometric capacitance) and typically occurs in polymer electrolyte systems, as the ionic conductivity is low enough to shift this contribution to the observed frequency domain.*

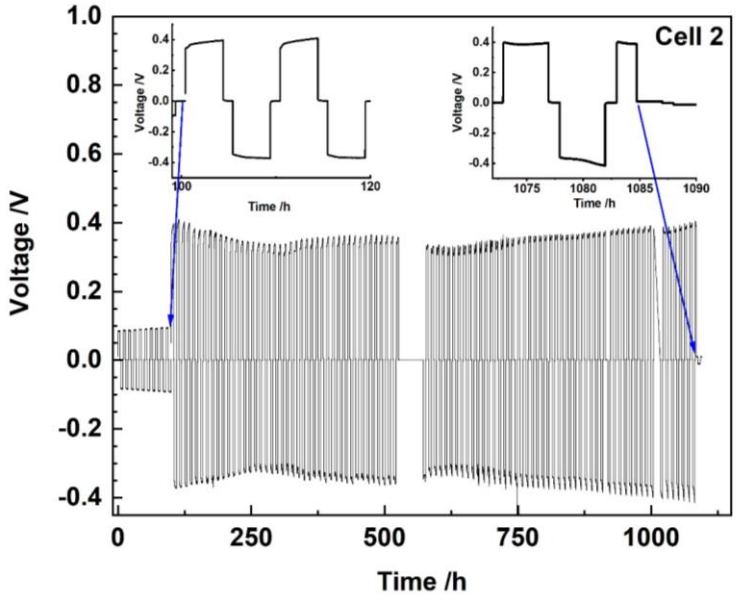

Figure A5: *Overvoltage as a function of time for cell 2 operated at a current density of 0.1 mA cm^{-2}. Reprinted with permission from ref.[53] Copyright © 2024 American Chemical Society.*

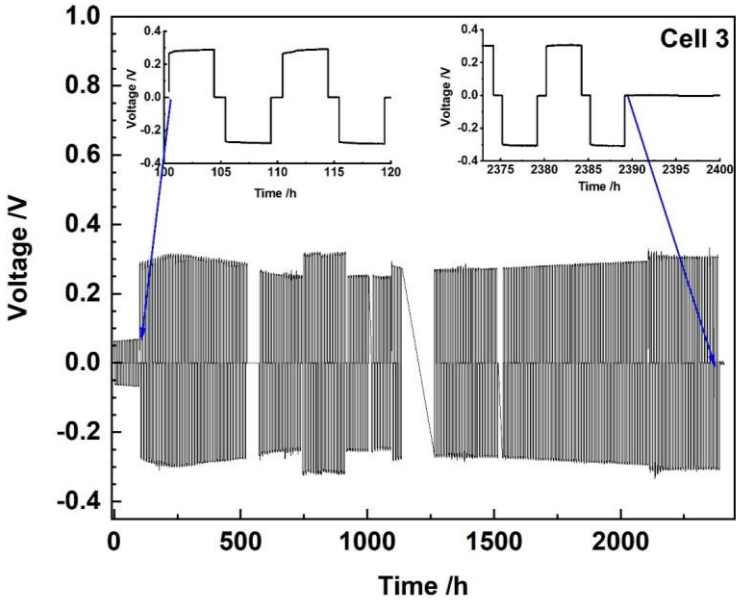

Figure A6: *Overvoltage as a function of time for cell 3 operated at a current density of 0.1 mA cm^{-2}. Reprinted with permission from ref.[53] Copyright © 2024 American Chemical Society.*

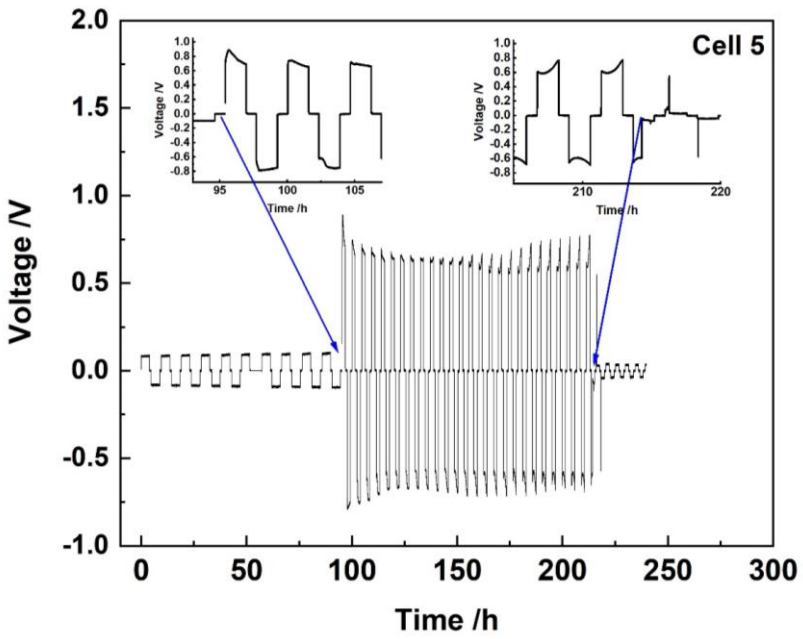

Figure A7: *Overvoltage as a function of time for cell 5 operated at a current density of 0.3 mA cm^{-2}. Reprinted with permission from ref.[53] Copyright © 2024 American Chemical Society.*

.

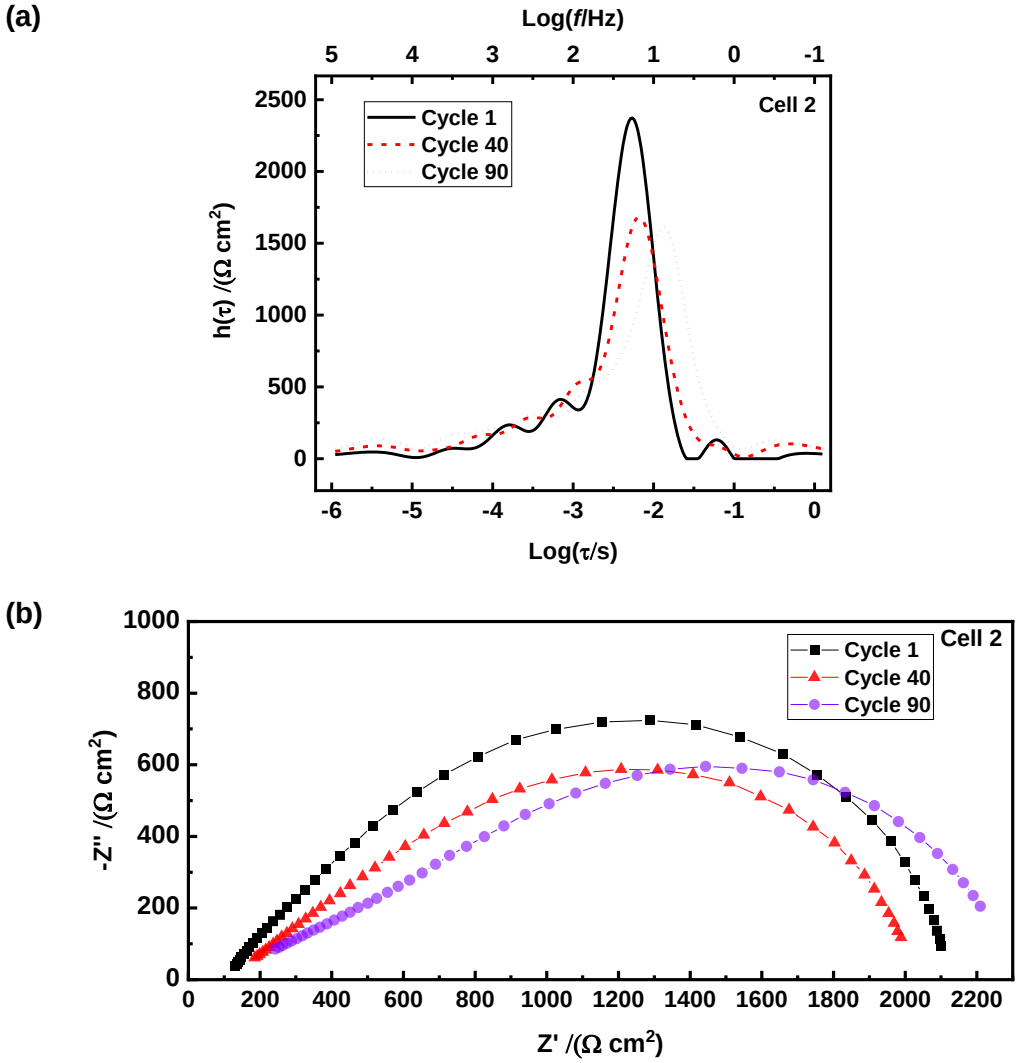

Figure A8: *(a) DRT spectrum of the overall impedances of cell 2 for cycles 1, 40, and 90 (cycling current density of 0.1 mA cm^{-2}). (b) Nyquist of normalized areal impedances of cell 2. Reprinted with permission from ref.[53] Copyright © 2024 American Chemical Society.*

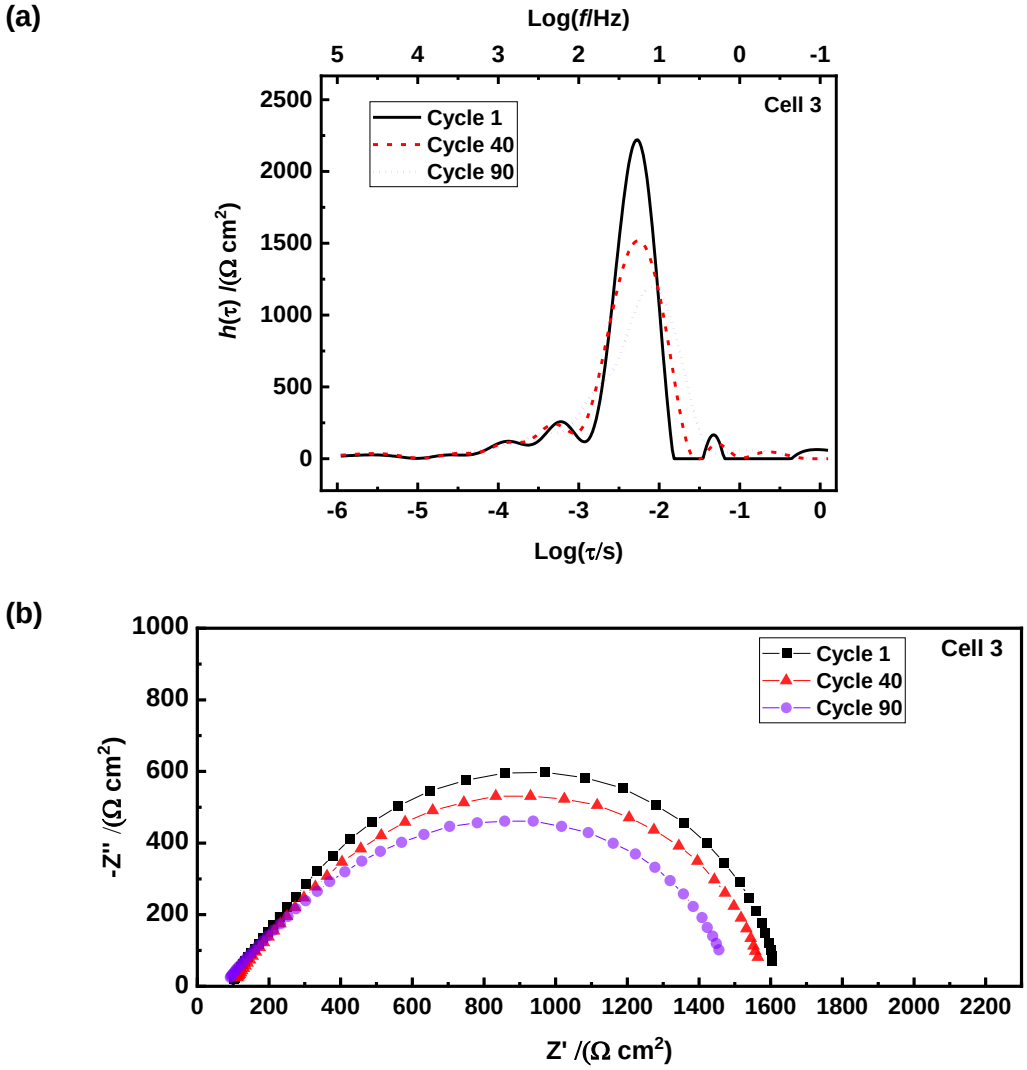

Figure A9: *(a) DRT spectrum of the overall impedances of cell 3 for cycles 1, 40, and 90 (cycling current density of 0.1 mA cm^{-2}). (b) Nyquist of normalized areal impedances of cell 3. Reprinted with permission from ref.[53] Copyright © 2024 American Chemical Society.*

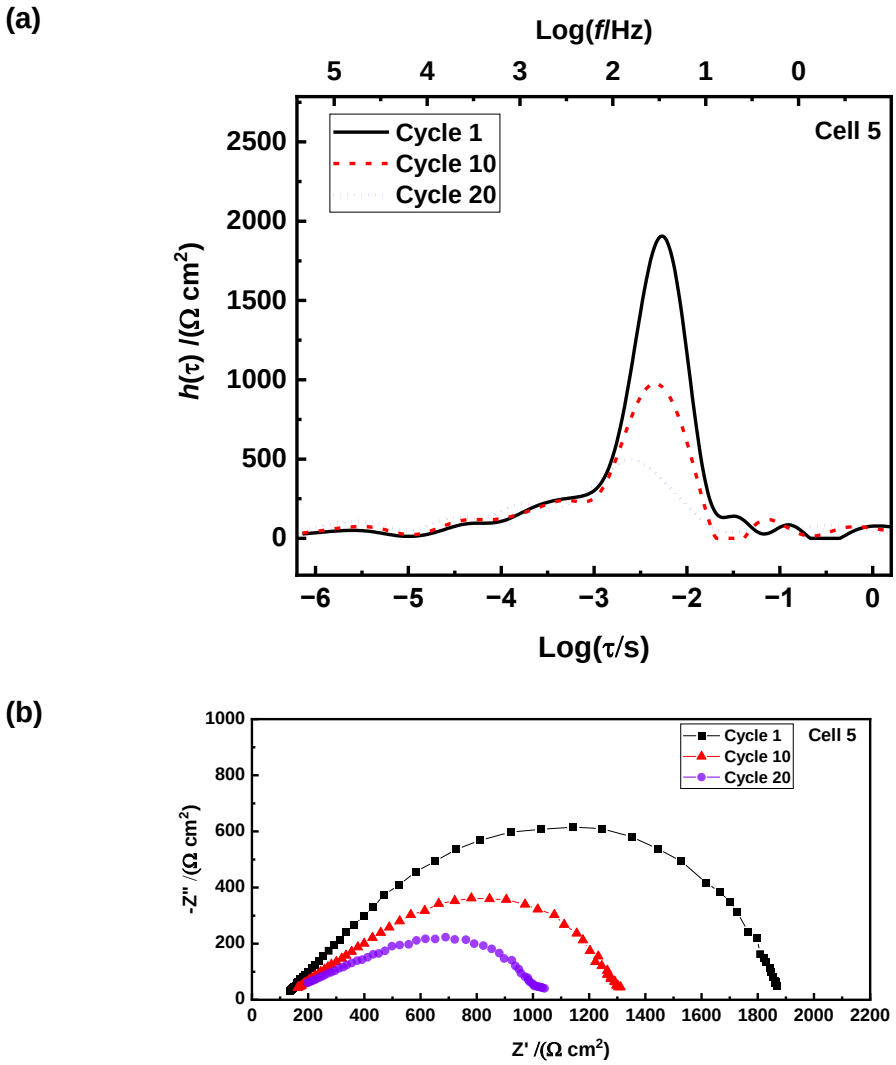

Figure A10: *(a) DRT spectrum of the overall impedances of cell 5 for cycles 1, 10, and 20 (cycling current density of 0.3 mA cm^{-2}). (b) Nyquist of normalized areal impedances of cell 5. Reprinted with permission from ref.[53] Copyright © 2024 American Chemical Society.*

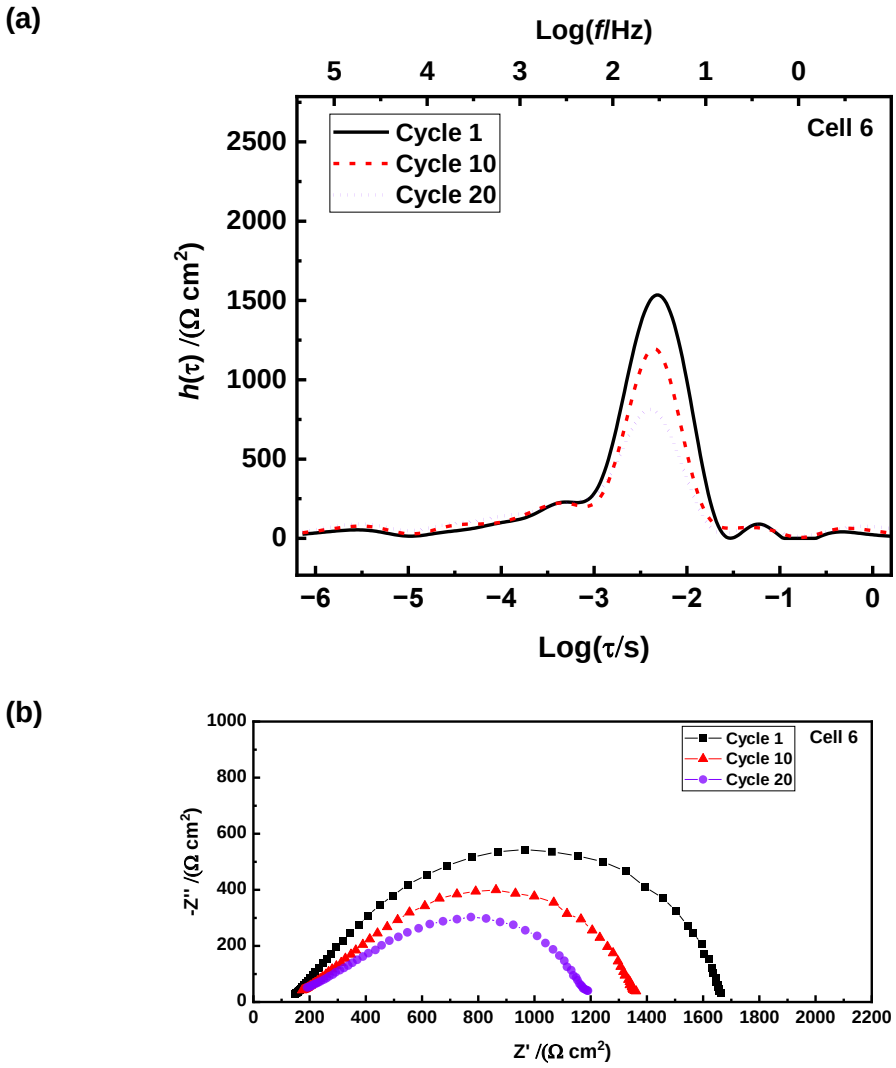

Figure A11: *(a) DRT spectrum of the overall impedances of cell 6 for cycles 1, 10, and 20 (cycling current density of 0.3 mA cm^{-2}). (b) Nyquist of normalized areal impedances of cell 6. Reprinted with permission from ref.[53] Copyright © 2024 American Chemical Society.*

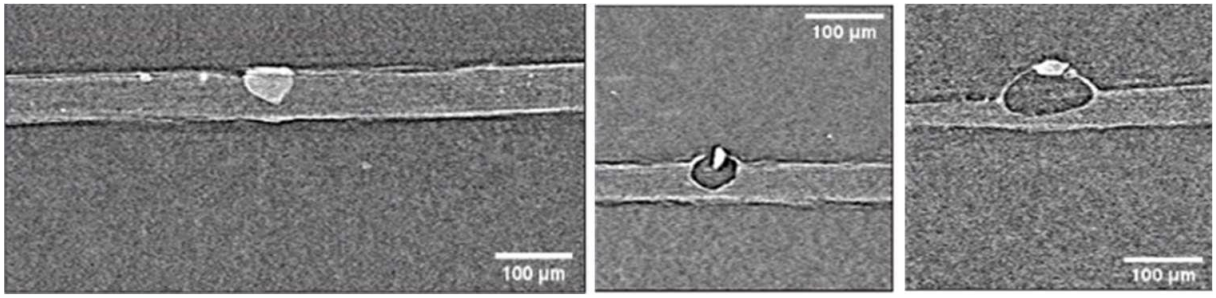

Figure A12: *Cross-sectional slices through the reconstructed X-ray tomograms representing different electrolyte impurity sizes and morphology. Reprinted with permission from ref.[53] Copyright © 2024 American Chemical Society.*

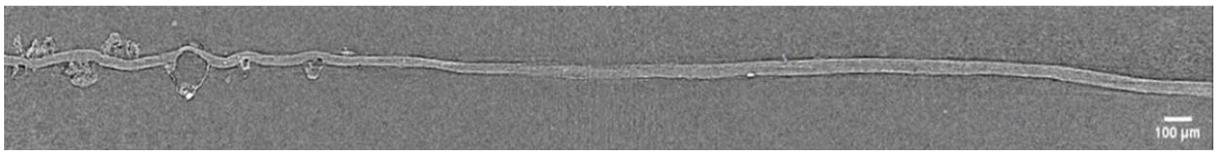

Figure A13: *Cross-sectional slice of a failed Li||Li cell with large accumulations of Li on the left side and largely planar deposition on the right side of the membrane. Reprinted with permission from ref.[53] Copyright © 2024 American Chemical Society.*

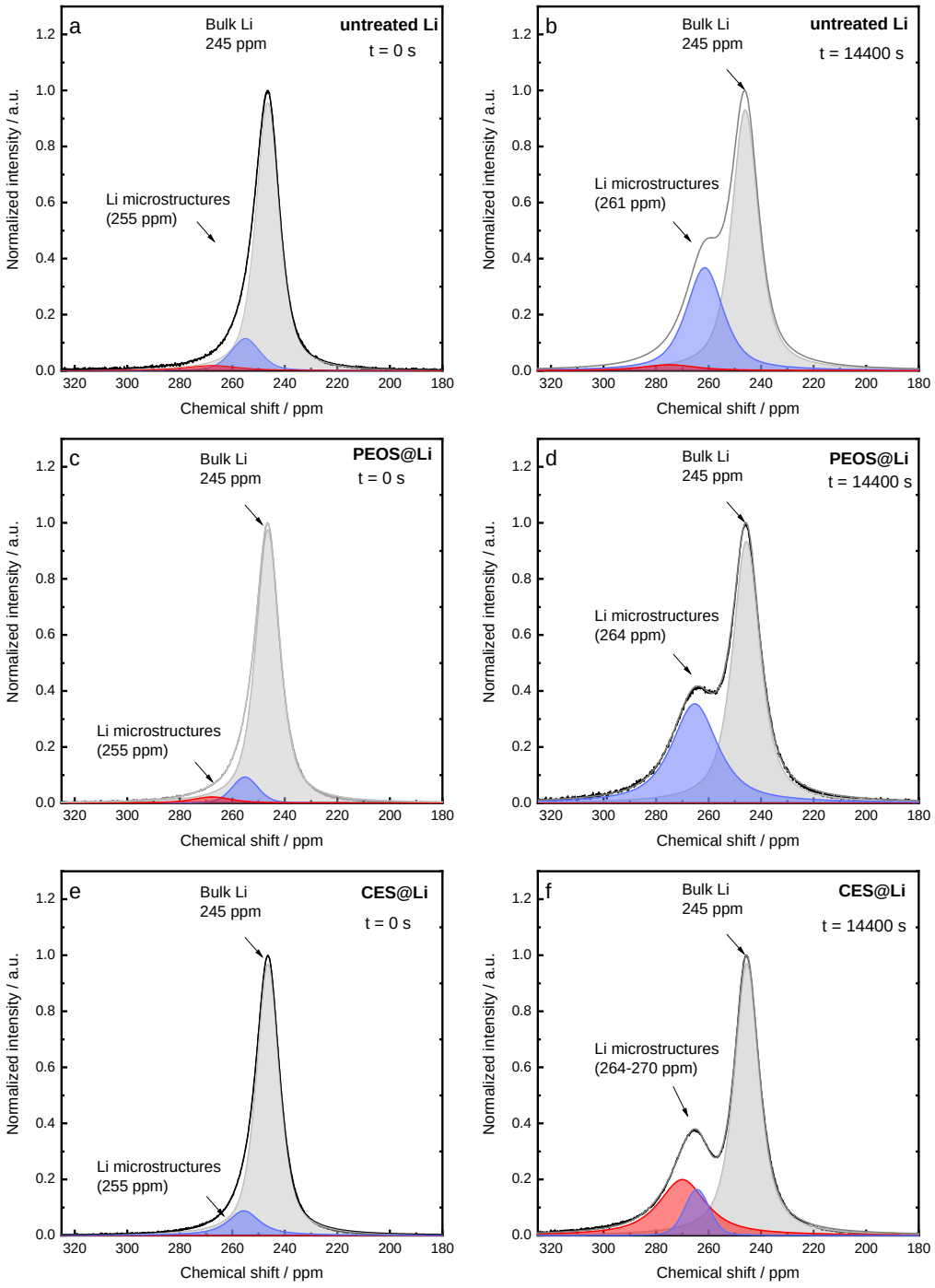

Figure A14: *In situ ^{7}Li NMR spectra of Li||Li cells with and without coatings before plating (a, c, e) and after plating (b, d, f), respectively, at a current density of 1 mA cm^{-2} (4 mAh cm^{-2}).*

Table A1: *Input parameters based on an experimental polymer electrolyte-based Li metal cell, as demonstrated by Chen et al.*[61]

	Projection based on experimental cell
Energy density /Wh L^{-1}	356
Specific energy /Wh kg^{-1}	213
Operating voltage /V	3.6
Average capacity /mAh g^{-1}	175
Electrolyte thickness /µm	30
Electrolyte density /g cm^{-3}	1.8
Lithium thickness /µm	50
Cathode thickness /µm	50
Cath. active material cont. /wt%	90
Active mass loading /mg cm^{-2}	11
Number of layers	15
Anode current collector thickness (Copper) /µm	15
Cathode current collector (Aluminum) thickness /µm	20
Casing thickness /µm	100
Casing area /cm^2	24
Current collector area /cm^2	22
Anode and cathode area /cm^2	20

Table A2: *Parameters from literature for various polymer electrolytes with Li metal cells. The index numbers 1to 49 correspond to those used in the main text.*

			Index [ref]	Cathode|Anode	m_{act} (mg cm^{-2})	Conductivity (S cm^{-1})	T (Conductivity) (°C)	Transference number	T (Cycling) (°C)	Cycle number	$C_{initial}$ (mAh g^{-1})	C_{final} (mAh g^{-1})	C-Rate	$V_{nominal}$ (V)	Liquid uptake (%)	Interfacial resistance (Ω cm^2)	Li conductivity (S cm^{-1})	Capacity retention (%)	CE (%)	$C_{avg.}$ (mAh g^{-1})	Avg. energy per cycle (mWh cm^{-2})
Polymer electrolytes	Polymers +Li salt	Dry polymers	1 [114]	LFP||Li	1.8	2.9E-04	60	0.31	60	200	163	122	0.20	3.4	--	--	8.9E-05	74.8	99.86	142.5	0.87
			2 [115]	LFP||Li	6	2.8E-04	70	0.43	70	30	130	132	0.33	3.4	--	40	1.2E-04	101.5	100.05	131.0	2.67
			3 [116]	LFP||Li	4	4.0E-04	70	0.63	70	30	140	140	0.10	3.4	--	564	2.5E-04	100.0	100.00	140.0	1.90
			4 [117]	LCO||Li	5	5.6E-03	60	0.56	60	100	152	127	0.10	3.9	--	169	3.1E-03	83.6	99.82	139.5	2.72
			5 [118]	LCO||Li	1.5	9.8E-05	60	0.57	50	150	146	123	0.10	3.9	--	1400	5.6E-05	84.2	99.89	134.5	0.79
			6 [119]	LVO||Li	--	--	--	--	80	60	270	105	0.33	--	--	--	--	38.9	98.44	187.5	--
			7 [119]	LFP||Li	--	--	--	--	70	1400	158	130	0.33	--	--	--	--	82.3	99.99	144.0	--
			8 [57]	NMC||Li	2.5	5.0E-05	60	0.59	60	60	180	155	0.10	3.7	--	100	3.0E-05	86.0	99.75	167.4	1.55
			9 [57]	NMC||Li	2.5	5.0E-05	60	0.59	60	500	125	70	1.00	3.4	--	--	3.0E-05	56.0	99.88	97.5	0.83
		Polymer-ceramic composites	10 [120]	LFP||Li	2.5	8.0E-05	25	0.28	60	20	84	90	1.00	3.4	--	--	2.2E-05	107.1	95.00	87.0	0.74
			11 [121]	LFP||Li	--	8.0E-05	30	0.43	60	60	145	139	0.20	3.4	--	350	3.4E-05	95.9	99.93	142.0	--
			12 [122]	LFP||Li	0.8	1.9E-04	25	0.5	35	200	135	111	0.50	3.4	--	70	9.5E-05	82.2	99.90	123.0	0.33
			13 [123]	LFP||Li		1.6E-04	30	0.47	30	200	122	100	0.10	3.4	--	150	7.5E-05	82.0	99.90	111.0	--
			14 [94]	NMC||Li	7	1.1E-03	--	0.43	60	300	160	125	--	3.7	100	17	4.7E-04	78.1	99.92	142.5	3.69
		Gels	15 [124]	LFP||Li	--	1.0E-04	--	--	60	--	--	--	--	--	100	25	--	--	--	--	--
			16 [125]	LFP||Li	1.5	7.2E-04	70	0.57	70	500	158	111	0.50	3.4	130	300	4.1E-04	70.3	99.93	134.5	0.69
			17 [126]	LCO||Li	1	2.8E-03	60	0.54	60	700	178	151	1.00	3.9	650	80	1.5E-03	84.8	99.98	164.5	0.64
			18 [126]	LCO||Li	1	1.3E-04	25	0.54	25	650	172	122	1.00	3.9	--	--	7.2E-04	70.9	99.95	147.0	0.57
			19 [127]	LFP||Li	--	1.6E-04	25	0.47	10	100	146	139	0.20	3.4	100	374	7.7E-05	95.2	99.95	142.5	--
			20 [128]	NMC||Li	2.5	3.3E-03	25	0.63	25	50	160	139	0.20	3.5	422	500	2.1E-03	86.9	99.72	149.5	1.31
			21 [129]	LFP||Li	3	8.1E-04	30	--	25	250	120	118	1.00	3.4	--	--	--	98.3	99.99	119.0	1.21
			22 [71]	NMC||Li	2.5	1.0E-03	60	0.28	60	500	160	120	1.00	3.6	--	40	2.8E-04	75.0	99.94	140.0	1.26
			23 [71]	NMC||Li	2.5	5.0E-04	40	0.28	40	500	125	113	1.00	3.6	--	--	1.4E-04	90.4	99.98	119.0	1.07

Table A2 (continued): *Parameters from literature for various polymer electrolytes with Li metal cells. The index numbers 1 to 49 correspond to those used in the main text.*

			Index [ref]	Cathode|Anode	m_{act} (mg cm^{-2})	Conductivity (S cm^{-1})	T (Conductivity) (°C)	Transference number	T (Cycling) (°C)	Cycle number	$C_{initial}$ (mAh g^{-1})	C_{final} (mAh g^{-1})	C-Rate	$V_{nominal}$ (V)	Liquid uptake (%)	Interfacial resistance (Ω cm^2)	Li conductivity (S cm^{-1})	Capacity retention (%)	*CE* (%)	$C_{avg.}$ (mAh g^{-1})	Avg. energy per cycle (mWh cm^{-2})
	Single-ion conductors	Blend or co-polymers	24 [130]	LFP||Li	4	1.0E-04	70	0.91	70	300	100	85	0.50	3.35	--	811	9.1E-05	85.0	99.95	92.5	1.24
			25 [131]	LFP||Li	0.8	1.3E-05	60	0.85	60	--	--	--	0.50	--	--	100	1.1E-05	85.0	--	--	--
			26 [132]	LFP||Li	--	8.4E-05	80	0.91	80	50	120	120	0.10	3.2	--	--	7.6E-05	--	--	120.0	--
		Gels	27 [133]	LFP||Li	0.8	5.7E-05	25	0.88	25	500	100	95	1.00	3.35	122	330	5.0E-05	95.0	99.99	97.5	0.26
			28 [76]	LFP||Li	5	1.2E-04	25	0.9	25	100	126	125	0.10	3.35	50	500	1.1E-04	99.2	99.99	125.5	2.10
			29 [134]	NMC||Li	2.25	1.0E-03	30	1	40	230	100	105	0.20	3.7	--	--	1.0E-03	--	99.50	102.5	0.85
			30 [43]	NMC||Li	2.8	5.2E-04	20	0.9	20	100	116	101	0.10	3.7	--	--	4.7E-04	87.1	99.86	108.5	1.12
			31 [135]	LFP||Li	--	1.7E-05	30	0.92	25	80	122	119	0.20	3.4	40	12000	1.5E-05	97.5	99.97	120.5	--
			32 [136]	LFP||Li	1.5	1.0E-04	25	0.92	25	1000	105	105	1.00	3.3	--	--	9.6E-05	100.0	100.00	105.0	0.52
			33 [137]	LFP||Li	5	4.1E-04	25	0.93	25	800	108	100	1.00	3.4	--	--	3.8E-04	92.6	99.99	104.0	1.77
			34 [138]	LFP||Li	1.5	1.6E-04	25	0.9	25	1000	126	120	1.00	3.4	--	--	1.4E-04	95.2	100.00	123.0	0.63
			35 [139]	LFP||Li	--	3.1E-04	25	0.97	80	350	118	106	0.10	--	--	--	3.0E-04	89.8	99.97	112.0	--
			36 [140]	LFP||Li	--	1.3E-03	25	0.92	25	380	141	128	1.00	3.4	--	--	1.2E-03	90.8	99.97	134.5	--
			37 [141]	LFP||Li	1.7	1.5E-03	25	0.89	25	500	138	124	1.00	3.4	--	--	1.3E-03	89.9	99.98	131.0	0.76
			38 [142]	LFP||Li	--	1.5E-04	26	0.95	25	--	--	--	--	--	30	--	1.4E-04	--	--	--	--
			39 [143]	LFP||Li	2.7	1.0E-06	65	0.79	65	100	145	119	0.10	3.4	--	--	7.9E-07	82.1	99.80	132.0	1.21
			40 [144]	NMC||Li	2	1.0E-03	40	1	40	180	165	132	1.00	3.6	--	--	1.0E-03	80.0	99.88	148.5	1.07
			41 [145]	LMO||Li	3.2	5.0E-04	25	0.91	25	100	90	92	0.50	3.9	--	--	4.6E-04	102.2	100.02	91.0	1.14
			42 [146]	LFP||Li	5	6.8E-04	25	0.85	25	1000	110	100	1.00	3.4	--	--	5.8E-04	90.9	99.99	105.0	1.79
Liquid electrolytes			43 [95]	NMC||Li	7.5	1.4E-03	25	0.62	25	90	220	180	0.50	3.6	--	--	8.5E-04	81.8	99.78	200.0	5.40
			44 [147]	NMC||Li	7.5	2.4E-03	25	--	25	250	216	175	0.33	3.3	--	--	--	81.0	99.92	195.5	4.84
Inorganic solid-state electrolytes			45 [148]	LFP||Li	5.88	6.0E-04	25	1	25	1000	87.5	70	1.00	3.5		30	6.0E-04	80.0	99.98	78.8	1.62
			46 [149]	LCO||Li	5.5	--	--	--	25	500	137	119	0.10	3.9	--	--	--	86.9	99.97	128.0	2.75
			47 [93]	NMC||μSi	25	--	--	--	25	500	80	60	1.00	3.4	--	--	--	75.0	99.94	70.0	5.95
HIMS polymer xBtH			48 [61]	NMC||Li	6	1.1E-05	60	0.49	60	50	186	142	0.25	3.6	--	--	5.4E-05	76.0	99.45	164.0	3.54
Tesla liquid electrolyte			49 [92]	LFP||C	21.5	---	25	--	--	--	--	--	--	3.25	--	--	--	--	99.95	--	8.94

***Table A3**: Cell components of the experimental prototype pouch cell containg Li metal and a solid polymer electrolyte.*

Cell components	Mass /mg	Rel. mass /wt%	Thickness /µm	Area /cm^2
Lithium metal	104.6	1.6	50	44.4
Electrolyte membrane	114.2	1.7	50	60.1
Cathode (incl. Aluminum)	614.9	9.2	55	36.4
Pouch casing, tape, tabs	5825.3	87.5	100	209
Total	**6659.0**	**100**	**355**	**209**

***Table A4**: Cathode components of the experimental prototype pouch cell containg Ni-rich NMC83 (83 wt% Ni), Aluminum current collector foil, Oligomer as catholyte and Carbon Black as electronic conductor.*

Cathode components	Mass /mg	Rel. mass /wt%	Mass loading /(mg cm^{-2})
NMC83	364.48	59.3	10.13
Aluminum	153.81	25.0	4.11
Oligomer	81.47	13.2	2.24
Binder + Carbon Black	15.19	2.5	0.42
Total	**614.95**	**100**	**16.9**

***Table A5**: Electrolyte components of the experimental prototype pouch cell the solid polymer Bt-PCL, the conducting salt LiTFSI, a thin polyethylen (PE) matrix, as well as benzophenon (BP) as cross-linking agent.*

Electrolyte components	Mass /mg	Rel. mass /wt%	Mass loading /(mg cm^{-2})
Bt-PCL	56.54	49.5	0.94
LiTFSI	28.11	24.6	0.47
PE matrix	27.05	23.7	0.45
BP cross-linker	2.51	2.2	0.042
Total	**114.20**	**100**	**1.9**

Permissions to use and adapt previously published figures

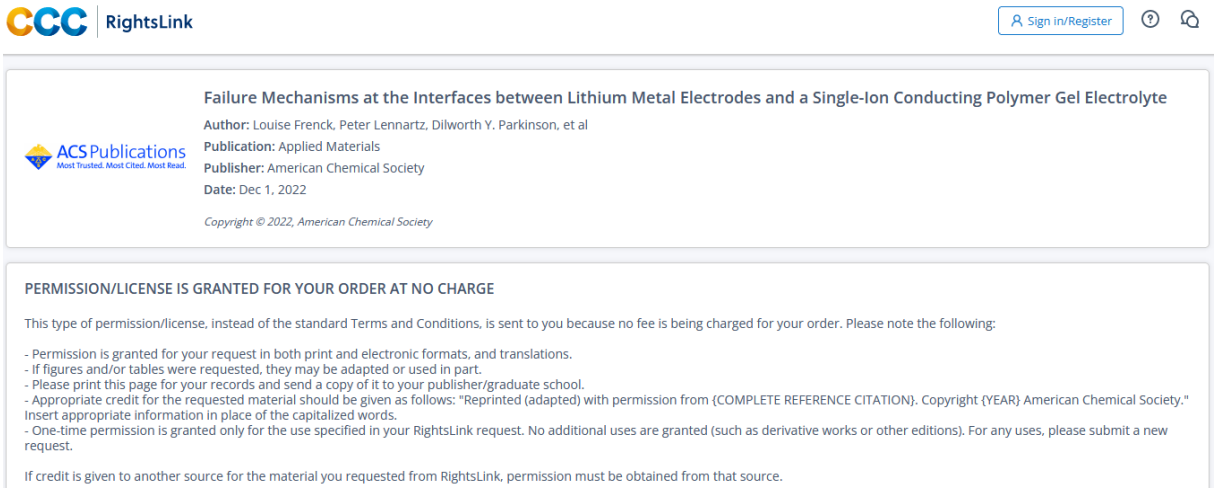

RightsLink

Sign in/Register

ACS Publications
Most Trusted. Most Cited. Most Read.

Failure Mechanisms at the Interfaces between Lithium Metal Electrodes and a Single-Ion Conducting Polymer Gel Electrolyte

Author: Louise Frenck, Peter Lennartz, Dilworth Y. Parkinson, et al
Publication: Applied Materials
Publisher: American Chemical Society
Date: Dec 1, 2022

Copyright © 2022, American Chemical Society

PERMISSION/LICENSE IS GRANTED FOR YOUR ORDER AT NO CHARGE

This type of permission/license, instead of the standard Terms and Conditions, is sent to you because no fee is being charged for your order. Please note the following:

- Permission is granted for your request in both print and electronic formats, and translations.
- If figures and/or tables were requested, they may be adapted or used in part.
- Please print this page for your records and send a copy of it to your publisher/graduate school.
- Appropriate credit for the requested material should be given as follows: "Reprinted (adapted) with permission from {COMPLETE REFERENCE CITATION}. Copyright {YEAR} American Chemical Society." Insert appropriate information in place of the capitalized words.
- One-time permission is granted only for the use specified in your RightsLink request. No additional uses are granted (such as derivative works or other editions). For any uses, please submit a new request.

If credit is given to another source for the material you requested from RightsLink, permission must be obtained from that source.

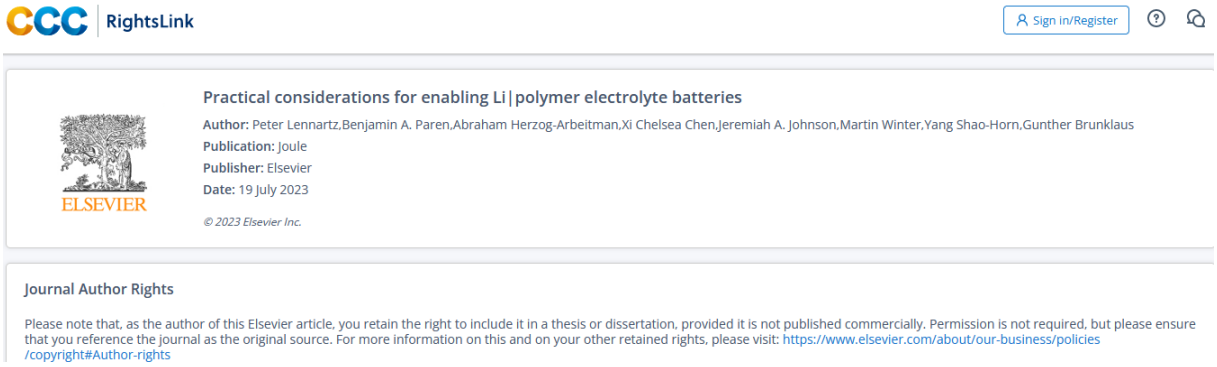

RightsLink

Sign in/Register

ELSEVIER

Practical considerations for enabling Li|polymer electrolyte batteries

Author: Peter Lennartz,Benjamin A. Paren,Abraham Herzog-Arbeitman,Xi Chelsea Chen,Jeremiah A. Johnson,Martin Winter,Yang Shao-Horn,Gunther Brunklaus
Publication: Joule
Publisher: Elsevier
Date: 19 July 2023

© 2023 Elsevier Inc.

Journal Author Rights

Please note that, as the author of this Elsevier article, you retain the right to include it in a thesis or dissertation, provided it is not published commercially. Permission is not required, but please ensure that you reference the journal as the original source. For more information on this and on your other retained rights, please visit: https://www.elsevier.com/about/our-business/policies/copyright#Author-rights

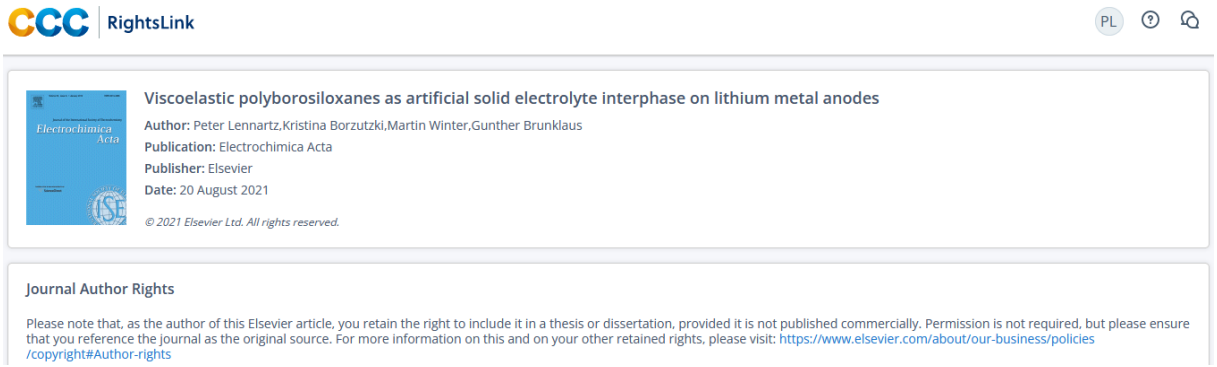

RightsLink

PL

Viscoelastic polyborosiloxanes as artificial solid electrolyte interphase on lithium metal anodes

Author: Peter Lennartz,Kristina Borzutzki,Martin Winter,Gunther Brunklaus
Publication: Electrochimica Acta
Publisher: Elsevier
Date: 20 August 2021

© 2021 Elsevier Ltd. All rights reserved.

Journal Author Rights

Please note that, as the author of this Elsevier article, you retain the right to include it in a thesis or dissertation, provided it is not published commercially. Permission is not required, but please ensure that you reference the journal as the original source. For more information on this and on your other retained rights, please visit: https://www.elsevier.com/about/our-business/policies/copyright#Author-rights

DOI: 10.17185/duepublico/82699
URN: urn:nbn:de:hbz:465-20241213-112951-9